

**Design and development of a two-phase closed loop
thermosyphon for CPU cooling**

Miguel Andrade Pereira Barata Moura

Thesis to obtain the Master of Science Degree in

Mechanical Engineering

Supervisor: Dr. Ana Sofia Oliveira Henriques Moita

Examination Committee

Chairperson: Prof. Viriato Sérgio de Almeida Semião

Supervisor: Dr. Ana Sofia Oliveira Henriques Moita

Member of the Committee: Prof. Pedro Jorge Martins Coelho

November 2015

Acknowledgments

Foremost, I would like to express my sincere gratitude to Doctor Ana Moita and to the Ph.D candidate Emanuele Teodori for the scientific guidance and supervision through the course of this dissertation. Their availability, motivation, enthusiasm and support were of utmost importance for my academic success and for my personal life. I would also like to thank to Professor Doctor Luis Nobre Moreira for his acceptance in his research group.

I would also like to express my gratitude to Professor Doctor José Carlos Pereira for the support, availability and valuable guidance thought the numerical simulation.

My thanks to *Sorradiadores* for the manufacture of the condenser used in this work; to the *Frigoríficos Imperial* C.E.O. Mr. José Fonseca for the guided tour to the factory premises and valuable advices given for the experimental setup; to the Production Manager António Granjeia and Engineer Manuela Soares, from *Centauro*, for the advices given concerning the condenser design; to Mr. Chito Pereira, from *Versa*, for the important advices given on the design and sizing of the auxiliary equipments used in this work; to the Mechanical II building workshops' staff for the help and guidance through the manufacturing of several parts for the experimental facility; to Mr. Manuel Amaral, from *Amaral Radiadores*, for the welding job on the last prototype; to Engineer Camilo for providing the acquisition board, and to my uncle Mr. Henrique Pereira for the precious help in the design of all the electronic circuits developed for monitoring and control of the experimental facility.

A huge appreciation to all my dear laboratory colleagues: to Tomás Valente, for the long and late night philosophical discussions about boiling heat transfer; to Catarina Laurência, for having introduced me to the IN+ and shown me this opportunity; to the Ph.D. candidate Vânia Silvério for the chemistry lessons about the working fluid used and research methodology advices; to Filipe Ferreira, for sharing with me the ups and downs of developing an experimental facility from scratch; to Davide Almeida, for the help with *COMSOL*. To all, thank you for your support in the more difficult times and for sharing your enthusiasm in the celebration of fulfilled goals. I also thank to my closest friends: Ricardo Rodrigues, Gonçalo Gomes, João Batista and Diogo Rebelo for their genuine interest in my work, for their support and motivation. Finally, to my dear brother and mother, to whom I dedicate this thesis.

At last, I am grateful to Fundação para a Ciência e a Tecnologia (FCT) for partially financing this research under the framework of the project RECI/SEM-SIS/0147/2012 and for the award of a research fellowship.

Abstract

The present work comprises the design and development of a benchmark facility based on a two-phase closed loop thermosyphon. This study aims at demonstrating the feasibility of pool boiling of dielectric fluids to be used as a CPU cooling technique.

The devised system acts as a modular benchmark facility, allowing a detailed analysis of the various parameters that influence its performance, which were investigated for steady state and transient working conditions.

Regarding the use of micro-structured surfaces, the micro-patterns consist of arrays of laser etched cavities, with fixed shape and dimensions, so the sole varying parameter is the distance between cavities. The results show that the overall thermal resistance is reduced 21% using the surface with cavities distance of $300 \mu m$, when compared to the performance evaluated for a smooth surface. In transient power steps, the onset of nucleate boiling was identified as the critical parameter influencing the system performance, due to the overshoot in the temperature above steady-state values.

The condenser tilt angle affects the overall performance of the system: a 10° inclination, compared to the horizontal position lead to a decrease in 5% of the overall thermal resistance.

Concerning the orientation of the evaporator, the cooling system has a lower performance for the evaporator mounted in the vertical position. However, this outcome is balanced by the benefits arising from more application oriented implementation.

Based on this analysis, the geometry of the final system was optimized. The final thermal resistance achieved was $R_{ja} = 0.29 \text{ }^\circ\text{C}/\text{W}$ for a heat load $Q = 130 \text{ W}$.

Keywords

Pool boiling, closed loop thermosyphon, CPU cooling system, overall thermal resistance, micro-structured surfaces

Resumo

O presente trabalho contempla o projeto e desenvolvimento de uma instalação experimental para avaliar a aplicabilidade de um sistema de arrefecimento de micro-processadores, baseado na ebulição quiescente de fluidos dielétricos.

O sistema desenvolvido é modular de modo a permitir a análise detalhada dos diversos parâmetros que podem afetar o seu desempenho. Esta análise realizou-se considerando condições de operação estacionárias e transientes.

Este trabalho considerou o uso de superfícies micro-estruturadas no evaporador. O micro-padrão é composto por linhas de cavidades, com uma forma e uma dimensão fixas, modificando-se apenas a distância entre cavidades. Os resultados, obtidos em condições de operação estacionárias, mostram que a resistência térmica global é reduzida em 21% quando se usa uma superfície com uma distância entre cavidades de $300 \mu m$. Na análise da resposta do sistema de arrefecimento a degraus de potência impostos, o ponto onde se inicia a ebulição determina a resposta do sistema, traduzida numa acentuada subida da temperatura, acima dos valores obtidos em condições de operação estacionárias.

O ângulo de inclinação do condensador afeta também a resposta do sistema: uma inclinação de 10° em relação à posição horizontal conduz a um decréscimo de 5% da resistência térmica global.

Relativamente à orientação do evaporador, o sistema apresenta pior desempenho quando o evaporador é montado na posição vertical. No entanto, este resultado é contrabalançado pelos benefícios inerentes à aplicabilidade do sistema desenvolvido em situações reais.

No final desta análise, o sistema projetado foi otimizado e apresenta uma resistência térmica global de $R_{ja} = 0.29 \text{ }^\circ C/W$, para uma potência térmica dissipada $Q = 130 W$.

Palavras-chave

Ebulição em meio quiescente, termossifão em circuito fechado, sistema de arrefecimento de CPU, resistência térmica global, superfícies micro-estruturadas.

Table of Contents

Acknowledgments	iii
Abstract	v
Resumo	vii
Table of Contents	ix
List of Figures	xi
List of Tables	xv
List of Acronyms	xvii
List of Latin Letters	xviii
List of Greek Symbols	xix
Subscripts	xix
1. Introduction	1
1.1. Context and motivation	1
1.2. Objectives and Contribution	2
1.3. Document structure	3
2. State of the art	5
2.1. Overview of existing CPU cooling techniques.....	5
2.2. Two-phase closed loop thermosyphon: parametric research and implementation in the context of CPU cooling	7
3. Theoretical background	11
3.1. Fundamentals of Nucleate Pool Boiling Heat Transfer	11
3.1.1. Boiling curve	11
3.1.2. Physical Mechanism of Boiling heat transfer	14
3.1.3. Pool boiling from vertically oriented surfaces	15
3.2. Boiling on Enhanced Surfaces	16
3.3. Condensation inside tubes	17
4. CPU thermal simulation	23
4.1. Overview	23
4.2. Transistor as a die simulator	24
4.3. CPU package simulation	26

4.4.	Validation	29
4.4.1.	Infrared Thermography experimental setup	30
4.4.2.	Results and conclusions	32
5.	Design and development of the thermosyphon experimental facility	35
5.1.	Proof of concept prototype	35
5.1.1.	Working fluid	35
5.1.2.	Experimental prototype, instrumentation and acquisition	37
5.1.3.	Results and conclusions	39
5.2.	Final experimental facility design	40
5.2.1.	Evaporator design.....	40
5.2.2.	Condenser design.....	41
5.2.3.	Experimental facility overview	51
5.3.	Experimental methodology	51
6.	Results and discussion.....	55
6.1.	Loop characterization and working conditions	55
6.2.	Effect of surface micro-structuring.....	58
6.2.1.	Steady-state analysis under real working conditions	58
6.2.2.	Steady-state analysis under controlled working conditions.....	63
6.2.3.	Transient analysis	66
6.3.	Condenser optimization.....	70
6.3.1.	Effect of tilt angle	70
6.3.2.	Reflux condenser.....	72
6.4.	Evaporator Optimization	75
6.4.1.	Orientation effects.....	76
6.4.2.	Effect of evaporator's dimension in vertical orientation	79
7.	Conclusions and Future Work.....	83
7.1.	Conclusions	83
7.2.	Future work.....	84
	References	85
	Annexes.....	I
	Annex A – Electronic circuits:.....	I
	A.1. Transistor power control unit:.....	I
	A.2. Power supply remote control unit:.....	II
	A.3. Fan control and acquisition unit	III
	A.4. Differential pressure transducers amplification circuit	III

List of Figures

Figure 3.1 – Boiling curve for a horizontal plain surface.	12
Figure 3.2 – Review of effects of orientation on CHF. Refer to [63] for the references in legend....	15
Figure 3.3 – a) Baker flow pattern map; b) Flow regimes illustration (grey = liquid, white = vapour)	18
Figure 3.4 – a) Heat transfer coefficient as function of tilt angle for several mass fluxes and $x = 0.25$; b) Optimum angle for different saturation temperature and $x = 0.25$ [80]......	20
Figure 3.5 – Effect of inclination angle on reflux condensation heat transfer for a 7 mm tube and R134a [83]......	20
Figure 4.1 – a) Intel Pentium 4 2.0GHz, bottom view; b) Intel Pentium 4 3.4GHz, bottom view	23
Figure 4.2 – Intel i7 processor package components	24
Figure 4.3 – a) N-channel transistor package; b) Connection circuit diagram	25
Figure 4.4 – a) Electronic control circuit diagram; b) Experimental setup.....	26
Figure 4.5 – Intel Pentium 4 IHS bottom view (left), processor die top view (centre) and selected transistor bottom view (right)......	27
Figure 4.6 – Remote programming controller unit. a) Electronic circuit; b) User interface panel	28
Figure 4.7 – Transistor incorporated within CPU package simulator. a) Bottom assembly view; b) Transistor detail with 0.5mm K-Type insulated probe thermocouple; c) Overview of developed system's top view.	29
Figure 4.8 – Experimental setup	30
Figure 4.9 – Experimental assembly. a) Intel Pentium 4; b) CPU simulator	31
Figure 4.10 – IR image of CPU and transistor assembly at $P_D=15W$. a) Intel Pentium 4; b) CPU simulator. Dashed lines indicate acquisition region	32
Figure 4.11 – Temperature distribution in steady-state conditions.	32
Figure 4.12 – Maximum temperature at steady-state conditions.	33
Figure 4.13 – CPU and Transistor assembly under transient power step. a) $P_D \cong 10W$; b) $P_D \cong 20W$	34
Figure 4.14 – CPU and Transistor temperature evolution under cyclic power steps.	34
Figure 5.1 – Proof-of-concept prototype.....	38
Figure 5.2 – CAD model of the evaporator.....	41

Figure 5.3 – a) Actual fluid temperature distribution in a condensation process. b) Idealized model. Adapted from [89].	42
Figure 5.4 – Corrugated herringbone fin on a tube array. a) front view; b) side view; Adopted from [89].	44
Figure 5.5 – Numerical model and boundary conditions used.	46
Figure 5.6 – a) Fluid and solid discrete domains; b) Qualitative velocity magnitude; c) Qualitative temperature distribution in the solid and fluid.	48
Figure 5.7 – a) Wang's correlation <i>j-Colburn</i> factor comparison with numerical results; b) Heat transfer rate comparison	48
Figure 5.8 – Flat tube with plain serpentine fins geometry from Sorradiadores.	49
Figure 5.9 – a) CAD model; fluid and solid domain mesh; c) Qualitative temperature distribution in both domains for $Re_{Dh} = 280$.	50
Figure 5.10 – Condenser manufactured according to technical drawings by Sorradiadores.	50
Figure 5.11 – Overview of the experimental facility. a) Overview; b) detail of the test section; c) Evaporator; d) Condenser.	52
Figure 5.12 – Typical power profile of an Intel Pentium 4 used in the transient tests [95].	53
Figure 5.13 – Methodology algorithm employed within the multi-parameter exploratory investigation. Red circle denotes an illustrative final geometry achieved.	54
Figure 6.1 – Steady-state pressure and temperature measurements along the loop as function of dissipated power. a) Absolute evaporator pressure; b) Temperature distribution.	55
Figure 6.2 – Thermodynamic cycles of the developed loop thermosyphon. a) Combined temperature and pressure measurement locations; b) p-h diagram under steady-state conditions at 150W.	56
Figure 6.3 – Liquid free surface height ratio as function of heat load. Error bars indicate the standard deviation of consecutive measurements.	57
Figure 6.4 – Overall thermal resistance (junction-to-ambient) as function of heat load.	58
Figure 6.5 – Steady-state boiling curves under real working conditions. a) Increasing heat flux; b) Decreasing heat flux.	59
Figure 6.6 – Steady-state real working conditions boiling curve example for increasing and decreasing heat flux.	60
Figure 6.7 – Visualization of the boiling phenomena for increasing and decreasing heat flux with $S = 600\mu\text{m}$. a) 60W increasing; b) 60W decreasing; c) 40W increasing; d) 40W decreasing; e) 20W increasing; f) 20W decreasing; g) 10W increasing; h) 10W decreasing.	61

Figure 6.8 – Overall steady-state thermal resistance under real working conditions as function of cavity distance.....	62
Figure 6.9 – Boiling curves under controlled pressure via PID.	63
Figure 6.10 – Rohsenow correlation with experimental data. Predicted and experimental temperature superheat.....	64
Figure 6.11 – Heat transfer ratio versus cavity distance	65
Figure 6.12 – Simulated CPU die junction temperature with Isci & Martonosi benchmark power profile for an Intel Pentium 4 [95]. $S=300\mu\text{m}$	66
Figure 6.13 – Maximum junction temperature reached versus cavity distance.	67
Figure 6.14 – Illustrative example of a typical junction temperature step response	68
Figure 6.15 – Average results as function of applied power step. a) Peak time at the onset of nucleate boiling for the five surfaces under examination; b) Maximum junction temperature at the overshoot, $T_{j.ONB}$. Dashed lines indicate steady-state settled temperature for the same heat load.....	68
Figure 6.16 – Temperature of onset of nucleate boiling versus cavity distance. Arrow indicates the onset of boiling a) Experimental methodology; b) Results comprising average and standard deviation of the measurements.....	70
Figure 6.17 – Study on the effect of tilt angle. a) 0° ; b) 45° ; c) 90°	71
Figure 6.18 – Overall thermal resistance as function of tilt angle and heat load.	72
Figure 6.19 – Reflux condenser. a) Experimental test section overview; b) Counter-flow pattern in the connecting lines.	73
Figure 6.20 – a) Steady-state junction temperature measurements for both condenser arrangements; b) Temperature fluctuations due to partial dry-out with the reflux condenser at 150W.	74
Figure 6.21 – Thermal resistance as function of reflux condenser tilt angle.	75
Figure 6.22 – Overall thermal resistance as function as initial working fluid fill charge	76
Figure 6.23 – a) Overview of the experimental facility comprising a vertically oriented evaporator; b) Detail of the boiling phenomena occurring inside the evaporator at $Q=150\text{W}$	77
Figure 6.24 – a) Boiling curves under real working conditions for vertical and horizontal orientation. Increasing and decreasing heat flux; b) PID controlled environment comparison between horizontal and vertical orientation	77
Figure 6.25 – Overall thermal resistance and equilibrium pressure as function of initial working fluid fill charge with vertical orientation	78
Figure 6.26 – Overall thermal resistance as function of initial fill charge ratio.	79

Figure 6.27 – Overall thermal resistance as function of heat load for the three vertical configurations tested..... 80

List of Tables

Table 3.1 – Values of the factors F and F' for laminar film stratified condensation in a horizontal tube [77].....	19
Table 4.1 – IRF450 N-channel power MOSFET	27
Table 4.2 - Xenics ONCA 4969 IR camera.....	30
Table 5.1 - 3M Novec HFE-7000 properties at 25°C, 1atm.....	36
Table 5.2 - Polymeric materials compatibility chart with 3M Novec HFE fluids.....	37
Table 5.3 – Grid independency study; $Re_{dc} = 1010$	47
Table 6.1 – Overall thermal resistance as function of cavity distance at 150W under real working conditions.....	62
Table 6.2 – Average temperature overshoot at the onset of nucleate boiling under sudden power step.....	69

List of Acronyms

ADC	Analog to Digital Converter
CAD	Computer-Aided Design
CFD	Computational Fluid Dynamics
CHF	Critical Heat flux
CPU	Central processing unit
DAC	Digital to Analog Converter
DC	Direct Current
FE	Finite Element
FEM	Finite Element Method
FVM	Finite Volume method
GPU	Graphics Processing Unit
IC	Integrated Circuit
IHS	Integrated Heat Spreader
IR	Infra-red
LMTD	Log mean temperature difference
PC	Personal computer
PDE	Partial Differential Equation
PID	Proportional integral derivative
ROI	Region of Interest
TDP	Thermal Design Point
TIM	Thermal Interface Material
VDC	Volts Direct Current

List of Latin Letters

a	parameter in eq. (3.1)	-
A	surface area	m^2
C	constant in eq. (3.3)	-
C_p	specific heat	J/kg.K
C_{sf}	constant in Rohsenow correlation, eq. (3.2), eq. (6.2)	-
D	diameter	m
F	correction factor in Chato correlation, eq. (3.4), eq. (3.6), eq. (3.7)	-
	counter flow correction factor, in eq. (5.6)	-
g	acceleration due to gravity	m/s^2
h	heat transfer coefficient	$W/m^2.K$
h_{fg}	latent heat of vaporization	J/kg
I	electrical current	A
k	thermal conductivity	$W/m.K$
L	length	m
m	index used in eq. (3.2)	-
n	index used in eq. (3.2)	-
r	radius	m
P	electrical power	W
q''	heat flux	W/cm^2
Q	heat rate	W
R	electrical resistance	Ω
R	thermal resistance	$^{\circ}C/W$
S	cavity distance	μm
T	temperature	$^{\circ}C$
U	electrical voltage	V
x	mass vapour quality	-

List of Greek Symbols

α	Thermal diffusivity	m^2/s
β	Gain in current for a Transistor	-
ϵ	Emissivity	-
δ	fin thickness	m
μ	Viscosity	Pa.s
ρ	Density	Kg/m^3
ϕ	Titl angle	deg.
σ	Surface tension	N/m
σ_{SB}	Stefan-Boltzmann constant	$\text{W}/\text{m}^2\text{K}^4$
τ	Transmissivity	-
ν	Kinematic viscosity	m^2/s

Subscripts

amb	ambiente conditions
av	average
b	base
c	coolant
cond	condenser
dc	collar diameter
evap	evaporator
ext	exterior
f	frontal; fin
g	gas/vapour phase
h	hydraulic
int	interior
j	junction
l	liquid phase; longitudinal

ls	liquid-solid
lv	liquid-vapour interface
max	maximum
NB	nucleate boiling
o	outer
obj	object
ONB	onset of nucleate boiling
r	row
refl	reflection
sat	at saturation conditions
sv	solid-vapour interface
t	total; transversal
v	vapour
w	wall

1. Introduction

This present chapter provides an insight of this thesis framework. The context and motivation are introduced as well as the objectives and valuable contributions proposed in the development of this work. Finally, a brief paragraph outlining the organization of the document is presented.

1.1. Context and motivation

Moore's law states that the number of transistors in an integrated circuit (IC) approximately doubles every two years [1]. In fact, half-century later Moore's prediction held true with uncanny accuracy, in such a way that it has become a mandatory target in every major computer-chip manufacturer. The remarkable fast paced competitiveness in micro-processors development rewards consumers with tremendous advances in computational power and electronic devices. However, this led to an increase in the dissipated thermal power by electronic devices [2] due to exponential increase in the number of elements in subsequently reduced packaging. This constant - and proportional to transistor count - increase of the dissipated thermal power proceeded until 2004, when the Intel Pentium 4 processor appears and becomes known due to severe thermal management failures. To cope with this issue, single-core architecture was replaced by multi-core architectures along with multi-thread software optimization, distributing the computational load across multiple and less powerful processors [3]. However, a decrease in the performance slope is notorious after the multi-thread implementation when considering numerical simulations or computer gaming applications [4]. Hennessy and Patterson [2] state that thermal management of electronic devices is the biggest limitation in the development of new processors in the near future. In fact, the maximum allowed junction temperature (i.e. the highest operating temperature of the actual semiconductor in an electronic device) for reliable operation is of the order of 80°C. Bar-Cohen *et al.* [5] alert for the performance degradation and reliability that this increase in heat dissipation can cause. Moreover, Tonapsi *et al.* [6] state that an increase by 10°C is enough to reduce the device life by half, while Paik *et al.* [7] state that an increase by 15°C can increase time response from 10% to 15%. Cader *et al.* [8] state that the conventional air cooled systems have trouble accompanying the heat flux generated by constant increase of clock frequency and number of transistors. Nowadays it is a common practice to overclock the CPU (Central Processing Unit) in order to take full advantage of the hardware potential of modern processors. However, the overclocked system still demands the dissipation of high thermal loads (e.g., as high as 100 W/cm² as argued by Mudawar [9]), which definitely cannot be achieved by the conventional air forced convection cooling systems. Alternative cooling strategies have been explored within the last decade, being some of them already available in the market, such as water-cooling or heat-pipe heatsinks. (These technologies will be reviewed in Chapter 2). Among them, liquid single-phase cooling or two-phase heat-pipe heatsinks are the more efficient technologies, although they are still widely studied in the literature. Phase-change technologies are considered the most promising heat transfer techniques owing to the latent heat of vaporization, to which typical heat transfer coefficients

are $10^4 W/m^2K$, much higher than $10^2 W/m^2K$, the typical heat transfer coefficient from air-forced convection. Forced convection two-phase micro-channels, spray-cooling or pool boiling among others are widely studied. Considering the latter, in spite of being characterized with a typical lower heat transfer coefficient compared to other two, is in fact considered the most potential solution in the field of electronic cooling due to its inherent lower level of complexity, the higher reliability and ease of manufacture and implementation. However, towards successively decreasing the thermal resistance between the die junction and the cooling mechanism, pool boiling based cooling system often address the direct immersion of the micro-processor into the boiling fluid, which demands for the use of dielectric fluids. The downside of these fluids is that the thermo-physical properties that play a major role in the heat transfer mechanisms are considered poor. For instance, considering HFE-7000, a dielectric fluid manufactured by 3M, its thermal conductivity is 12.9% of that of water under similar conditions, and its latent heat of vaporization is only 6.3%. Hence, turning pool boiling cooling systems into a feasible solution demands for the enhancement of the heat transfer mechanisms. One of the most common strategies is to alter the surface topography, promoting the increase of heat transfer. However, this solution still requires much investigation as the surface properties are related to these mechanisms in a complex and intricate way. Also, commercial solutions based on pool boiling demand for efficient systems allowing perfect balance between the vaporized and condensed mass flow rates and careful design solutions to account for many interdependent variables.

1.2. Objectives and Contribution

Following this context, the present work addresses the investigation, design and development of a benchmark experimental facility based on a two-phase closed loop thermosyphon to infer on the feasibility of pool boiling as an effective alternative cooling technique applied for the cooling of CPU's in desktop computers.

To accurately infer on a CPU cooling technology, and owing to the fact that the dissipated power by a real processor is not easily controlled, an accurate and reliable simulation of a CPU thermal behavior is developed, replicating several boundary conditions and comprising a proper control and acquisition system. This setup, once validated, is intended to act as thermal boundary for the aforementioned pool boiling cooling technology – also to be designed and developed within the scope of this work.

The pool boiling system to be devised is dimensioned by combining boiling and condensation in a closed loop. The design of the system is based on an extensive experimental characterization of the system behavior under steady-state and transient conditions.

Additional parameters should also be addressed such as the surface topography, liquid fill charge, condenser arrangement and positioning, size and orientation of the evaporator, among others.

The system devised here should be modular, to allow proceeding with the optimization campaign towards the development of a custom made product.

1.3. Document structure

The present document is composed of seven main chapters, including this Introduction.

Chapter 2 aims to extend the context of this work by introducing a comprehensive literature review on the most recent advances in cooling technologies currently widely investigated. This allows the reader a more comprehensive understanding of the devised cooling system, compared to the state of the art. Given to the similarity in many relevant issues, with the system developed here, particular emphasis is given to the state of the art of thermosyphons.

Chapter 3 introduces the main physical phenomena involved in the work by means of a theoretical background required for the design process of the cooling system. The basic concepts explained here are also important in the interpretation and discussion of the results, further presented in Chapter 6.

Chapter 4 comprises the study, design and development of a simulated CPU heat source, comprising a validation of the devised simulator with an actual commercially available CPU.

A proof-of-concept prototype developed in the beginning of the work, in order to validate the devised control systems and instrumentation is presented in Chapter 5, together with the developed experimental setup and a detailed design process of the facility and the cooling system. The experimental methodology is also described in this chapter.

Following the discussion of the results, in Chapter 6, Chapter 7 includes the final remarks and proposes the future work.

2. State of the art

2.1. Overview of existing CPU cooling techniques

Despite its extensive use in CPU cooling, and considerable performance improvements have taken place in the last decades, it is generally accepted that traditional air-cooling techniques are about to reach their limit for cooling of high-power applications. For instance, Lasance *et al.* [10] stated that with standard fans a maximum heat transfer coefficient of around $150 W/m^2K$ can be reached with acceptable noise levels.

Cooling techniques alternative to the conventional air-forced convective systems, often deal with liquids, as working fluids, due to their higher heat transfer coefficients, when compared to air. For instance, single phase cooling systems using water can easily reach heat transfer coefficients ranging between 300 and $10000 W/m^2K$. These systems usually comprise a heat sink, cooling the processor, connected to a heat exchanger, which cools the liquid, often based on air-forced convection. Being already a well-established cooling technique, efforts were made in order to optimize the performance of the system as a whole, for example improving the heat removal performance of the water block heat sink or integrating the system with thermoelectric coolers, e.g. [11]. Furthermore being a flexible system it would be also possible to cool at the same time the CPU and the GPU in a personal desktop or to use coolant based on aqueous solution but with anticorrosion and anti-frosting properties [12]. Nano-fluids [13] have also been found to enhance cooling performance. One of the main problems is related to system leakage of a conductive fluid that could damage the device being cooled.

Based on a completely different heat removal mechanism, heat pipes are nowadays still the best alternative cooler available in the market and a subject of intense research. A heat pipe is a two-phase heat transfer device with an extremely high effective thermal conductivity. They are totally passive systems, having no moving parts and requiring no energy to operate. Heat pipes are usually used as an additional structure that is added to a heat sink increasing the thermal performance up to 20% when compared to a typical aluminium or copper base heat sink [14]. The thermal resistance, evaluated as the ratio of the temperature difference between the junction and the ambient temperature, to the heat dissipated by the chip, achievable with this technique was evaluated to be $0.4 ^\circ C/W$ according to [15] and [16]. The performance of heat pipes scales from $10 W/cm^2$ to over $300 W/cm^2$ [10].

Variants of convective heat pipes have been subject of investigation namely vapour chambers and miniature loop heat pipes. The first, according to [17, 18, 19], can remove $96 W/cm^2$ at a temperature difference of only $45^\circ C$, the second, presented an overall thermal resistance of $0.5 ^\circ C/W$ in an air-cooled loop and water-cooled loop heat pipe and with further integration of thermoelectric cooler and two-phase thermosyphons the thermal resistance is further reduced to $0.29 ^\circ C/W$ [20, 21]

Extended research has been performed in the last year concerning heat pipes and a recent review on the technology can be found in [22].

In the context of two-phase systems, two-phase loop thermosyphons, based on nucleate boiling heat transfer, are in the last years attracting the attention of researchers and manufactures in terms of a possible solution for CPU cooling. The interest is due to the fact that an extremely high heat transfer coefficient is reachable by mean of the boiling process ($3000-60000 W/m^2K$). A literature review focusing on this technique, which is the one of interest of this thesis, will be given in the next sub-chapter.

Despite not being yet a solution ready for the market, micro-channels, operating in single phase or convective flow boiling conditions, are extremely efficient in removing large amount of heat from a compact space.

In the context of single phase, in [23] a micro-channel heat exchanger thermal resistance of only $0.1 ^\circ C/W$ and an overall thermal resistance of $0.23 ^\circ C/W$ for the whole liquid cooling system was successfully achieved.

Convective flow boiling in micro-channels can provide even higher heat transfer coefficients, e.g. [24] [25] in which the heat transfer coefficient measured experimentally were at maximum $11764 W/m^2K$ (2001). Although these values make micro-channel heat sinks an attractive solution for CPU cooling, [26] inferred that due to large discrepancies and dispersion of results reported in the literature, reliable prediction of the heat transfer rates and pressure drops in micro-channels is not available for design applications such as micro-channel heat sinks.

As an extreme solution, micro-channels heat sinks could also be integrated in vapor compression refrigeration. Adaptation of conventional vapor compression refrigeration for CPU cooling is an extremely hard task, which requires miniaturization. In any case experimental results show the potentiality of this vapor compression refrigeration for CPU cooling. For instance in [27] using micro-channel heat exchangers achieved to remove a heat flux of $154 W/cm^2$. In [28] the system was able to dissipate CPU heat fluxes of approximately $40-75 W/cm^2$ and keep the junction temperature below $85^\circ C$ for a chip size of $1.9 cm^2$. The system has an overall system thermal resistance between 0.02 to $0.42 ^\circ C cm^2/W$, the chip heat dissipation rate was between 176 and $226 W$ and the chip surface temperature was between $34-53 ^\circ C$.

In recent years also spray cooling has received increasing attention as a possible candidate for CPU cooling applications. Mudawar *et al.* [9] have shown that spray impingement cooling is one of the most efficient technologies for heat flux removal per unit of fluid flow. Performance could be enhanced by micro-structured surfaces, for instance Bostanci *et al.* [29] or by mean of intermittent spray cooling [30].

From this brief literature review one can conclude that several CPU cooling technique have been proposed and evaluated in the past and up to now. Anyway those that reached the market are only forced air convection (fin fan cooling), heat pipes and forced liquid convection (liquid cooling). All the

others are still been studied in laboratory environment. Spray cooling and micro-channels are extremely promising and efficient in terms of heat removal, but complexity and cost of implementation could be prohibitive for an application such as CPU cooling. Two-phase thermosyphon seem in this context to be the next candidate to effectively being employed as a CPU cooling solution. The following literature review will present some of the research performed in this direction.

2.2. Two-phase closed loop thermosyphon: parametric research and implementation in the context of CPU cooling

A two-phase closed loop thermosyphon consists in an evaporator and a condenser, which are connected through a passage, or a loop. Heat is transferred from the source through an interface to the evaporator, where the fluid removes heat thanks to the nucleate boiling mechanism. At the solid-liquid interface, vapour is generated. The released heat is dissipated to the ambient from the condenser and the condensed liquid is returned to the evaporator, thus completing a closed loop. The density difference between the liquid and vapour creates a pressure head, which drives the flow through the loop, and as such no driving force is needed.

Differently from pipe thermosyphons, closed loop thermosyphon allows to decouple the condensation and the evaporation system. This makes it suitable to be used to remove high heat rates, while providing an additional advantage in terms of custom made design for applications which are very restricted by the available space (as in the case of the cooling of CPU's in desktops).

A considerable number of studies can be found in the literature, addressing the use of thermosyphon as a cooling device. Particularly, experimental research was conducted to study the effect of the various operational parameters.

In this context, in [31] the quantity of working fluid was shown to influence the thermal performance and so it was optimized in a two-phase loop thermosyphon system capable to remove heat flux of $12 W/cm^2$. It was shown that 30-40 ml was reasonable for water and acetone and for FC-87 40-50 ml delivered satisfying results. Increasing the quantity of working fluid would decrease the thermal performance of the system.

The presence of non-condensable gas was subject of investigation in [32]. Despite the completely different operating conditions the authors agreed that the cooling performance of a thermosyphon deteriorates with an increasing amount of non-condensable gases. This effect was so strong that the performance of the system resulted lower than conventional air forced convection cooling.

The pressure has a significant effect on the boiling heat transfer coefficient of the thermosyphon evaporator. It was found [33] that the heat transfer coefficient at most points at a given heat flux was larger at the higher values of reduced pressure.

Surface micro-structure can increase the cooling performance of the evaporator. In a recent study from [34] the authors tested four kinds of heat transfer surfaces of the evaporator: smooth, blasted, copper-plated and finned surfaces. The latter resulted as the best performing one. A more detailed description of the underlying physical phenomena related with structured surfaces will be given in the next chapter.

Differently from the previous mentioned work, other studies address the mutual influence of some of the parameters characterizing two-phase loop thermosyphons. For instance [35] studied the effect of the evaporator inclination (from 0° to 90°) and the effect of varying the liquid fill volume. They reported a slight improvement in the boiling performance for a vertical orientation and negligible effect of variation in liquid volume as long as the boiling surface is submerged. Enhanced micro-structured surfaces were also used resulting in almost a 2.5 fold increase in heat transfer compared to a solid block of the same size. Later, the same author also studied the combined effects of sub-cooling and operating pressure on the performance of the thermosyphon. Results show that a partial vacuum at all heat fluxes results in better performance compared to higher pressures. Sub-cooling resulted in a negligible effect in the system.

In [36] the experimental parameters tested were the evaporator surface type and working fluid fill ratio. The condenser thermal resistance clearly increased with increasing liquid volume. A groove-type evaporator surface with 0.2 mm height and 1 mm width had the best performance, decreasing the evaporator thermal resistance about 15.5% compared to a smooth surface.

All the works previously reported were mainly focused on the optimization of the evaporation section, or in separate analyses of the evaporator and the condenser. Studies focusing more in the optimization of the system in a whole and in the definition of the complete thermodynamic cycle were recently reported. In this context, in [37] transient and steady-state analysis of the thermosyphon loop efficiency, the temperature distributions, and the thermal resistance as a function of heat load were studied. Moreover, different working fluid filling ratios were tested and the results show that the optimal volumetric filling ratio was about 9.2%. The results showed that the maximum heat load obtained with the thermosyphon loop cooling system was twice as important as that given by a traditional cooling system.

In [38], similarly to the previously reported study, thermal resistance analysis of system, loop, evaporator, vapour line, condenser, and liquid volume were addressed additionally to the pressure and temperature evolutions for the better understand of the main parameters affecting the cooling system performance. The effects of fill charge ratio, the condenser jacket coolant inlet temperature and the mass flow rate were also investigated. The optimal fill charge ratio resulted to be between 7% and 10%, the cooling system presented the optimal performance when controlling the condenser jacket water temperature and flow rate at $5\text{ }^\circ\text{C}$ and at 0.7 l/min respectively.

Despite the large amount of work performed to characterize influencing parameters in two-phase loop thermosyphons, only few publications were found in literature dealing with the possibility of the implementation of such technique as a CPU cooling solution. In this context, [39] proposed the concept of an air-cooled thermosyphon heat rejection device, intended to reject 100 *W* (or more) from the CPU of a desktop computer or server. This concept is believed to represent the highest performance that has been reported for an air-cooled heat rejection system. A working fluid is boiled in a small chamber mounted on the CPU, and the vapour is condensed in the tubes of the remotely located air-cooled condenser. Under laboratory conditions, their system was able to dissipate 100 *W* for a maximum boiling surface temperature of 70°C.

[40] were the first to verify the performance hypotheses and demonstrate the effectiveness of two-phase thermosyphons as a passive cooling solution for two HP computer systems. Their system was capable of dissipating 85 *W* while keeping chip temperature below 85°C. In their tests water was identified as the best working fluid with respect to dielectric liquid; however, optimum charging and proper degassing may have improved the qualities of dielectric liquid as a working fluid. The thermal performance of the thermosyphon was also found to be unaffected for large inclination angles. Natural convection case was found to be inefficient; however a change in design may make the condenser more efficient.

In [41] a closed-loop two-phase thermosyphon with Fluorinert (FC-72) as working fluid was experimentally investigated as a cooling solution for CPU. Four possible boiling surfaces of an evaporator were examined: smooth, rough, smooth with plate fins and rough with plate fins. The last evaporator showed the highest performance, i.e., it reduced the temperature at the evaporator/heater interface by about 18% in comparison with that of the smooth surface evaporator. The effects of the volumetric amount of Fluorinert liquid in the thermosyphon, on the heat transfer were also addressed, showing that the temperature of the evaporator surface was nearly constant at various charged volume. The authors claimed that the thermal resistance (1.83 °C/*W* at heat input 30 *W*) was significantly lower compared to the systems used in practice, and therefore the present system had a potential to be one of the most effective cooling methods for notebook computers.

In [42] a new micro-porous metallic coating method was used to produce two compact boiler assemblies for use in thermosyphons for CPU cooling. These assemblies were tested using a segregated hydrofluoroether (HFE) working fluid C₃F₇OCH₃. The boiler assembly was incorporated into a thermosyphon with a remote finned-tube condenser. The so realized thermosyphon was tested yielding values of sink-to-fluid resistances of 0.083, 0.026 and 0.014 °C/*W* at 150 *W*. Data gathered with larger condensers or more powerful fans suggested that it would be quite practical to produce a compact thermosyphon that could cool a 20mm device generating 250 *W* with sink to ambient thermal resistance lower than 0.10 °C/*W*, a performance level competitive with forced water systems.

3. Theoretical background

This chapter introduces the theoretical concepts that were required for the design and development of the cooling system. Pool boiling is the major heat transfer mechanism occurring in a two-phase thermosyphon. Hence, the fundamentals of nucleate pool boiling heat transfer are revised in the sub-chapter 3.1. The system designed here considers the possibility of the CPU to be working in the horizontal or in the vertical positions, despite the later is, in fact the most used in the configuration of the majority of the desktops. Hence, pool boiling on vertical surfaces is also briefly addressed in sub-chapter 3.1.3.

An important approach followed in the development of this system addresses the use of micro-structured surfaces for heat transfer enhancement. In this context, the numerous studies which have been performed on pool boiling on modified surfaces are revised in sub-chapter 3.2, to support the strategy that was followed in the present study to select the micro-patterns to test.

Finally, the theoretical background on condensation inside tubes, which is required to design the condenser, is introduced in sub-chapter 3.3.

3.1. Fundamentals of Nucleate Pool Boiling Heat Transfer

3.1.1. Boiling curve

Figure 3.1 illustrates a typical boiling curve, as experimentally obtained by researchers such as Nukiyama [43], Jacob and Linke [44], and Drew and Mueller [45]. The boiling curve represents the relation between an imposed heat flux and the resulting wall superheat, i.e. the difference between the surface temperature and the saturation temperature of the working fluid. Different boiling regimes can be identified, namely the single-phase natural convection, nucleate pool boiling, transition boiling and film boiling.

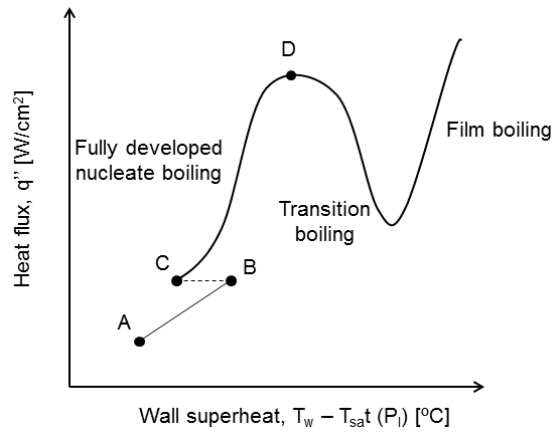


Figure 3.1 – Boiling curve for a horizontal plain surface.

Single-phase natural convection heat transfer is the underlying physical mechanism occurring on a pool of saturated liquid when low heat flux is applied. A thermal boundary layer is created near the heated surface. This thermal gradient causes the superheated liquid to circulate, buoyed from the hot surface onto the liquid-vapour interface, where it eventually evaporates. In Figure 3.1 this regime is identified from point A to B. The onset of nucleate boiling occurs at point B, at which bubble embryo starts to grow on imperfections or cavities etched in the surface that contain pre-existing vapour nuclei. The bubbles grow to a certain size before departure, being this diameter dependent on the surface tension in the liquid-vapour interface, buoyancy force, temperature and pressure. Continuous evaporation supports the cycle of bubble grow and departure, enhancing the overall transport of heat from the surface, thus significantly decreasing the wall superheat at constant heat flux. This sudden decrease in temperature is referred to incipience overshoot. Due to lower surface tension of dielectric fluids, the wall superheat at the onset may be delayed thus increasing this overshoot. This behaviour is not observed when decreasing the heat flux, due to the hysteresis effects. A comprehensive review on this phenomenon is provided by Bar-Cohen and Simon [46]. From this point and beyond, isolated bubbles are released from the surface. As the wall superheat is raised, the number of nucleation sites increase and the constant release of bubbles induce a considerable fluid circulation near the surface, increasing the heat transfer coefficient. Most of the cooling and refrigeration equipment operates within the fully developed nucleate boiling regime, (defined between points C and D) due to the steep slope of the boiling curve in this region. In the present work, the cooling system is also designed to operate in this region. As one approaches point D, bubbles at a given site begin to merge in the vertical direction and the heat transfer coefficient starts to decline. Thus, this region of the curve (still in the regime of the fully developed nucleate boiling) is characterized by the decrease in the slope of the boiling curve. Vapour appears to leave the heated surface in the form of jets or columns, which subsequently merge into vapour slugs. Interference between the densely populated bubbles inhibits the motion of liquid near the surface thus causing a decrease of the heat transfer coefficient. This region corresponds to an inflection of the boiling curve, where the heat transfer coefficient reaches the maximum value. From this point beyond, the strong coalesce generates large bubbles blocking the liquid supply to the nucleation sites and reducing drastically the heat transfer coefficient. This turning point is referred to as critical heat flux. In the context of cooling applications, the critical heat flux

establishes the limiting working condition. In fact, in the following regime, the so-called transition boiling, increasing localized dry-out is caused by the formation of large vapour bubbles on several regions of the surface, leading to an exponential decrease of the heat transfer coefficient. When no liquid is in contact with the surface, a vapour blanket fully covers the surface and a sudden critical heat flux is attained characterized by a sudden increase in the surface temperature. Film boiling is initiated with the establishment of a vapour insulating layer over the surface, so that evaporation occurs at the liquid-vapour interface.

Focusing on nucleate boiling heat transfer, several authors proposed semi-empirical correlations predicting the relation between heat flux and wall superheat on the heating surface, starting from the pioneering studies of Rohsenow [47], Foster-Zuber [48] or Stephan-Abdelsalam [49] among others. Comparing the correlations devised by different authors, even if the detailed parameters differ between them, the nucleate boiling heat flux q''_{NB} may be expressed as follows:

$$q''_{NB} = f(\text{fluid property, surface characteristics}) \cdot [T_w - T_{sat}(P_l)]^a \quad (3.1)$$

Perhaps the best known nucleate boiling heat transfer correlation was proposed by Rohsenow [47]:

$$q''_{NB} = \mu_l h_{fg} \left[\frac{g(\rho_l - \rho_v)}{\sigma} \right]^{\frac{1}{2}} \left(\frac{c_{pl} \Delta T_{sat}}{C_{sf} h_{fg} Pr_l^{m+1}} \right)^{\frac{1}{n}} \quad (3.2)$$

where σ is the surface tension, h_{fg} is the latent heat of vaporization, μ_l is the viscosity of liquid working fluid, g the gravity, c_{pl} is the specific heat constant, $\Delta T_{sat} = T_w - T_{sat}(P_l)$ is the surface superheat and q'' is the heat flux across heating surface. Pr is the Prandtl number $Pr = c_p \mu / k$. Values of C_{sf} , m and n , are fitting constants that take into account the properties of the surface (mainly the wettability associated to the contact angle and the micro-roughness) and their effect in the nucleation site intensity. Despite its popularity, Rohsenow's correlation must be used with care. All the correlations have an empirical nature associated to the particular experimental conditions for which they were devised. In this case the fitting coefficients related to the properties of the fluids are consistently confirmed by several authors, but the coefficient associated to the surface properties may vary significantly, e.g. [50, 34]

Few authors also proposed correlations to predict the critical heat flux. Hence, besides Rohsenow [47], Kutateladze [51] and Zuber [52] proposed a theoretical explanation for the CHF phenomena in their hydrodynamic theory based on Kelvin-Helmholtz instability. According to this theory, CHF occurs when the surface-fluid interface is disrupted as the result of the velocity difference between the ascending vapour column and the liquid descending due to gravity. The CHF expression can be approximated as

$$q''_{max} = Ch_{fg}\rho_v \left[\frac{\sigma g(\rho_l - \rho_v)}{\rho_v^2} \right]^{\frac{1}{4}} \quad (3.3)$$

where the constant C is a correction factor accounting for different heater geometries. $C = \pi/24$ is the recommended factor by Zuber for a variety of finite geometries and $C = 0.149$ is recommended for large plates. If the characteristic length of the heater L is small, such that the Confinement number, $Co = \sqrt{\sigma/(g[\rho_l - \rho_v])}/L$ is greater than 0.2, a correction factor must be added [53].

This theory does not successfully predict the CHF in many current working conditions. One of the reasons pointed for this is the fact that the surface characteristics such as wettability are not taken into account. In this context, Kim *et al.* [54] showed that surface characteristics of modified surfaces are effective in the value of CHF whereas they are not accounted for in the hydrodynamic instability theory, but could be included in the hot/dry spot theory. Based on this argument, alternative correlations were also proposed, for instance by Kandlikar [55]. Although some authors (e.g. Gerardi *et al.* [56]) report better agreement for these correlations addressing the effect of surface properties, they still often require custom fitting when applied to data obtained from diverse working conditions.

3.1.2. Physical Mechanism of Boiling heat transfer

According to Hsu and Graham [57] there are three main mechanisms which characterize the heat transfer during the nucleate pool boiling process, namely bubble agitation, vapour-liquid exchange and evaporation. While the first two mechanisms are both modes of convection to the liquid, the evaporation mechanism is a latent heat transfer. Bubble agitation is the mechanism at which the growth and departure of bubbles agitates the adjacent liquid, creating an intermittent pumping motion. The displacement of super-heated liquid transports sensible heat away from the thermal boundary layer. This mechanism can be considered as a forced convection process given that the velocity of the liquid is influenced by the rate of bubble growth. The vapour-liquid exchange consists on the cyclical detachment of vapour bubbles from the surface allowing the cold liquid to quench the hot surface. With the thermal boundary layer being disrupted by the departing bubble, the rate of sensible heat removal is proportional to various factors such as, thickness and temperature of boundary layer, number of nucleation sites, and the bubble departure frequency and diameter. These mechanisms contribute to the augmentation of the overall convection to the liquid. Finally, in the evaporation, phase change occurs at the bubble interface, from the superheated liquid that surrounds the bubble and from the liquid micro-layer squeezed in between the growing bubble and the heated surface. These are the main mechanisms also identified in the so-called RPI model (Kurul & Podowski [58] who in addition also consider the natural convection). So, the coexistence of these three mechanisms contributes to the extremely high heat transfer coefficients achievable during nucleate pool boiling.

In the region of fully developed nucleate boiling regime, one should expect that the evaporation process would be the dominant mode of heat transfer. However, experimental results from Han and Griffith [59] and more recently from Gerardi *et al.* [60], show that the contribution of the quenching of

the cold liquid on the heated surface is also relevant and in several working conditions, may actually be the governing mechanism.

3.1.3. Pool boiling from vertically oriented surfaces

Boiling on a heated large vertical surface is qualitatively similar to that on a horizontal surface, except for the upward liquid and vapour velocities caused by natural convection. This often results in a cooler liquid and a lower surface temperature at lower elevations of the vertical plate, and a progression through the various types of boiling regimes as the flow proceeds upwards. Boiling begins near the bottom of the surface and the bubbles increase in size and diameter as they are convected upwards. If the surface is large enough, at a certain elevation, boiling crisis occurs where eventually all the rising bubbles coalesce and this marks the transition to film boiling. At this point the surface temperature increases abruptly, similarly to what happens in film boiling in a horizontal surface. Film boiling in vertical surfaces has been deeply investigated due to modern application (e.g. [61]) but surprisingly, information concerning nucleate pool boiling is still scarcely found on the open literature. Ishigai *et al.* [62] report that the CHF decreases with increasing heater area. Thus, focusing on small surfaces where transition does not occur, nucleate boiling heat transfer is still very difficult to predict. Howard and Mudawar [63] performed a review study on the critical heat flux as function of surface orientation, as presented in Figure 3.2.

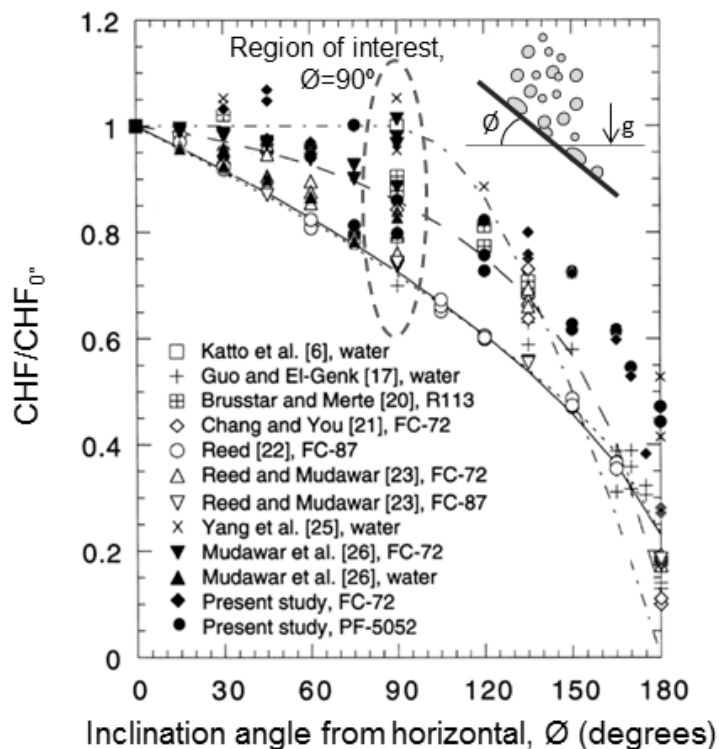


Figure 3.2 – Review of effects of orientation on CHF. Refer to [63] for the references in legend.

Given that the focus of interest for the current work is only for the 90 degrees orientation, despite the scattered information, mostly due to dimensional effects, one can argue that the critical heat flux for boiling on a surface oriented at 90° is lower than that obtained for a horizontally placed surface. In fact

at high heat flux conditions, vertical pool boiling exhibits vapour production flow patterns similar to those found in flow boiling. A fairly continuous wavy vapour layer involves the heated surface, where intermittent wetting occurs. As the heat flux is further increased, the individual bubbles coalesce to form large oblong vapour bubbles. Critical heat flux is triggered when the normal momentum of the vapour produced in the wetting front exceeds the pressure force exerted upon the interface, due to interfacial curvature and the wetting front of each large bubble is lifted from the heater surface. However, concerning the heat transfer coefficient at smaller heat fluxes, for instance Nishikawa *et al.* [64] states that using water at ambient pressure, in the low heat flux region the heat transfer coefficient increases remarkably as the inclination angle is increased, and there is no marked effect in the high heat flux region. Mohamad and Bostanci [65] using a similar dielectric working fluid (HFE-7100) conclude that for high surface superheats the heat transfer coefficient decreases with increasing angle, but increases with tilt angle for lower superheats. Two extra mechanisms of sensible heat removal play a role in vertically oriented surfaces: the sensible heat transport by compulsory removal of the thermal boundary layer by the raising bubble along the boundary layer and the latent heat transport by evaporation from the micro-layer of the liquid film squeezed underneath the rising bubble.

3.2. Boiling on Enhanced Surfaces

One of the most used approaches to enhance pool boiling heat transfer consists in altering the surface topography and/or wettability. Jakob [66] was one of the first authors reporting that changing surface roughness can considerably affect the shape of the aforementioned boiling curve. Ever since, the theory that boiling bubbles are emanated from crevices that can entrap air or vapor within them has been further investigated, leading to several parametric studies on surface structuring to enhance heat transfer coefficient or critical heat flux. For instance, Kim *et al.* [67] recently published a detailed review paper on the recent advances in fabrication techniques and outlined some relevant recent studies on this topic. Poniewski and Thome [68] extensively review the theoretical background on this subject.

Several different types of surface structuring have been proposed in the literature, such as differently shaped cavities, pillars, fins or stochastic roughness. Among these, surfaces with etched or laser drilled cavities have been found to be effective in enhancing the heterogeneous nucleation process. (e.g. Teodori *et al.* [34]). In fact, these re-entrant cavities are able to nucleate at very low wall superheats with respect to plain surfaces. Usually, etched surfaces have 2 to 4 times more wetted surface area, while more complex shaped cavities could attain ratios from 4 to 10 times those of a plain surface. Besides this obvious improvement, several mechanisms coexist. For instance, depending upon the type of cavity, a thin film evaporation forms on the extensive inner walls and, in corners, liquid menisci evaporate as heat is conducted into the liquid. Also, liquid phase is pumped in and back out of the re-entrant cavity by the action of the surrounding bubble agitation. Concerning the external nucleate boiling convection mechanisms, the high density and departure frequency of the bubbles emerging from the cavities accentuates the heat transfer due to bubble agitation and thermal boundary layer stripping. Concerning the overall performance increase, Yu *et al.* [69] reported an

increase in the heat transfer coefficient as high as 150% for the boiling of the dielectric fluid FC-72 on surfaces micro-patterned with circular cavities of diameters ranging from 50 to 200 μm , depths of 110 to 200 μm , and distance between cavities from 100 to 400 μm . Nitesh *et al.* [70] reported an increase in the heat transfer coefficient of 50% for the pool boiling of FC 72 on surfaces micro-patterned with pyramidal cavities of mouth dimensions of 40 μm and base dimensions of 240 μm . The spacing between the cavities was diverse from 500 to 1000 μm . Several other analogous studies are found in the literature. However, no agreement is found concerning the optimal micro-pattern, resulting in a common trial and error approach that is not desirable. Fixing the size and shape of the cavities, Moita *et al.* [71] and Teodori *et al.* [72] studied the boiling of water, ethanol, and HFE-7000 on micro-patterned surfaces where the only quantity that was changed was the distance between cavities, ranging from 300 to 1200 μm . The authors observed an increment in the heat transfer coefficients as high as 150% and discussed the relevance of the distance between cavities in such enhancement. The authors conclude that considering the increase in surface contact area and the increase of cavities density and consequently of the number of potential nucleation sites, it would be unrealistic to consider that these two parameters linearly affect the heat transfer coefficient. In fact, Yu *et al.* [69], Nitesh *et al.* [70], Moita *et al.* [71], and Teodori *et al.* [72] observed that changing the spacing between cavities influences the interaction mechanisms, which in turn affect boiling performance. These observations are in agreement with the pioneering work of e.g. Chekanov [73] who reported that the distance between cavities is a characteristic parameter that plays a vital role in defining the regimes for the different interaction mechanisms involved in the heterogeneous nucleate boiling process.

Based on this trend, the present work follows the approach of Moita *et al.* [71] and Teodori *et al.* [72] and fixes the shape and size of the cavities, based on their experimental results. Then different patterns are tested to infer on the effect of the distance between cavities.

3.3. Condensation inside tubes

The devised thermosyphon cooling system comprises a condenser heat exchanger where vapour formed within the boiling process arises and undergoes a phase change returning to the liquid phase and closing the loop. This section introduces the basic theoretical background required to predict the convective condensation heat transfer coefficient, which in turn is needed to properly address the design of the condenser, which comprises horizontal tubes.

Figure 3.3 illustrates the flow pattern map and regimes experienced in a horizontal two-phase flow, inside a tube, as described by Bell *et al.* [74], who followed the pioneer work of Baker [75].

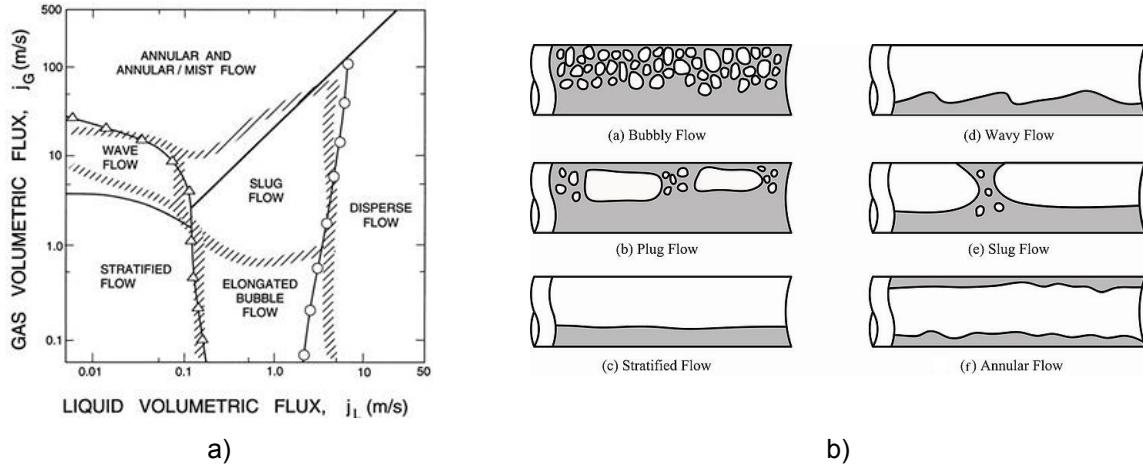


Figure 3.3 – a) Baker flow pattern map; b) Flow regimes illustration (grey = liquid, white = vapour)

In this present work, the regime of interest is the stratified flow regime, in which both liquid and vapour phases have very low velocities and low interfacial shear forces. In fact, this regime is also the one that maximizes heat transfer due to the reduced liquid film thickness resistance. For this condition, the condensation process on the inside perimeter around the top and sides of the tube is very similar to that on the outside of a horizontal tube. Thus, Nusselt falling film analysis, as proposed by Chato [76] may be modified by means of a correction factor and applied to the upper zone of the tube, where liquid film resistance applies. The liquid pool collected in the lower part of the tube is implied as the angle 2ϕ from the tube center to the chord forming the liquid level. Thus, the modified Nusselt theory proposed by Chato is given by:

$$\bar{h}_f = F \left[\frac{\rho_f (\rho_f - \rho_g) g h'_{fg} k_f^3}{D \mu_f (T_{sat} - T_w)} \right]^{1/4} \quad (3.4)$$

where ρ_f and ρ_g are the fluid and vapour densities, g the gravity acceleration, k_f the thermal conductivity of the fluid, D the inner diameter of the tube, μ_f is the fluid viscosity, T_{sat} and T_w are the saturation and wall temperatures. Following Chato's formulation, the modified latent heat is:

$$h'_{fg} = h_{fg} + 0.68 c_{p,l} (T_{sat} - T_w) \quad (3.5)$$

where h_{fg} is the latent heat of vaporization and $c_{p,l}$ the liquid heat capacity. The correction F factor is calculated according to

$$F = \left(1 - \frac{\phi}{\pi} \right) F' \quad (3.6)$$

Table 3.1 depicts the F' and F values as function of ϕ .

Table 3.1 – Values of the factors F and F' for laminar film stratified condensation in a horizontal tube [77].

ϕ°	F'	F
0	0.725	0.725
10	0.754	0.712
20	0.775	0.689
30	0.793	0.661
40	0.808	0.629
50	0.822	0.594
60	0.835	0.557
70	0.846	0.517
80	0.857	0.476
90	0.866	0.433
100	0.874	0.389
110	0.881	0.343
120	0.887	0.296
130	0.892	0.248
140	0.896	0.199
150	0.899	0.150
160	0.902	0.100
170	0.903	0.050
180	-	0

Chato concluded that the heat transfer coefficient was not particularly sensitive to the 2ϕ angle and suggested to use a mean value of 120° if the vapour is assumed to be stagnant. Carey [78] suggested a more comprehensive correction factor:

$$F = 0.728 \left[1 + \frac{1-x}{x} \left(\frac{\rho_g}{\rho_f} \right)^{2/3} \right]^{-3/4} \quad (3.7)$$

where x is the vapour quality. Recently, Ould Didi *et al.* [79] have experimentally validated Carey's correction factor within $\pm 18\%$ accuracy with experimental data.

In the past few years, Lips & Meyer published several studies concerning the inclination effect on the enhancement of the heat transfer coefficient in condensation occurring inside tubes [80] [81] [82]. These authors show that, since the heat transfer coefficient is strongly dependent on the flow pattern and the liquid film thickness, the influence of gravity caused by orientation effects strongly influence the liquid film thickness and thus its thermal resistance. An enhanced hydraulic gradient reduces the liquid film thickness at slightly downwards facing tilt angle $-15^\circ < \phi < -30^\circ$ (See Figure 3.4) but a higher inclination angle $\phi > 30^\circ$ promotes annular flow even for small mass vapor velocities, since the liquid film spreads equally through the interior tube wall, decreasing the heat transfer coefficient. The fluid distribution that maximizes heat transfer is a result of a balance between gravitational, shear and capillary forces. The increase of heat transfer can be up to 20% for an inclination angle of 15° downward flow [81].

Figure 3.4 depicts an illustrative example of the inclination effects for R134a under different vapour inlet qualities and saturation temperature.

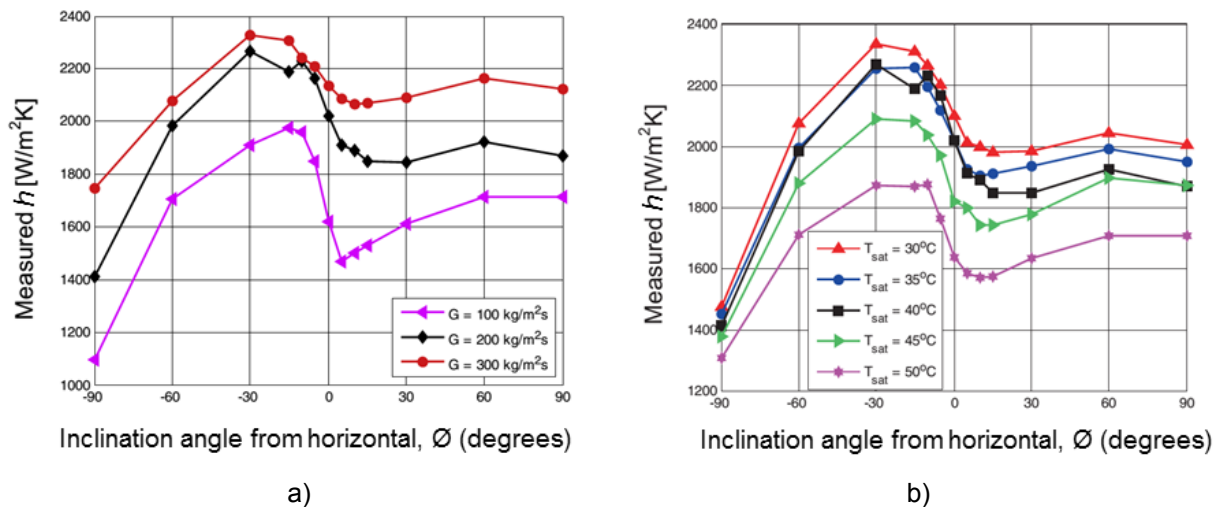


Figure 3.4 – a) Heat transfer coefficient as function of tilt angle for several mass fluxes and $x = 0.25$; b) Optimum angle for different saturation temperature and $x = 0.25$ [80].

The authors conclude that the beneficial inclination effect is also more pronounced with low mass fluxes, low mean vapour qualities and high saturation temperatures. For very low mass fluxes, the optimal inclination angle is placed between 15° and 30° downward facing orientation [80]. An extensive review on this subject can be found in Lips & Meyer [82].

A reflux condenser is a gravity-led system in which vapour is flowing upwards and liquid flows downwards in the same tube. Fiedler *et al.* [83] studied the effect of the inclination angle on heat transfer in a 7mm diameter tube filled with R134a which the most relevant results are summarized in Figure 3.5.

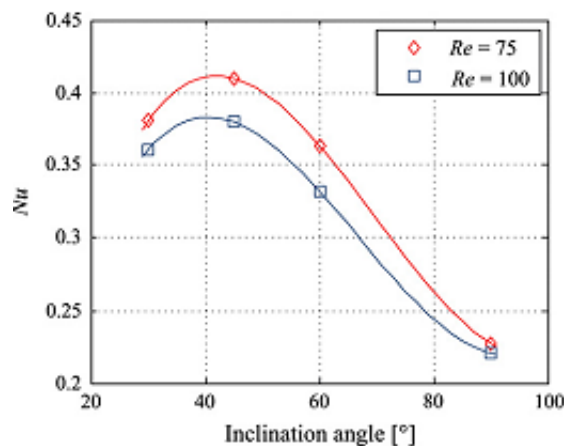


Figure 3.5 – Effect of inclination angle on reflux condensation heat transfer for a 7 mm tube and R134a [83].

Fiedler *et al.* [83] claim an increase in the Nusselt number by a factor of 2, for an upward facing angle close to 40° , and almost as high as the value obtained for the vertical position. Another extensive study on this topic was performed by Klahm and Auracher [84] comprising circular and rectangular

cross-section channels. The authors conclude that for a circular tube the optimum angle is 45° , while for a rectangular channel is between 30° and 45° .

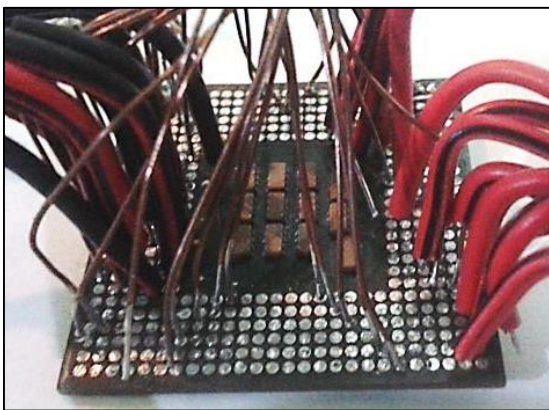
The present study addresses the design of a condenser comprised by horizontal tubes. Besides, its dimensioning, additional tests will be performed to optimize the inclination angle. Also, a reflux configuration will be tested.

4. CPU thermal simulation

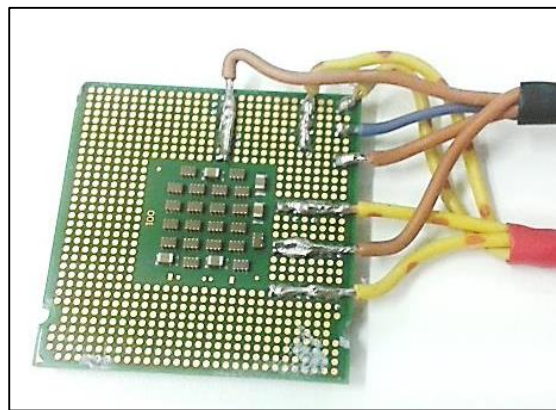
4.1. Overview

The cooling system to be developed should be tested under accurate boundary conditions, which are representative of the real working conditions, namely the heat input which has to be similar to that dissipated by an actual CPU, in both steady and transient conditions. Replicating such conditions is not an easy task due to the complex mechanism responsible for the heat dissipation of a CPU.

In this context, efforts were done to use an actual CPU instead of a simulated heat source. Due to the known issues in thermal management of the Intel Pentium 4, A 2.0GHz Pentium 4 and a last generation 3.4GHz Pentium 4 were used and, by inspection of the corresponding datasheet, power pins were welded and connected to a power supply. This operation saturates the transistors inside allowing the processor to generate heat by means of the Joule effect.



a)



b)

Figure 4.1 – a) Intel Pentium 4 2.0GHz, bottom view; b) Intel Pentium 4 3.4GHz, bottom view

Modern processors work with very low voltage in order to avoid current leakage between components. This means that very high current is required to supply the correct power to the CPU. For instance, up to 70A of current is required for the 3.4GHz processor (Figure 4.1) to dissipate the maximum TDP (Thermal Design Power – i.e, typical power dissipation under extreme load) power of 84 W. Unfortunately, this amount of current could not be delivered by the equipment available in the Laboratory.

Nevertheless, using a HP 6274B DC power supply, one could still provide the maximum of 16A of current to the processor. The internal resistance of the CPU with all the transistors already saturated, which was measured with a digital multimeter, was found to be 0.0754 Ω . Hence, for this 16A current input, this setup could dissipate up to 20 W.

Also, this set-up does not allow establishing well defined and controlled boundary conditions, required to characterize the developed system. So, the thermal behaviour of the CPU was simulated, following the approach described in the next paragraphs. Although 20 W is a very low value compared to the power dissipated by modern desktop processors, it is sufficient to validate the thermal response of the devise CPU simulator.

Modern desktop CPU's are comprised by a substrate made of fiber-reinforced resin, which supports the entire package and where gold pins are welded to contact with the System Board (Figure 4.2). On the top of the substrate, the silicone die is attached. This semiconductor material contains all the active elements of a CPU comprising any number of cores where the transistors actually reside. This is physically the component responsible for heat generation. Heat loss is removed through the Integrated Heat Spreader (IHS), which is made of a nickel-plated copper alloy. The IHS is in contact with the die by means of a highly conductive Thermal Interface Material (TIM), also known as thermal grease. Heat generated is removed from the entire package through a heatsink placed on top of the IHS and using thermal grease in the interface to reduce contact resistance.

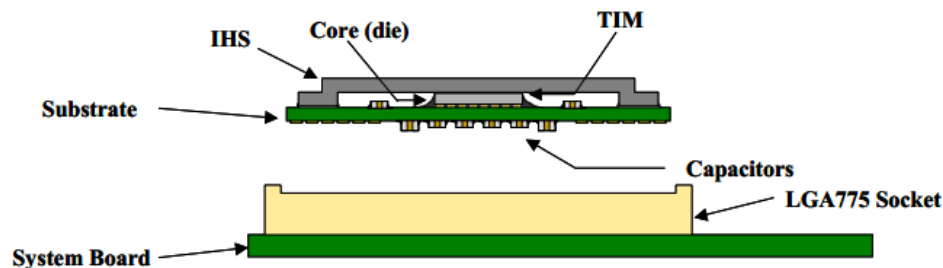


Figure 4.2 – Intel i7 processor package components

Moita [85] developed a CPU simulated heat-source, using two high-power resistors coupled to a cooper plate with the same dimensions as the IHS of an Intel Pentium 4. Moita [85] claims that in spite of the resistive load could replicate the expected steady-state surface temperature, for a given applied power, it was unable to reproduce transient conditions, given that the surface of the copper plate took several minutes to reach the expected temperature, even in natural-convection conditions. Indeed, the power density of the resistors used by Moita [85], or any cartridge heater commonly available is much lower than the power density of a processor die, which nowadays dissipates up to 130 W on a $65\text{--}180\text{ nm}$ thickness die. Due to the abovementioned reason, Moita [85], followed by Guerreiro [30], used a transistor and a copper plate to simulate the die of a CPU.

4.2. Transistor as a die simulator

Although in a different scale, the transistor is in fact the fundamental building element of a processor's core integrated circuit. In the context of a logic processor, a transistor is a semiconductor device used as electronic switch that can be either in an "on" or "off" state (1 or 0). In a N-channel transistor (NPN) a positive current applied to the Base terminal of the transistor changes the internal resistance between the Collector and Emitter allowing the current to flow between these terminals (Figure 4.3). In an off-state, the semiconductor has a virtually infinite resistance, blocking the current flow, and in an

on-state it has a very low internal resistance allowing the signal to pass. However, the disadvantage of a transistor in this application is that this change of state is not an instantaneous event, i.e., the internal resistance changes from zero to infinite continuously and in a finite amount of time dissipating heat due to Joule effect in every state change, thus proportional to the operating frequency.

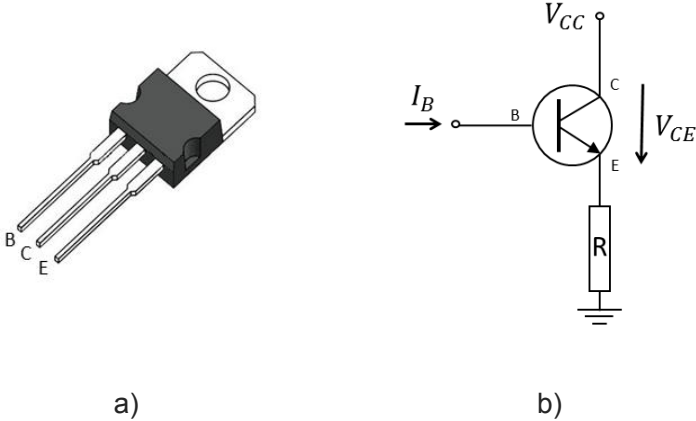
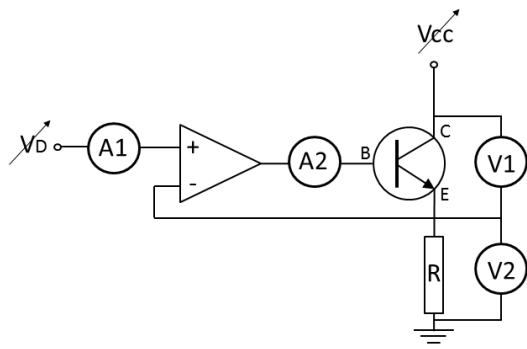


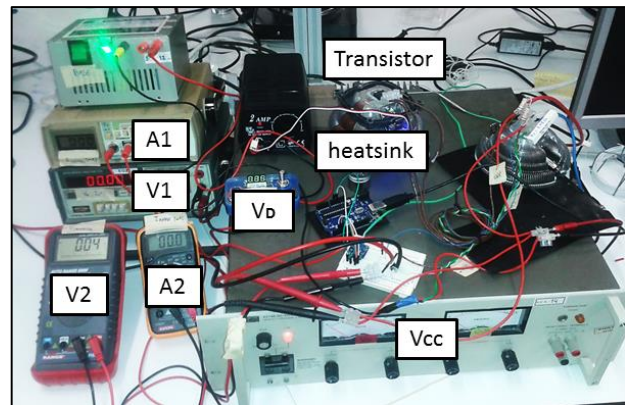
Figure 4.3 – a) N-channel transistor package; b) Connection circuit diagram

If a transistor is used as a current amplifier instead of a switch, the dissipated heat becomes even more dramatic owing to the electrical power blocked by the transistor that has to be thermally dissipated. The gain β of a transistor is quantified as the ratio between the current flow through the Collector-Emitter and the drive current applied to the Base. In this case, the drive current has to be positive and smaller than the saturation current which would switch the transistor to a permanent on-state with minimum internal resistance. Controlling this drive current and knowing the gain of the transistor, the dissipated power is equal to the product of the Collector-Emitter current and the voltage drop across these terminals which, in turn would be equal to the applied voltage of the power supply in the absence of any other load in the circuit besides the transistor itself. The internal resistance of a transistor is a function of its operating temperature, so a constant base current would not produce a constant dissipated power. For this reason an Operational Amplifier was coupled with the transistor, within the so-called constant current circuit to compensate this behaviour.

The experimental setup shown in Figure 4.4 was used to understand and to optimize all the parameters in order to precisely control the dissipated power by a transistor. The considerable more complex resulting circuit and its explanation may be found in Annex A.1.



a)



b)

Figure 4.4 – a) Electronic control circuit diagram; b) Experimental setup

4.3. CPU package simulation

Using the controlling circuit described in Section 4.2, and in Annex A.1 in more detail, one can now use any N-channel transistor and choose according to the desired maximum power output and dimensions. In order to simulate an extremely demanding CPU a Pentium 4 like configuration was chosen. Recalling Section 4.1, although a 2003 Pentium 4 has an average TDP of only 60 W , it has a single-core architecture which means that the dissipated heat flux through the die is much higher than that in recent multi-core technologies. The selected transistor is a IRFP450 N-channel power MOSFET with a TO-247 package. Relevant characteristics are enclosed in Table 4.1 This transistor has a maximum dissipated power of 190 W and its IHS has a contact area of 172 mm^2 , thus, using this device, a processor can be simulated with a maximum heat flux dissipation of 110.47 W/cm^2 . Maximum junction temperature is 150°C , much higher than in any CPU, to allow a safe margin in the operating temperature of the system. Furthermore, its considerably high on-state internal resistance allows higher voltage for the same current and dissipated power, thus allowing the power supply to work in a more stable condition. Figure 4.5 depicts a visual comparison between an actual die size of a 2005 Intel Pentium 4 CPU and the transistor chosen. CPU die size is 200 mm^2 and the transistor IHS is 172 mm^2 .

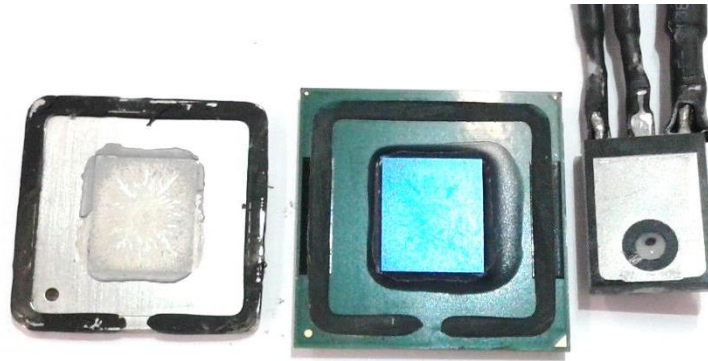


Figure 4.5 – Intel Pentium 4 IHS bottom view (left), processor die top view (centre) and selected transistor bottom view (right).

Table 4.1 – IRF450 N-channel power MOSFET¹

Parameter	Max.	Units
Power Dissipation, P_D	190	W
Junction Temperature, T_j	150	°C
Static On-Resistance, $R_{DS(on)}$	0.40	Ω
Drain Current, I_D	14	A
Gate-to-Source Voltage, V_{GS}	± 30	V

As already mentioned, a processor IHS is made of a copper-nickel alloy which would be difficult to replicate. Hence, to assure the correct material characteristics the actual IHS with $L = 31\text{mm}$, as shown in Figure 4.5 was recovered and is used in the present work. This IHS is also similar to that of a 2011 intel i7, whose typical dimension, according to the datasheet, is $L = 38\text{mm}$.

The developed electronic circuit imposes constant current in the transistor, so the user can control the dissipated power by means of the DC power supply frontal voltage controls. However, the integrated potentiometer does not provide precise control of the resulting dissipated power. This means that, to allow a full and more precise simulation the CPU thermal behaviour, automation of the power supply is also required. Due to the abovementioned reason, a control system has to be developed, comprising a user interface panel.

The HP 6274B DC power supply used allows voltage output remote programming by means of an external resistor connected to the rear panel terminals, disabling the corresponding front panel controls. According to the manufacturer's datasheet, a programming current of $3.33\text{mA} \pm 1\%$ produces

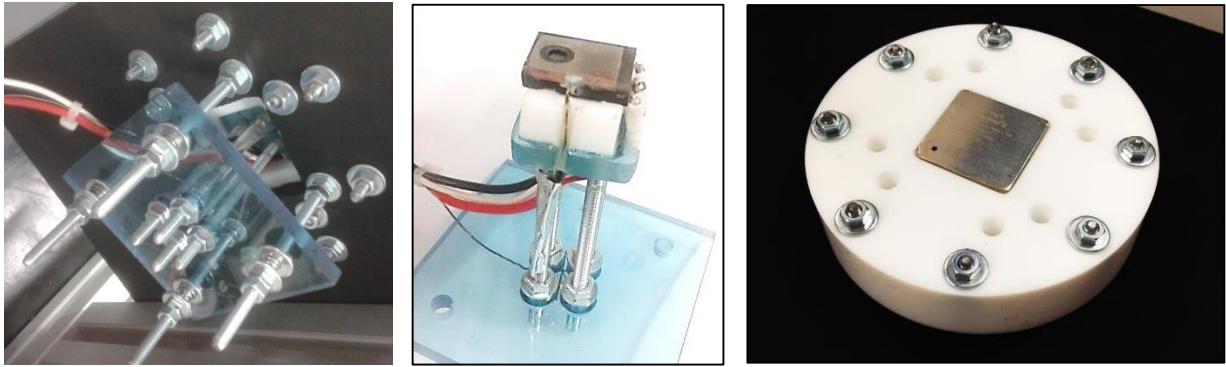
¹ For the sake of coherence the entire document uses bipolar BJT nomenclature. A MOSFET was used and its associated nomenclature in Table 4.1 may differ. The equivalent terminology is the following: Drain – Emitter; Source – Collector; Gate – Base.

a programming coefficient of 300 ohms per volt. Therefore, the solution found consists on a set of four relays controlled by an Arduino micro-controller, allowing to introduce four individually variable resistors in series and each one in parallel with a relay. This results in 2^4 different pre-set values of programming voltage output and equivalent dissipated power in the transistor. Furthermore, a precision multi-turn potentiometer allows the user to either change manually the resulting voltage combination output or to bypass the relay system and fully control the output voltage. The resulting circuit and user interface panel comprise the following features: manual control of voltage output; automatic control via programmed micro-controller; trigger of a pre-programmed sequence via micro-controller programming. The resulting control system is depicted in Figure 4.6. The circuit's diagram, followed by a brief explanation, is available in Annex A.2.



Figure 4.6 – Remote programming controller unit. a) Electronic circuit; b) User interface panel

Finally, the transistor CPU simulated system must be integrated in a functional way with the cooling device to be developed. In this scope, the entire package is surrounded by a PTFE 2 cm thickness block and 10 cm in diameter in order to minimize heat losses to the environment. The only open boundary is the top of the IHS to interact with the cooling system. Four compression springs hold the simulated package together and contact pressure reproducibility is assured due to known spring deflection, in order to reproduce the same contact resistance between the transistor, thermal grease and IHS in every experiment. Concerning junction temperature acquisition, a 0.6 mm hole was drilled in the side base of the transistor up to the mid-section to accommodate a 0.5 mm K-Type insulated probe thermocouple. Insulated probes have lower response time but, reminding that the drilled section of the transistor is in electrical contact with the Emitter, a voltage difference above ground is expected, which would compromise temperature readings. The abovementioned is illustrated in Figure 4.7.



a)

b)

c)

Figure 4.7 – Transistor incorporated within CPU package simulator. a) Bottom assembly view; b) Transistor detail with 0.5mm K-Type insulated probe thermocouple; c) Overview of developed system's top view.

4.4. Validation

In the present work, efforts were conducted in order to accurately replicate a CPU thermal behavior, namely power density, die size and materials. Although the IHS has the exact same material and dimensions, and the simulated die dimensions are in accordance to an actual CPU, the thermal response of this CPU simulator must be validated under steady-state and transient power loads.

Recalling the attempt made to use a real processor by welding the power pins directly to a DC power supply, a maximum of 20 W of dissipated thermal power could be obtained in that configuration. Although the developed simulated system could dissipate up to 190 W, the thermal response of the simulator was validated for 20 W, by comparison with the behavior of the real CPU, and conclusions were extrapolated to the entire power range.

The expected temperature profile on the top of the IHS for both the actual CPU and the simulated one is expected to be non-homogeneous with a continuous distribution along the surface. The location of the maximum temperature is not expected to necessarily occur at the geometric center of the IHS, being the temperature distribution also a key parameter to validate the simulated system, together with the maximum temperature measured on the surface. A surface thermocouple cannot acquire a temperature field. Furthermore, the surface thermocouple requires a high conductivity thermal compound in order to minimize the contact resistance between the thermocouple and the target, which would not be replicated exactly for every experiment. For the abovementioned reasons, high speed Infrared Thermography was used to measure the temperature distribution in the real CPU and in the simulator.

4.4.1. Infrared Thermography experimental setup

An enlightening scheme of the developed facility used to validate the thermal behavior of the CPU simulator is depicted in Figure 4.8.

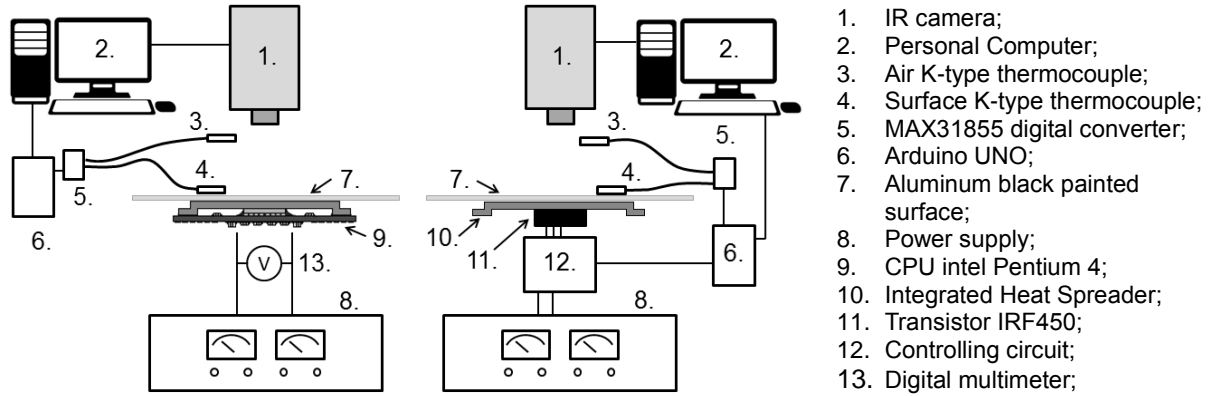


Figure 4.8 – Experimental setup

The Infrared Thermographic camera used is an ONCA 4969 from *Xenics*. Its main characteristics are presented in Table 4.2.

Table 4.2 - *Xenics* ONCA 4969 IR camera

Camera characteristics	Optical system	Image characteristics
Sensor: InSb (MWIR)	Focal lens: 13mm	Video rate: 60Hz
Spectral sensibility 3.5 to 5µm	Optics material: germanium	Max. framerate: 3000fps
Resolution: 320x256 pixel		Minimum Region of interest:
Pixel dimension. 30x30µm		15x5 pixels
Refrigeration: Stirling engine		Exposition time > 1µs
Thermal sensibility < 17 mk		
Pixel operability > 99.5%		

Temperature measurements using infrared thermography consists on the capture of incident radiation through a germanium focal lens transparent to IR radiation. This radiation is then collected by the incorporated photo-detector, thus converting the intensity of the incident radiation to a 2D matrix of the temperature distribution of the focal plane. However, not all the radiation acquired by the camera is emitted by the target object due to participating media and reflection from the surroundings.

The camera evaluate the target object temperature by means of the following equation:

$$T_{obj} = \sqrt[4]{\frac{W_{tot} - (1 - \varepsilon_{obj}) \cdot \tau_{atm} \cdot \sigma \cdot (T_{refl})^4 - (1 - \tau_{atm}) \cdot \sigma \cdot (T_{atm})^4}{\varepsilon_{obj} \cdot \tau_{atm} \cdot \sigma}} \quad (4.1)$$

In order to solve Equation 4.1, the following parameters must be supplied: the emissivity of the object (ε_{obj}) related to the material or coating characteristics of the object; the surroundings equivalent reflected temperature (T_{refl}), the transmittance of the atmosphere (τ_{atm}) correlated to the distance of the object to the focal lens, and the temperature of the atmosphere (T_{atm}).

An actual Intel Pentium 4 processor was directly connected to a DC power supply according to the methodology introduced in section 4.1. The simulated CPU package was controlled with the circuit developed as explained in section 4.3. Both devices are coupled to a 2mm thickness aluminium plate using a thin thermal compound layer in the interface, to reduce contact resistance. This surface is smooth on both sides and has the same dimensions as the interface surface that will be used later to couple the cooling device to the CPU simulator. Both surfaces are black mate painted with $\varepsilon_{obj} = 0.95$.

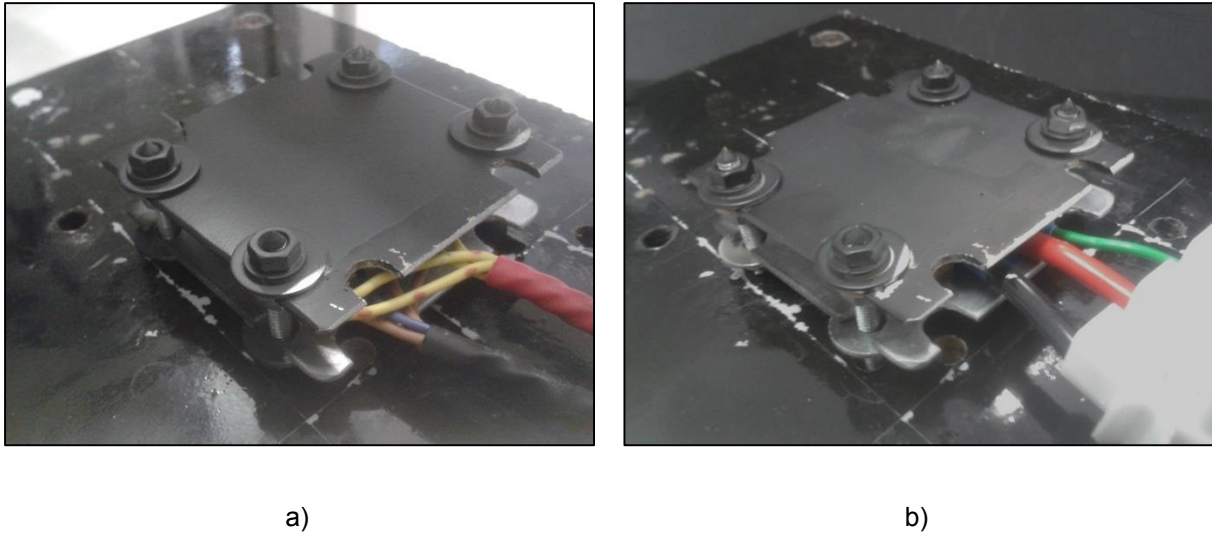


Figure 4.9 – Experimental assembly. a) Intel Pentium 4; b) CPU simulator

Two K-Type thermocouples are used and acquired with a MAX31855 cold-junction compensated thermocouple-to-digital converter connected to an Arduino UNO board. This converter resolves temperatures to 0.25°C with $\pm 2^\circ\text{C}$ accuracy. Surface temperature is acquired only for monitoring purposes; atmosphere temperature is acquired and introduced into the camera software along with the focal distance in order to account for the atmosphere transmittance.

The surroundings reflected temperature (T_{refl}) measurement requires a recommended procedure as follows: in order to account for the reflection from air, this theoretical temperature is measured by placing a reflective object at the same focal distance and its recorded temperature is inserted into the software. At last, in order to account for the reflection of the infrared image of the camera's own lens, known as *Dionisio* effect, an offset calibration is required. A plain object is placed in front of the camera and calibration for the reflection is performed using the integrated algorithm of the camera's software.

4.4.2. Results and conclusions

Figure 4.10 depicts a qualitative comparison between the real CPU (Figure 4.10a) and the simulator transistor (Figure 4.10b) surface temperature under constant load. On top of both images a surface K-Type thermocouple is visible. Dashed lines indicate pixel region to be acquired.

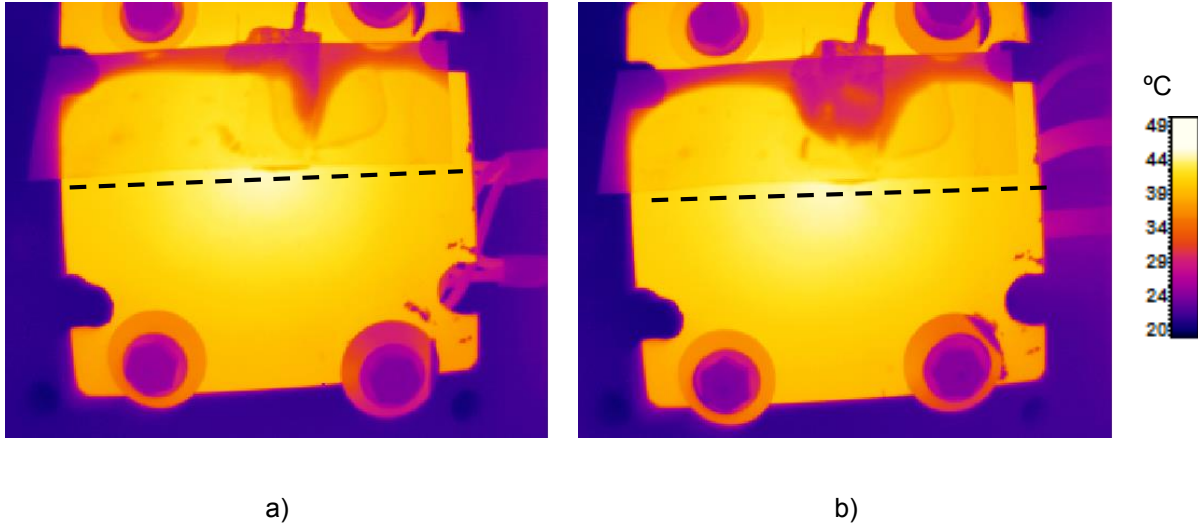


Figure 4.10 – IR image of CPU and transistor assembly at $P_D=15W$. a) Intel Pentium 4; b) CPU simulator. Dashed lines indicate acquisition region

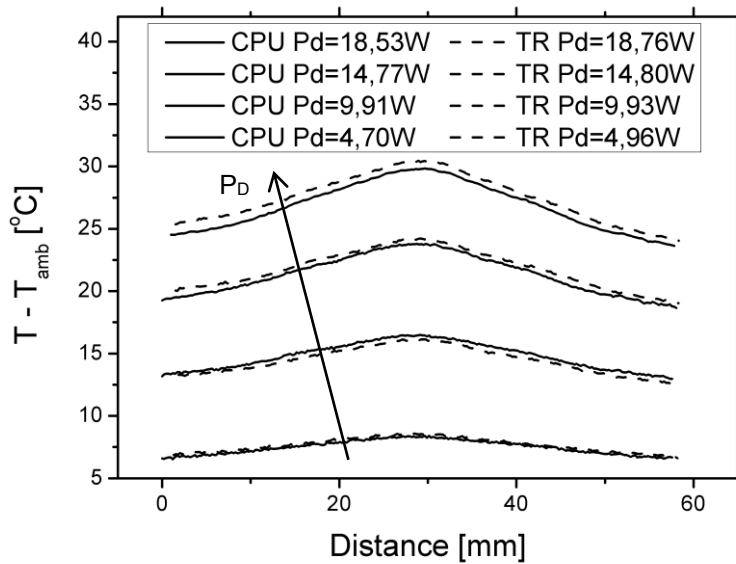


Figure 4.11 – Temperature distribution in steady-state conditions.

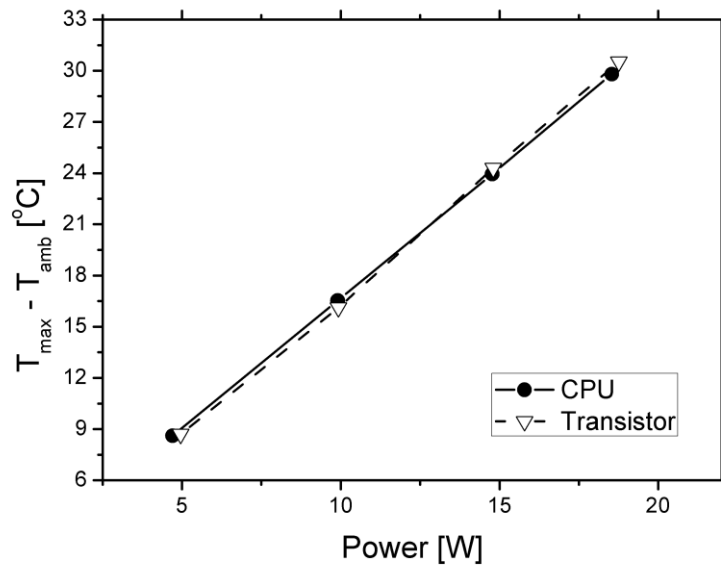


Figure 4.12 – Maximum temperature at steady-state conditions.

The system developed in Section 4.2 to control of the dissipated power of the transistor is very precise. On the other hand, no control or acquisition system for the processor power dissipation has been developed. The dissipated power P_D , is controlled directly with the main controls of the power supply and computed later using a digital multimeter. Consequently the dissipated power in the real CPU and in the simulator is not exactly the same, which results in the temperature difference between both configurations, depicted in Figure 4.11. Nevertheless a qualitative approach suggests that the distribution profile of the temperature is comparable for both configurations, with similar temperature gradient across the mid-section.

Also, due to time lag between experiments and consequent change in ambient temperature, all plots account for the temperature difference, using as a reference the ambient temperature registered at the beginning of each test. This is done under the assumption that for the ambient temperature change between experiments the natural convection heat transfer coefficient does not change significantly, thus this methodology is considered suitable for this purpose.

Figure 4.12 illustrates the maximum recorded temperature for each dissipated power for both real CPU and simulator. One can safely conclude that within instrumentation uncertainty the transistor coupled to an IHS replicates steady-state thermal behavior of a real CPU.

It is still necessary to validate the system under transient conditions. For this purpose, time resolved acquisition (300fps) of the temperature field was acquired under a sudden power step and maximum temperature, in the aforementioned region of interest, for each frame is considered. Dissipated power was computed for both configurations. Results are depicted in Figure 4.13.

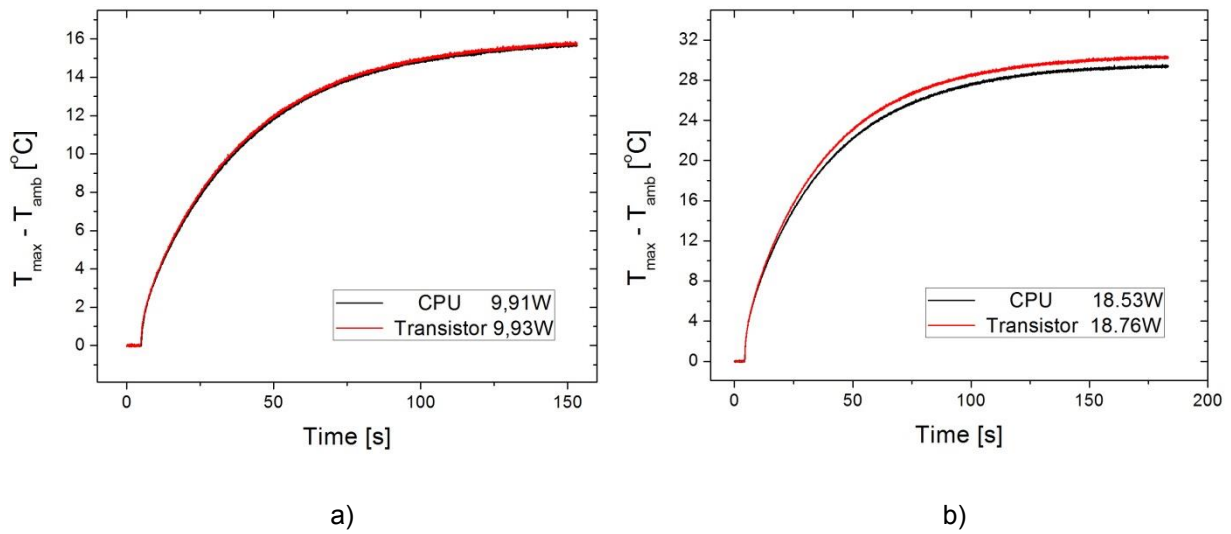


Figure 4.13 – CPU and Transistor assembly under transient power step. a) $P_D \cong 10W$; b) $P_D \cong 20W$

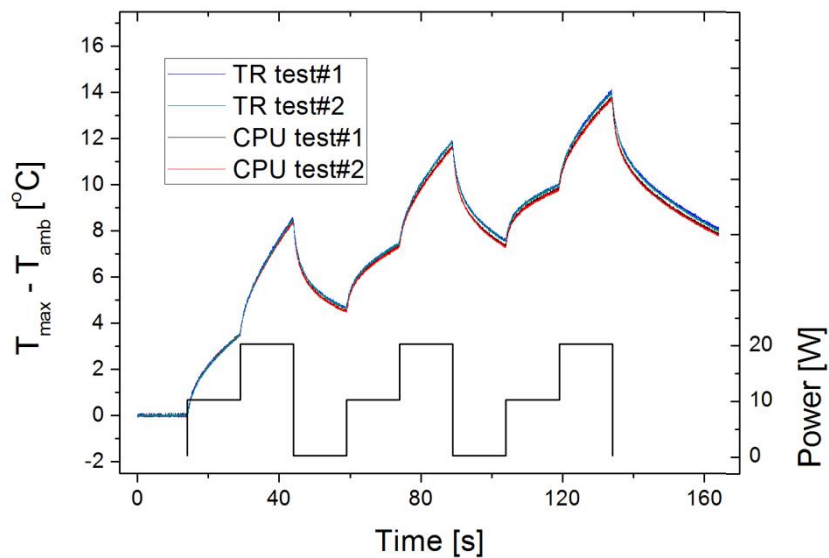


Figure 4.14 – CPU and Transistor temperature evolution under cyclic power steps.

Once again, paying attention to the figures' labels some discrepancies in the dissipated power are evident (Figure 4.13, b), with obvious consequent difference in the settled temperature. However, the thermal behaviour of the transistor is still very similar to that of the CPU for the tested conditions.

Finally, Figure 4.14 shows the transient temperature evolution for both configurations, under cyclic power steps. Maximum temperature for each frame along time shows no evidence of accumulated error due to a possible difference in both systems' capacitance.

Despite the limitations of this comparative study, as discussed in the previous paragraphs, one may argue that the extrapolation of these results to the entire power capacity range of the transistor (190W) is valid, thus concluding that the CPU simulator can fairly reproduce a CPU thermal behaviour.

5. Design and development of the thermosyphon experimental facility

To achieve the objectives proposed in Chapter 1, an experimental setup was developed from scratch, comprising an adequate test section as well as all the auxiliary components required such as auxiliary equipment, acquisition and control systems. A simple system was first assembled to work as a proof-of-concept and to test the experimental methodology and control and acquisition systems to be implemented (section 5.1). From this first attempt, a final configuration was assembled, as described in section 5.2.

5.1. Proof of concept prototype

As already mentioned in Chapter 2 pool boiling is well known to be suitable and extremely attractive in the context of IC cooling, as supported by several studies reported in the literature. Nevertheless, the development of a functional system, for the working conditions tested in the present work, requires an experimental validation of entire system comprised by the loop thermosyphon, the simulated CPU heat source and the corresponding control system.

5.1.1. Working fluid

The performance of a cooling device based on two-phase heat transfer strongly depends on the properties of the working fluid, which influence the condensation and boiling heat transfer coefficients, as well as the critical heat flux. Apart from the properties related to the heat transfer processes, other requirements should be addressed, such as global environment impact (zero ozone depletion potential). The fluid should also not be hazardous to the equipment (not corrosive, explosive or flammable) nor should be toxic. In addition, stability of the working fluid under the environmental working conditions of the device, cost and availability, among other factors should also be weighted. Considering the present context of electronic cooling application, an inert and dielectric fluid is recommended in order to meet the requirements of safety and reliability. However, compared to water under similar working conditions, boiling heat transfer rates on dielectric fluids are low owing to their low thermal conductivity and latent heat of vaporization. For instance, considering 3M Novec HFE-7000, used in the present study, its thermal conductivity is 0.075 W/m.K , which is only 12.9% of the thermal conductivity of water (0.58 W/m.K) at 25°C . Also, its latent heat of vaporization at the boiling point is 142 kJ/kg , corresponding to 6.3% of water latent heat. As a result, the major heat transfer mechanisms, including thin-film evaporation, convective boiling and nucleate boiling, are limited by their poor thermal properties. An effective management of these constrains led to explore the use of micro-structured surfaces to enhance nucleate boiling and convective heat transfer.

Another relevant characteristic of the working fluid is the solubility of air in the HFE-7000, which is approximately 35% in volume of air in the fluid. This property is relevant given that the air dissolved

affects the onset of boiling, may induce deterioration of the heat transfer coefficients and contributes to the presence of non-condensable gases inside the loop. Therefore, a degassing procedure was carried out at the beginning of each experiment.

Novec HFE-7000 is a hydrofluoroether manufactured by 3M. Main thermo-physical properties are presented in Table 5.1.

Table 5.1 - 3M Novec HFE-7000 properties at 25°C, 1atm.

Parameter.	3M Novec HFE-7000	Units.
Chemical formula	C ₃ F ₇ OCH ₃	-
Saturation temperature, T_{sat}	34	°C
Liquid density, ρ_l	1386.2	Kg/m ³
Vapour density, ρ_v	8.22	Kg/m ³
Liquid dynamic viscosity, μ_l	4.31x10 ⁻⁴	N·s/m
Heat capacity, C_{pl}	1327.93	J/kg·K
Thermal conductivity, k_l	0.075	W/m·K
Latent heat of vaporization, h_{fg}	132.16	kJ/kg
Liquid surface tension, σ_{lv}	12.4x10 ⁻³	(N/m)

The pressure-temperature relation along the saturation curve is given by the manufacturer.

$$\ln(p \cdot 10^6 [MPa]) = -\frac{3548.6}{T[K]} + 22.978 \quad (5.1)$$

where $243 < T[K] < T_c$ and $T_c = 437.7K \pm 0.1$. The liquid density, heat capacity, kinematic viscosity and thermal conductivity as function of temperature are as following:

$$\rho_l [kg \cdot m^{-3}] = 1472.6 - 2.880 t[°C]; \quad -120 < t[°C] < 35 \quad (5.2)$$

$$c_{p,l} [J \cdot kg^{-1} \cdot K^{-1}] = 1223.2 + 3.0803 t[°C]; \quad -120 < t[°C] < 40 \quad (5.3)$$

$$\nu_l [m^2 \cdot s^{-1}] = 90.9555 T[K]^{-3.43316}; \quad 233 < T[K] < 304 \quad (5.4)$$

$$\kappa_l [W \cdot m^{-1} \cdot K^{-1}] = 0.0798 - 1.96 \cdot 10^{-4} t[°C] \quad (5.5)$$

Several contacts with 3M were successfully carried on in order to minimize possible delays in the experimental facility development caused by material incompatibilities. Known incompatibility issues are plasticizers and additives added in the production of elastomers. Polymeric materials, however,

are the most suitable construction materials for the experimental facility, as they have a reduced cost and can be easily machined. The primary concern is the solubility of the plasticizer in the fluid which can be extracted from the polymer matrix, affecting both. Hydrofluoroethers' molecules contain not only fluorine, but also hydrogen, and because "like dissolves like" the working fluid is capable of easily dissolve common hydrocarbon plasticizers. Extraction of plasticizers from an elastomer can cause it to harden, crack or shrink. 3M recommended the following compatibility chart, concerning polymeric materials:

Table 5.2 - Polymeric materials compatibility chart with 3M Novec HFE fluids.

Compatible		Non compatible	
Polyethylene	Rulon™	Nitrile	Polysulfide
Polypropylene	PTFE(Teflon™)	Silicone	Polyacrylate
ABS	Polysulfone	Butyl	Polyurethane
Nylon	PEEK	Fluorocarbon	Styrene
PVC	Thermoplastics	Fluorosilicone	Butadiene
Polycarbonate	Acrylic(Plexiglas™)	Natural Rubber	Ethylene
		Chloroprene	EP or EPDM

However, due to high variability in the composition of the commercially available materials, the abovementioned compatibility chart can only be used for a preliminary selection of the materials. Hence, for every new material, a simple experiment should be performed to test the compatibility of the material with the working fluid. In the present study, samples of the materials were submerged into a HFE-7000 bath for one week, being the fluid replaced several times to avoid fluid saturation. Results shown that Viton O-rings were the only seal material that did not become brittle after one week of exposure. The other seal materials tested were NBR and EPDM. A Teflon-based anaerobic adhesive and Araldite epoxy were also subjected to testing, showing good results. Hence, the sealing was performed with Viton O-rings and a Teflon-based anaerobic adhesive.

5.1.2. Experimental prototype, instrumentation and acquisition

As already mentioned in chapter 2 Maciel [86] performed in 2014 - in this same research group - a pool boiling experiment on direct immersion of a working Pentium 4 CPU. The author was not interested in the cooling system, as the work mainly concerned the parametric characterization of the electronic actuation of a Peltier cell. However, the author did in fact use a pool boiling evaporator with HFE-7000 as working fluid. Despite the fact that the evaporator was extremely large for the expected dimensions of a convectional heatsink replacement, due to the documented effectiveness of this evaporator's dimensions, it was used in this present work as a starting point.

In order to condense the vapour, a water radiator intended for a CPU water-cooling system was used. The available models at the market restricted the choice of the condenser arrangement or configuration. A satisfactory solution was provided by a common flat tube finned heat exchanger, with

bras tubes and copper fins. Due to the fact that this particular heat exchanger is intended to work with single phase fluids, it contains two passages thus both the fluid connections are on the same side. Given that, for the thermosyphon developed in this work the vapour reaches the condenser due to impulsion and the condensed liquid film leaves due to gravity, there is no easy way to implement the abovementioned radiator as a gravity-assisted condenser without flooded areas. Nevertheless this condenser was used, as a starting point, powered by a 12V DC computer fan.

At this stage, piping was chosen solely based on assembly feasibility. Given the G1/4" threads in the condenser, the entire vapour line was built with bras nickel-plated pipe with standard 8mm inner diameter. Liquid line is a flexible 4mm inner diameter Nylon transparent tubing to allow flow visualization and easy assembly.

The evaporator bottom boundary is open to allow changing the interface aluminum surface used to couple with the simulated CPU heat source.

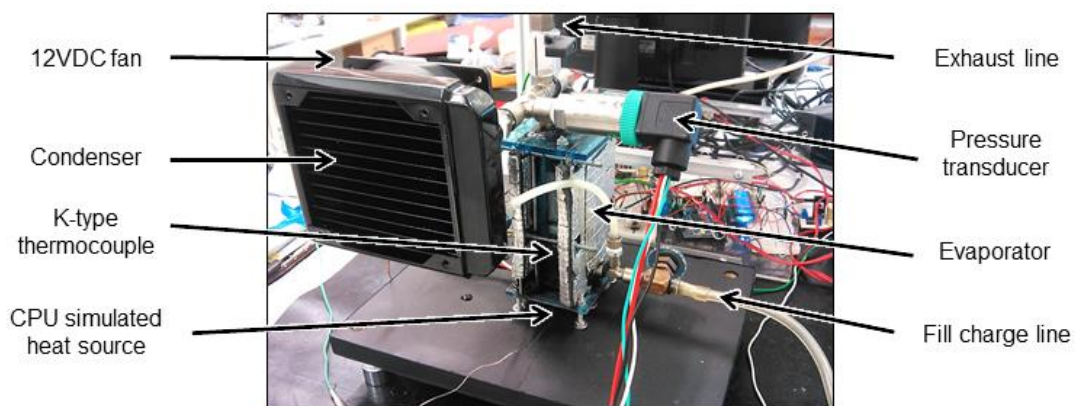


Figure 5.1 – Proof-of-concept prototype

A GEFTRAN -1..2bar gauge pressure transducer voltage amplified with $\pm 0.5\%$ FSO accuracy is flush-mounted into the vapour line, connecting the evaporator to the condenser inlet. This transducer is already amplified and voltage-output is acquired by the Arduino Due board integrated 12-bit ADC (Analog to Digital Converter). Calibration was conducted by the manufactures (3.33mV/mbar) which is valid for two years and resolution after acquisition is 0.73 mbar. Readings are compensated by a OMEGA DYNE Inc, with 0.08% FSO accuracy (0..2bar) absolute pressure sensor already available in the laboratory facility.

Three thermocouples by OMEGA are used, to measure: 1) the junction temperature is measured inside the transistor as reported in sub-section 4.4; 2) the saturation temperature of the liquid (using a 0.5mm insulated probe K-type thermocouple placed inside the evaporator) and 3) the ambient air temperature (using an exposed probe K-type thermocouple placed at the intel of the condenser's fan). Acquisition is performed by individual connection to a MAX31855 cold-junction compensated thermocouple-to-digital converter SPI (Serial Peripheral Interface) connected to the abovementioned micro-controller. This converter resolves temperatures to 0.25°C with $\pm 2^\circ\text{C}$ accuracy.

The imposed heat generation by the transistor is controlled with the aforementioned electronic circuit developed in Chapter 4 and Annex A.1. Dissipated power is obtained by the product of voltage drop

across the transistor terminals and the current flow. Voltage drop is acquired by a precision voltage divider and directly connected to the micro-controller ADC. Resolution after acquisition is 103.3mV. Current is acquired by 4 parallel Burdon precision high power resistors of 2.0 Ohms \pm 1% cooled by a 12VDC fan in order to maintain the temperature within the valid region of accuracy reported in the datasheet. Resolution after acquisition is 20.39mA.

The 12VDC condenser fan is electronically controlled by a home-made circuit. Detailed circuit diagram and explanation is available in Annex A.3. This circuit also allows controlling the rotational speed of the fan, by means of feedback acquisition of an integrated pulse counter. Analog control is performed using the 3.33V 8-bit DAC (Digital to Analog Converter) of the Arduino DUE board and amplified afterwards. The rotational speed of the fan is acquired by the integrated digital pulse counter of the micro-controller.

National Instruments LabView was used for data pre-processing, acquisition and real-time graphical representation. The Arduino board communicates with LabView via VISA communication protocol at 10Hz. A PID (Proportional-Integral-Derivative) controller was developed in LabView environment, to control the fan rotational speed at constant rpm, or the pressure inside the system, by actuating on the air-side forced-convection heat transfer performance. Due to the complex transfer function correlating the interior equilibrium pressure with the rotational speed of the condenser's fan, the PID was in-house tuned according to the heuristic Ziegler-Nichols method [87] with Gain Scheduling method due to the non-linear behaviour of the supplied voltage and rotational speed of the fan.

5.1.3. Results and conclusions

The assembly of this "*prototype*" was not intended to formally or quantitatively address the cooling performance of the system devised in this work, but to test the feasibility of its implementation and understand its overall behavior. Also, several tests under different conditions were conducted in order to determine the proper methodology to tackle when designing the final facility.

Preliminary tests performed with different micro-structured surfaces confirmed the reproducibility of the results for the same surface, after it accommodated. However, these preliminary results also showed that the procedure used to fix the surfaces must be tuned in the final facility, to assure reproducibility of the boundary conditions. Hence, 3 major problems were identified: 1) the amount of silicone used to seal the contact between the evaporator bottom wall and the surface was not easily controlled and due to silicone spreading, the same contact area repeatability was not guaranteed; 2) the use of bolts and nuts to fix the surface induces non homogeneous tensions in the surface, thus flat integrity in the contact with the simulated heat source IHS was not assured; 3) the aforementioned condenser positioning resulted in partially flooded areas which in turn deteriorate heat transfer, thus the equilibrium pressure attained is higher and the PID tuning extremely difficult.

5.2. Final experimental facility design

5.2.1. Evaporator design

Given the importance of the evaporator to the overall thermal performance of the cooler, much attention was given to the design of this element. The evaporator consists on a pool boiling reservoir which is placed on top of the CPU simulated heat source, using thermal interface grease. As already discussed, this element has to allow interchangeability of different surfaces, to infer on the effect of surface micro-structuring, while maintaining the entire system hermitically sealed. The size of the evaporator will also be subjected to a parametric study, so the design of the cooling system must also take into account an easy assembling and disassembling of several evaporators with different sizes. Also, visualization of the phenomena occurring inside the evaporator is expected to provide important information to describe the overall performance of the devised system. Hence, a transparent material has to be used to allow optical access. All the materials used in the design process must be compatible with the working fluid and hold good mechanical properties at temperatures as high as 80°C, the maximum working temperature of the system. Concerning mechanic considerations, the evaporator has to allow a vapour outlet and a liquid return inlet, both comprising a pressure tap for differential pressure measurements and seats for thermocouples. A pressure transducer has to be flush-mounted on the evaporator wall as well as a thermocouple in order to infer on the liquid saturation condition. Also, the evaporator will be subjected to a change in the orientation, thus the location of the aforementioned instrumentation and connections must be anticipated to consider this possibility.

According to 3M, the critical heat flux condition is achieved at 18 W/cm^2 from a 0.5 mm diameter platinum wire immersed in a quiescent pool of saturated liquid (HFE-7000) at atmospheric pressure. According to the expression proposed by Zuber [52] (Equation 3.3) the critical heat flux is attained at 20.3 W/cm^2 . Using the 3M data and preliminarily setting the thermal design point of the system to 200 W, a plain surface in contact with the working fluid should have the minimum surface area of 11.1 cm^2 . Due to structural stiffness and ease of manufacturing, a cylindrical based evaporator was selected, thus the minimum diameter is 37.6 mm. In order to completely cover the entire IHS of a modern Intel i7 with diagonal size of 41.4 mm, a 42 mm inner diameter acrylic tube was selected. The cylindrical evaporator was machined with two grooves for Viton O-rings, a liquid return line and a slot to accommodate the thermocouple measuring the liquid saturation temperature. The cover comprises the pressure transducer and the vapour outlet.

The diameter of the inlet and outlet connections were selected according to the maximum allowed pressure losses in the lines calculated with the Darcy–Weisbach equation [88]. Assuming that the friction losses occurring in a maximum liquid line length of 200 mm should be lower than the positive pressure head of liquid column in the minimum condenser height, relative to the inlet of the condenser, (30 mm), the positive pressure head of 4 mbar should be able to drive 1.3 ml/s across a 200 mm line. This results in a minimum tube inner diameter of 2.3 mm. Thus, a 4 mm inner diameter PVC tube was

used for the liquid line. A 9 mm inner diameter PVC tube was used for vapour line due to feasibility constrains. The final design of the evaporator is schematically represented in Figure 5.2

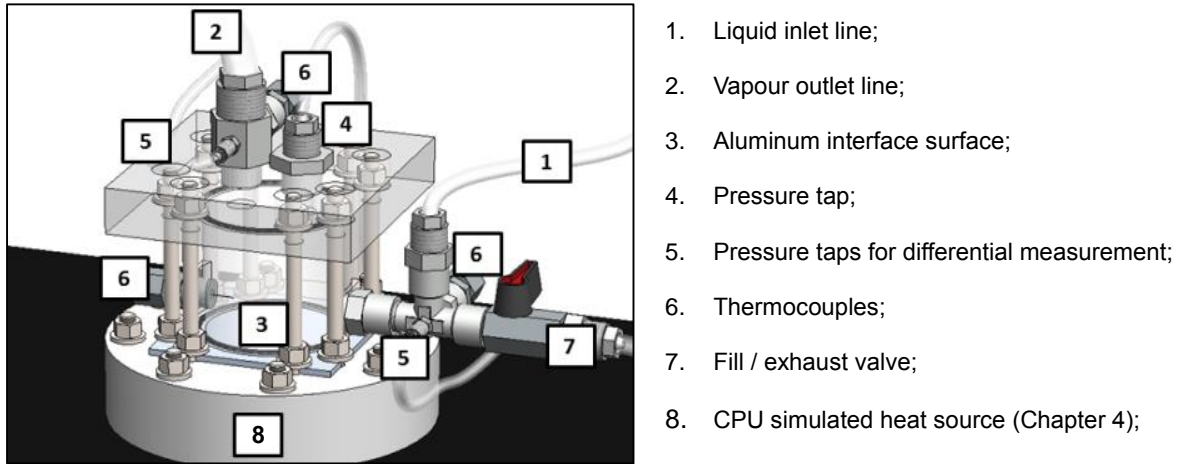


Figure 5.2 – CAD model of the evaporator.

5.2.2. Condenser design

In order to close the loop a feasible solution to condensate the vapour flow rate must be provided. Due to the poor thermodynamic properties of the dielectric fluid, the inner side area has to be extended, as well as the air-side area due to the relatively small forced-convection heat transfer coefficient. Considering manufacturing feasibility a tube-and-fin heat exchanger was considered. The condenser must be placed above the evaporator so the vapour can rise due to buoyancy and the condensed liquid film forming on the inner side walls of the condenser tubes is drained due to gravity forces and expected to fall back to the evaporator by the liquid return line. To avoid flooded areas, the condenser should comprise only one passage, with all the tubes in parallel. Thus, the inlet and outlet should be positioned in opposite sides and the tubes must be straight. The frontal area of the condenser should be $120\text{mm} \times 120\text{mm}$ in order to couple a standard 12VDC fan. Concerning instrumentation, the condenser shall have a plenum chamber at the inlet and outlet where a pressure tap for differential pressure measurements as well as two thermocouples are placed. The inlet should allow connecting one or two tubes (regular condenser arrangement or reflux arrangement) and the outlet should allow a single tube connection.

Concerning the degassing procedure required, the highest part of the condenser should also comprise a valve through which the vacuum pump is connected.

Although the CPU simulated heat source could in theory dissipate up to 190 W, the controlling circuit was designed to provide only up to 150 W of electrical power. Thus, the condenser should be able to dissipate this heat transfer rate. The design point is set to 200 W for safety reasons. Also, due to lack of information on the thermochemical properties of the fluid as function of pressure, the design process was conducted assuming atmospheric pressure, although the working pressure inside the loop is expected to be lower.

The LMTD (Log-Mean Temperature Difference) method was used following the methodology presented in [89]. Under the assumption that the vapour enters the condenser at saturation temperature and that no sub-cooling occurs and neglecting the inner pressure drop, the vapor temperature is assumed to be constant and equal to the saturation temperature at atmospheric pressure across the entire tube length, as illustrated in Figure 5.3.

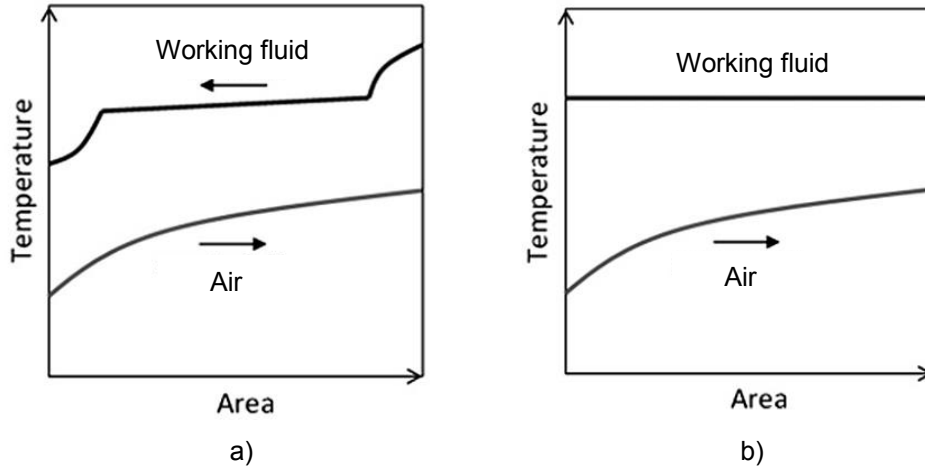


Figure 5.3 – a) Actual fluid temperature distribution in a condensation process. b) Idealized model. Adapted from [89]

The unmixed crossflow configuration with the constant temperature assumption, as abovementioned, results in a correction factor of $F = 1.0$ according to [89]. The iterative design procedure consists on solving equation 5.6 until convergence is achieved.

$$Q = AU F \Delta T_{LM} \quad (5.6)$$

Here, Q is the heat transfer rate, A is the outer heat transfer surface area, U is the overall heat transfer coefficient, F is correction factor used for every arrangement other than counter-flow. The log-mean temperature difference is calculated as follows:

$$\Delta T_{LM} = \frac{(T_{ext,o} - T_{ext,i})}{\ln\left(\frac{T_c - T_{ext,i}}{T_c - T_{ext,o}}\right)} \quad (5.7)$$

in which T_c is the coolant temperature, i.e. the saturation temperature of the working fluid. The air-side outlet temperature is determined based on an energy balance to the inlet and outlet of the condenser and this result must converge to the condenser overall heat transfer rate. Air properties can be assumed to change according to the ideal gas law and, due to small change in air temperature, specific heat capacity can be assumed to be constant, being evaluated at the mean air temperature.

The AU factor is based on the outer heat transfer phenomena due to the fact that the design process is primarily focused on the exterior geometry. A is the outer heat transfer area and U_o is the overall heat transfer coefficient, based on the exterior area for a finned-tube heat exchanger, defined as:

$$U_o = \frac{1}{\frac{A_o}{h_i A_i} + \frac{A_o r_i \ln(r_o/r_i)}{A_i k_w} + \frac{A_o}{[h(A_f \eta_f + A_b)]_o}} \quad (5.8)$$

where h_i is the interior heat transfer coefficient, r_o and r_i are the outer and interior tube radius, k_w is the thermal conductivity of the tube wall material. h_o is the exterior heat transfer coefficient, A_f the finned surface area η_f the fin efficiency and A_b the tube base area. The fin efficiency η_f is calculated by using the approximation method as described by Schmidt [90].

The inner side convective condensation heat transfer coefficient is calculated using equation 3.4, correlation proposed by Chato [76], and already introduced in Chapter 3. In fact, for a horizontally oriented tube, the flow regime is stratified with small vapour velocity and low interfacial forces, since the maximum Reynolds vapour number, for the commercially available inner tube diameters is 450 much lower than 2000, the critical value from which stratified wavy flow begins [76].

The Chato's parameter F was calculated according to equation 3.6 considering the average 2ϕ angle equal to 120° as originally proposed by the author [76]. This is a safe approach, since other authors suggest different correction values that could led to higher heat transfer coefficients [78, 79]. The modified latent heat was calculated according to equation 3.5 and the wall temperature was iteratively assumed in the design process.

The outer heat transfer coefficient was derived from j-Colburn data, published for several geometries. This was an iterative procedure severely constrained by the manufacturing capabilities of the suppliers and the requirements of this application. The best possible solution achieved comprised herringbone fins with two rows of five staggered tubes, following the dimensions made available by the Portuguese company Centauro. The geometrical parameters used for this design process are confidential data provided by Centauro and therefore are not disclosed here. The parameters are within the validity region of the semi-empirical correlation proposed by Wang [91] for herringbone patterned fins, as follows:

$$j = 0.324 Re_{dc}^{c_1} \left(\frac{p_f}{X_l}\right)^{c_2} (\tan\theta)^{c_3} \left(\frac{X_l}{X_t}\right)^{c_4} N_r^{0.428} \quad (5.9a)$$

where

$$c_1 = -0.229 + 0.115 \left(\frac{p_f}{D_c}\right)^{0.6} \left(\frac{X_l}{D_h}\right)^{0.54} N_r^{-0.284} \ln(0.5 \tan\theta) \quad (5.9b)$$

$$c_2 = -0.251 + \frac{0.232 N_r^{1.37}}{\ln(Re_{dc}) - 2.303} \quad (5.9c)$$

$$c_3 = -0.439 \left(\frac{p_f}{D_h}\right)^{0.09} \left(\frac{X_l}{X_t}\right)^{-1.75} N_r^{-0.93} \quad (5.9d)$$

$$c_4 = 0.502 [\ln(Re_{dc}) - 2.54] \quad (5.9e)$$

The regression analysis used by Wang to devise this correlation used 61 different geometries and approximately 570 data points. The author claims that the correlation can predict 91% of the experimental data within $\pm 15\%$. The nomenclature used above can be better understood by inspection of Figure 5.4.

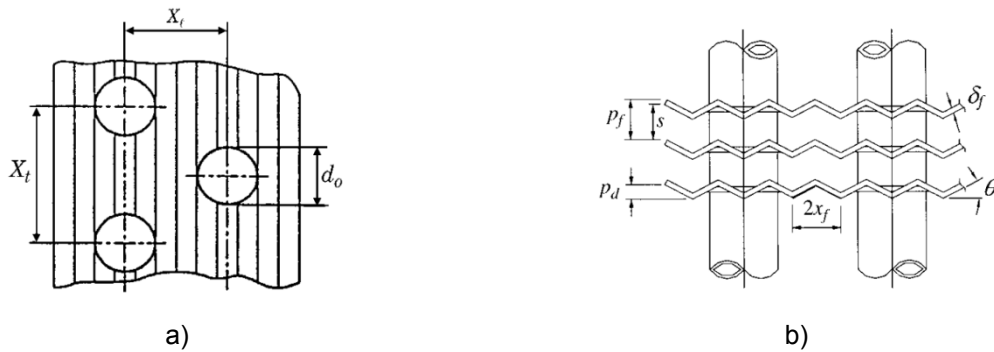


Figure 5.4 – Corrugated herringbone fin on a tube array. a) front view; b) side view; Adopted from [89].

The resulting geometry designed with the abovementioned methodology and depicted geometry consists of two rows of five staggered tubes 35 fins with $120\text{mm} \times 120\text{mm}$ of frontal area and 38 mm depth. Additional relevant empirical information can be provided. So, the free-flow area/frontal area is $\sigma = 0.584$, the heat transfer area/total volume is $\alpha = 537\text{m}^2/\text{m}^3$; This configuration allows to dissipate 253 W of heat transfer rate. It is considered a safe approach and a requirement in this design process to oversize the condenser capacity. The simulated heat source dissipates up to 150 W and the thermal design point of the condenser was chosen to be 200 W as a safety margin. However, a single row of tubes could dissipate only 145 W which is not enough, and a more compact geometry was not available.

Although the abovementioned condenser solution had a suitable heat transfer capacity and dimensions according to the requirements, a more compact geometry could significantly reduce the condenser size and improve the applicability of the cooling system to a PC desktop. In this context, another Portuguese company Sorradiadores was also available for custom made manufacturing. The only available geometry consists on radiator-like geometry comprising flat tubes with plain serpentine fins. Although promising due to high typical compactness, very few experimental studies or correlations were found in the literature. In fact, this is a common geometry but it usually comprises louvered fins. Furthermore, the only published study found in the literature, with plain serpentine fins was performed by Park and Jacobi [92], but the reported validity region of the j correlation is far from the actual geometrical parameters of the geometry proposed in the present work. In this context, a numerical CFD (Computational Fluid Dynamics) simulation was carried out in order to infer on the heat transfer performance of the abovementioned geometry. This simulation was also performed to check if the designed condenser could be more compact.

Numerical simulation

The simulation was performed using a commercially available CFD software (COMSOL Multiphysics 4.3b). As a first approach, the geometry obtained with the aforementioned Wang's empirical correlation was modelled and numerically validated inferring on the suitability of the modelling conditions used to replicate the air-side heat transfer performance. Later, the resulting settings were used to simulate the new geometry in order to conclude on the number of tube rows actually required to condensate the proper mass flow rate of vapour, since the frontal area is a fixed parameter.

COMSOL Multiphysics uses the Finite Element Method (FEM) to approximate solutions to boundary value problems. In each finite element the PDE's (partial differential equation) are locally approximated. The element equations are then combined into a global system of equations, over the entire domain, with an approach based on variational theory of calculus, in which an error function is minimized to yield the best approximation to the solution. This means that all spatial derivatives are removed, approximating the PDE's, over each element, as algebraic equations for this steady-state case. The resulting system of equations is then solved by numerical linear algebra. Non-linear equations such as Navier-Stokes have to be linearized in order to be solved. The local equations are combined into a global system of equations to approximate the solution on the entire domain. The resulting FE approximation, to the solution, is built out of linear combinations of basis functions, where each function is connected to a node point of the elemental mesh. These basis functions are polynomials where the order can be increased to improve accuracy, but this also increases the computational complexity of the problem. There are many advantages with the FEM, since complex geometries can be described with non-uniform meshes. The downside is that it is mathematically complex, when compared to other methods such as the Finite Volume Method (FVM), another common numerical method often used for fluid flow problems.

The flow over the fins is assumed to be laminar and steady-state. The equations representing the conservation of mass, momentum and energy for the three dimensional model are as follows:

$$u \frac{\partial u}{\partial x} + v \frac{\partial u}{\partial y} + w \frac{\partial u}{\partial z} = 0 \quad (5.10)$$

$$u \frac{\partial u}{\partial x} + v \frac{\partial u}{\partial y} + w \frac{\partial u}{\partial z} = \frac{\mu}{\rho} \left(\frac{\partial^2 u}{\partial x^2} + \frac{\partial^2 u}{\partial y^2} + \frac{\partial^2 u}{\partial z^2} \right) - \frac{1}{\rho} \frac{\partial p}{\partial x} \quad (5.11a)$$

$$u \frac{\partial v}{\partial x} + v \frac{\partial v}{\partial y} + w \frac{\partial v}{\partial z} = \frac{\mu}{\rho} \left(\frac{\partial^2 v}{\partial x^2} + \frac{\partial^2 v}{\partial y^2} + \frac{\partial^2 v}{\partial z^2} \right) - \frac{1}{\rho} \frac{\partial p}{\partial y} \quad (5.11b)$$

$$u \frac{\partial w}{\partial x} + v \frac{\partial w}{\partial y} + w \frac{\partial w}{\partial z} = \frac{\mu}{\rho} \left(\frac{\partial^2 w}{\partial x^2} + \frac{\partial^2 w}{\partial y^2} + \frac{\partial^2 w}{\partial z^2} \right) - \frac{1}{\rho} \frac{\partial p}{\partial z} + g \quad (5.11c)$$

$$u \frac{\partial T}{\partial x} + v \frac{\partial T}{\partial y} + w \frac{\partial T}{\partial z} = \frac{k}{\rho c_p} \left(\frac{\partial^2 T}{\partial x^2} + \frac{\partial^2 T}{\partial y^2} + \frac{\partial^2 T}{\partial z^2} \right) \quad (5.12)$$

where u , v , and w are velocity components in x , y , z direction, respectively; ρ is density, μ is dynamic viscosity, p is pressure, T is the temperature, g is gravitational acceleration, k is thermal conductivity coefficient of the media, and c_p is heat capacity. The solid is assumed as an isotropic body with temperature-dependent heat transfer, following:

$$\frac{\partial}{\partial x} \left(k \frac{\partial T}{\partial x} \right) + \frac{\partial}{\partial y} \left(k \frac{\partial T}{\partial y} \right) + \frac{\partial}{\partial z} \left(k \frac{\partial T}{\partial z} \right) + Q = \rho c \frac{\partial T}{\partial t} \quad (5.13)$$

Here, $Q = Q(x, y, z, t)$ is the inner heat-generation rate per unit volume and t is time. In steady-state conditions the time-dependent variable is removed from the equation. For the current work there is no

heat generation term. In order to complete this set of equations, additional relations are required to link heat transfer and transport properties of air. Air properties can be assumed to change according to the ideal gas law. Due to small variation in air temperature, specific heat capacity can be assumed to be constant, being evaluated at the mean air temperature. The buoyancy and radiation effects have been disregarded.

The herringbone-fin geometry achieved earlier is within the validity region of the Wang's empirical correlation. However, for validation purposes, the geometrical parameters were slightly changed in order to match a specific configuration used in the experimental study of Wang [93]. The experimental data with the most similar geometry that was found consists on tube collar diameter of 10.3 mm ; two staggered rows, with the same transversal pitch of 25.4 mm and longitudinal of 19.05 mm . Fin pitch is 3.53 mm ; tube wall thickness is 0.35 mm and waffle height is 1.5 mm . Wang [93] does not provide any information regarding the material used, so copper was selected. Other geometrical properties were carefully replicated during the model construction, following the drawings provided in [93].

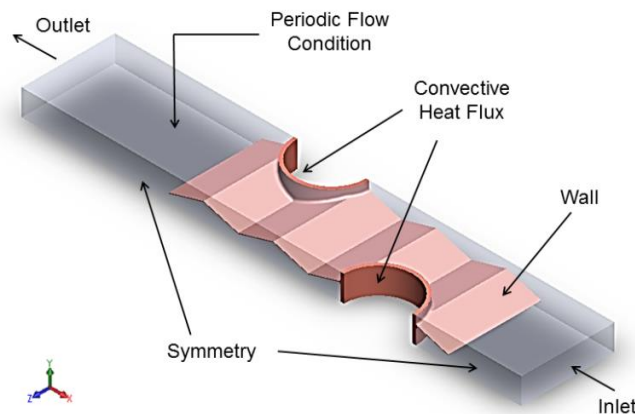


Figure 5.5 – Numerical model and boundary conditions used.

Figure 5.5 depicts the view of the simulated domains; for the fluid-dynamic analysis, the boundary conditions are:

- Symmetry on the lateral sides of both the solid domain and fluid domain;
- Periodic flow condition on the top and on the bottom of the fluid domain;
- Constant longitudinal velocity u_x ($u_y = u_z = 0$) at the inlet of the fluid domain according to the desired Reynolds number and static atmospheric pressure at the outlet;
- No-slip condition at the wall interface between the solid and the fluid domain;

For the solid domain, the boundary conditions are:

- Adiabatic condition on both lateral sides;
- Periodic heat flux on the upper and bottom transversal section of the tubes;
- Imposed convective heat flux on the inner half-side of the tubes, with $T_{\infty} = 34^{\circ}\text{C}$ and $h = 1969 \text{ W/m}^2\text{K}$, according to Equation 3.4;

A multi element unstructured grid was used comprising tetrahedral elements, within the flow stream away from the walls, while boundary layer elements were added close to the walls. Since the velocity changes very rapidly in the direction normal to the wall, close to the boundary and very little in the tangential direction of the wall, quadrilateral elements were used for the boundary layers, tightly packed in the direction normal to the wall and more sparsely in the tangential direction. Mesh refinements were added for all the sharp edges, and the resolution of curvatures and narrow region were successively improved. In addition, the number of finite elements, and thus also the number of degrees of freedom, was successively increased, to investigate whether the quantities of interest were dependent on the mesh chosen. The quantity of interest under investigation was chosen to be the total energy balance between inlet and outlet of the fluid domain as follow

$$Q = \iint_{inlet} \vec{v} \cdot \vec{n} \rho(T) C_p(T) T dA + \iint_{outlet} \vec{v} \cdot \vec{n} \rho(T) C_p(T) T dA \quad (5.14)$$

A sensitive analysis of the mesh was carried out in order to avoid any mesh dependent results. Table 5.3 depicts the grid independency study conducted, concerning the energy balance at the fluid domain boundaries as variable of interest.

Table 5.3 – Grid independency study; $Re_{dc} = 1010$

Physics induced setting	Number of domain elements	Degrees of freedom	Q [W]
Extra coarse	14960	26928	0.3618
Coarser	37388	65429	0.3618
Coarse	53403	90785	0.331
Normal	111487	183953	0.3008
Fine	218498	349596	0.2774
Finer	415896	644638	0.2991
Extra fine	836183	1254274	0.2719

The results show that the solution was mesh dependent, since the quantity of interest varied even for very fine meshes that consisted of a large amount of elements. Thus, due to lack of more computational resources, a slightly coarser mesh was chosen, for both models, to improve the

simulation speed, settling for a number of degrees of freedom around 200 000. The resulting mesh, as well as a qualitative velocity magnitude in the fluid domain and temperature distribution in the entire domain is shown in Figure 5.6.

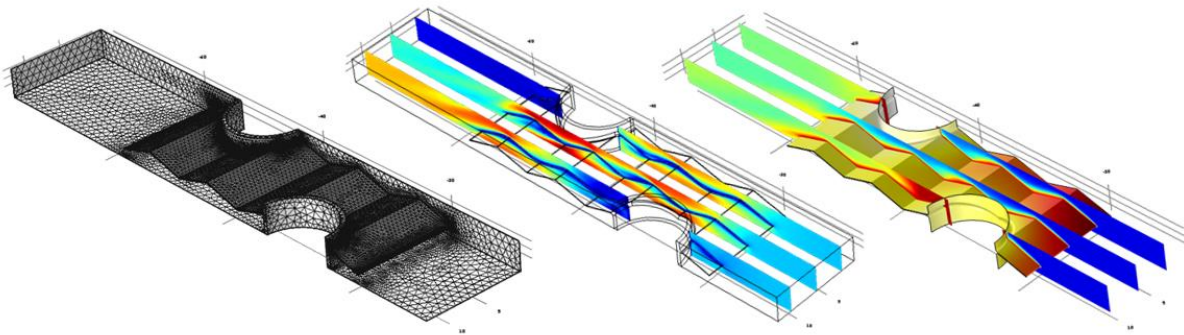


Figure 5.6 – a) Fluid and solid discrete domains; b) Qualitative velocity magnitude; c) Qualitative temperature distribution in the solid and fluid.

Using the mesh settings, as represented in Figure 5.6, the inlet air velocity was changed in order to match the Reynolds number range studied by Wang, for validation purposes. Two approaches were considered here: 1) using the fluid-side energy balance, numerical results were compared with those expected from the F-LMTD method, using the j -Colburn factor from Wang’s correlation. 2) The numerical heat flux and inlet and outlet temperatures were used to calculate the numerical j -Colburn factor and compared with that provided by the correlation. Results are presented in Figure 5.7.

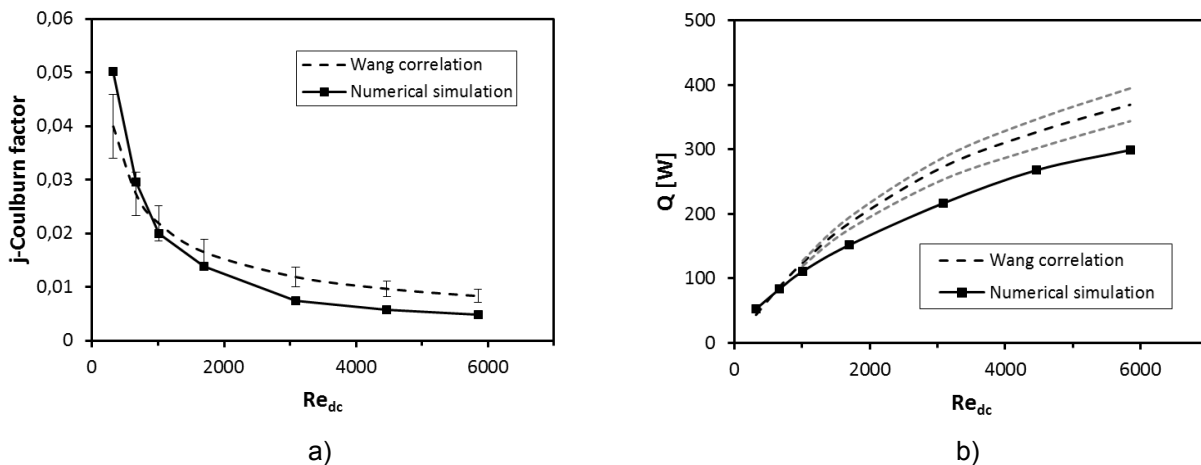


Figure 5.7 – a) Wang's correlation j -Colburn factor comparison with numerical results; b) Heat transfer rate comparison

Wang reported that 91% of the experimental test data used to derive the heat transfer correlation are within $\pm 15\%$ deviation from predicted j values. Thus, this percentage value was plotted in the j -Colburn graph, as well as the propagation to the derived heat transfer rate, as represented by dashed lines in Figure 5.7 b). Maximum heat transfer rate relative deviation is 21%, which is the quantity of interest for this study. From a qualitative analysis one can conclude that the numerical simulation tends to underestimate the heat transfer rate, particularly at higher Reynolds number ($Re > 2000$). This deviation can be explained as follows: a laminar flow model was used and although the author of this correlation did not make any reference to the flow regime, a transitional flow is expected at low

Reynolds number of 2000 according to [94]. Hence, laminar separation occurring at the sharp wavy fins could result in an early turbulent wake, which is not being correctly simulated with the laminar model employed. Also, several assumptions were considered when modelling the solid domain geometry. The simplifications introduced should not result in a significantly different flow, but Wang used the actual surface area of the fins and tubes which is not specified in his study. This could induce errors in the heat transfer area calculation using only the geometrical properties, thus the modelling simplification could reduce the effective heat transfer area, underpredicting the results. In fact, considering the practical application of the numerical CFD simulation to the flat tube and serpentine fin configuration, geometry is much simpler and Reynolds number based on hydraulic diameter is never higher than 2000, due to the inlet air velocity imposed by the 12VDC fan. Hence, one may argue that, globally, the numerical results show reasonable agreement with the experimental j -factor correlation proposed by Wang [91], confirming the suitability of the formulated simulation tool to predict the air-side heat transfer coefficient of the condenser.

The available geometry at Sorradiadores, to be simulated consists on flat copper tubes with plain copper serpentine fins. The geometrical parameters are depicted in Figure 5.8.

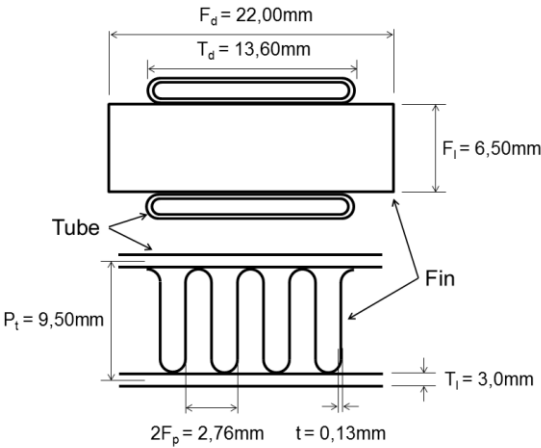


Figure 5.8 – Flat tube with plain serpentine fins geometry from Sorradiadores.

Under the assumption that for the flat tube the inner convective condensation heat transfer coefficient may be described using the correlation proposed by Chato [76] based on the inner hydraulic diameter of the tube, the procedure described in the previous paragraphs was repeated. The inlet air velocity is 2.18m/s corresponding to the maximum rotational speed of the fan. The Reynolds number based on the air-side hydraulic diameter is 280. Concerning boundary conditions, due to the different geometry, all the fluid domain boundaries are selected as symmetry. Exception is made to the inlet and outlet. The boundary conditions are the same as used in the previous model. An illustrative view of the model, mesh and the temperature distribution in both domains, for the conditions described is shown in Figure 5.9

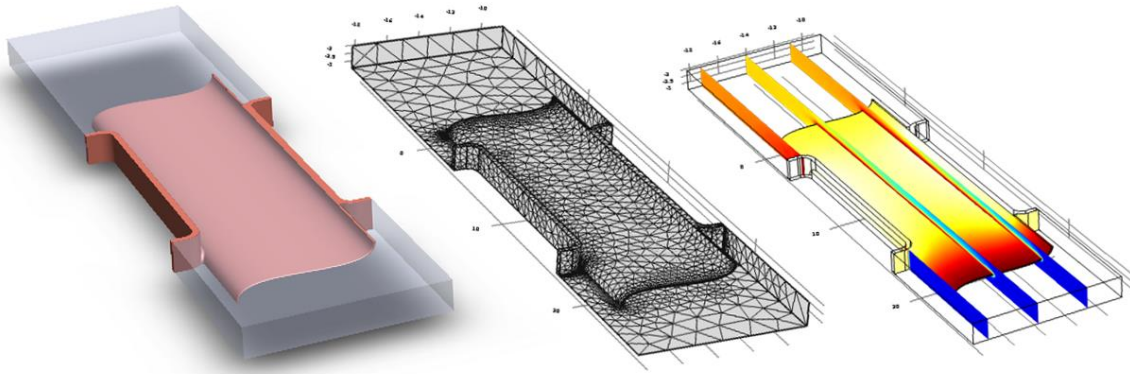


Figure 5.9 – a) CAD model; fluid and solid domain mesh; c) Qualitative temperature distribution in both domains for $Re_{Dh} = 280$

The resulting heat transfer rate is 217 W at atmospheric pressure, which is an acceptable value, providing a safety margin of 1.45 (compared to 150 W). Furthermore, it is worth mentioning that the inner side convective heat transfer was calculated based on the coefficient of Chato's [76] correlation which is a safe approach. Also, the convective interior condensation performance is expected to increase due to tilt angle effects according to [80], which was not considered here. In fact this geometry is more compact ($\alpha = 1205\text{ m}^2/\text{m}^3$ and the herringbone finned tube is $\alpha = 601\text{ m}^2/\text{m}^3$), which, due to the severe restrictions in terms of dimensions to implement the cooling system in the desktop tower, is particularly valuable. The simulation shows that a single row of flat tubes with the same frontal area of $120\text{ mm} \times 120\text{ mm}$ is sufficient. This results in a depth of 22 mm , almost half of the previous geometry which was 38 mm .

Figure 5.10 depicts a photo of the condenser which was manufactured based on the outputs of the numerical study.



Figure 5.10 – Condenser manufactured according to technical drawings by Sorradiadores.

5.2.3. Experimental facility overview

As a starting point, the condenser was placed directly above the evaporator. An auxiliary system was also developed to improve the degassing process, namely an outer condenser was installed with its outlet connected to a reservoir where exhaust liquid fluid is collected during the degassing procedure. The previous instrumentation designed for the proof-of-concept prototype (Section 5.1) was further improved. Hence, the ADC acquisition unit was replaced by a NI USB-6008 board from National Instruments, with the same 12-bit resolution, but comprising more channels and improving the acquisition frequency to 1.0 kHz . Also, due to the higher input voltage of the aforementioned board, the voltage dividers developed in section 5.1 were recalibrated, increasing the acquisition resolution by a factor of 3. The PID parameters were changed due to the different installed condenser. Four extra 0.5 mm K-type insulated probe thermocouples were added to the inlet and outlet of the evaporator and condenser. The thermocouple acquisition unit was also changed to reduce the high absolute uncertainty of $\pm 2^\circ\text{C}$. All the seven K-type thermocouples are now acquired with a Data Translation DT9828 12-bit ADC cold-junction compensated. Besides the gauge pressure transducer implemented on the first prototype, two Honeywell 24PCB, 5psi, differential pressure transducers with current output and with 0.25% accuracy were amplified with a home-made high precision low-noise amplification circuit. The circuit's schematics may be found in Annex A.4. The remaining acquisition sequence, instrumentation and electronic circuits were kept unchanged. Figure 5.11 depicts an overview of the devised cooling system.

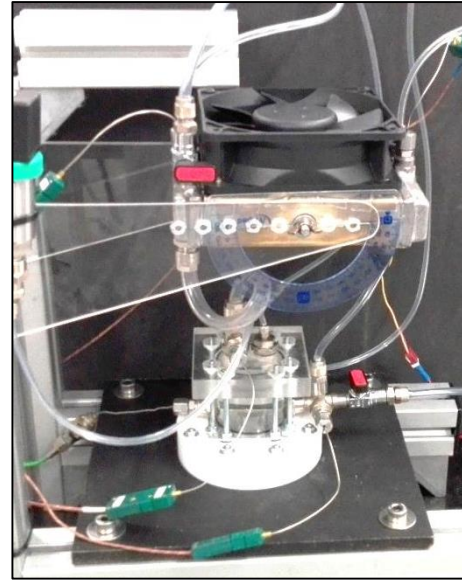
5.3. Experimental methodology

At the beginning of each test, the working fluid is degassed, according to the following procedure: the entire inner volume of the loop is filled with the working fluid while the remaining air is vacuum pumped. The controlling circuit is set to maximum dissipation power of 150 W and when the inner pressure achieves 1.5 bar , the exhaust valve at the highest location of the loop is opened, thus allowing the vapor and non-condensable gases to escape. The valve is closed and the fan is turned on, reducing the inner pressure. The loop proceeds with boiling and condensation phase change for 10 minutes, after which the fan is turned off, thus allowing the pressure to increase rapidly. This procedure is repeated for several times, until 20 mbar of difference is achieved between the saturation liquid temperature and pressure measured inside the evaporator, according to equation 5.1. Excess liquid beyond the desired level is removed, opening the evaporator fill valve.

Several surfaces with different distance between micro-cavities were tested in order to infer on the expected heat transfer enhancement as introduced in Chapter 3. Cavity depth and diameter are fixed parameters and equal to $15\text{ }\mu\text{m}$ and $100\text{ }\mu\text{m}$ respectively. Distance between cavities was changed as $800\text{ }\mu\text{m}$, $600\text{ }\mu\text{m}$, $400\text{ }\mu\text{m}$ and $300\text{ }\mu\text{m}$. The results obtained with a smooth surface were used as reference. This set of experiments was performed under steady-state conditions.



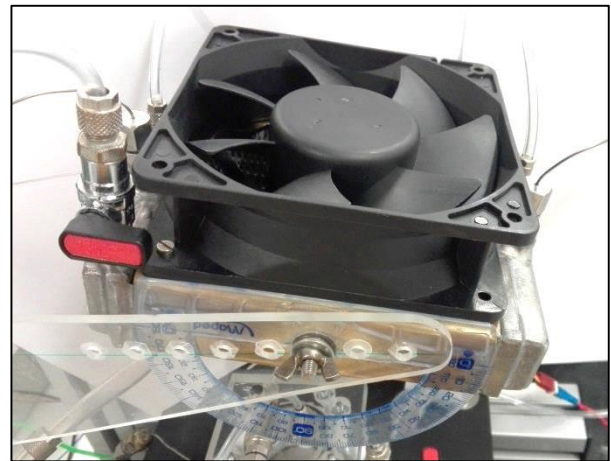
a)



b)



c)



d)

Figure 5.11 – Overview of the experimental facility. a) Overview; b) detail of the test section; c) Evaporator; d) Condenser.

As a first approach, a careful investigation of the loop thermal characteristics and working conditions depending on the heat load are addressed, inferring on the thermo-physical properties dependent on the loop behaviour. From this point and beyond, these will be called as real working conditions. The overall thermal resistance of the cooling system following this parametric study on cavities distances is addressed under these conditions. In contrast, via a PID controller the inner pressure and liquid and saturation temperature are controlled by the condenser fan rotational speed, and the thermal resistance is calculated under this controlled environment. In both situations, small steps of 5 W are applied until 40 W and then steps of 10 W successively up to 150 W . Steady-state temperatures pressure and dissipated power are monitored for 10 seconds at 1.0 kHz , computing the mean value and standard deviation. Each test is repeated three times for increasing and decreasing heat flux, for all the surfaces and under both experimental conditions.

To test the system in real processing situations, a typical power profile depicted in Figure 5.12 is imposed via pre-programmed micro-controller acting on the transistor power control circuit, based on the work of Isci and Martonosi [95], which simulates four separate CPU operations. Hence, the first region, from 20 to 45 s, is designed to simulate the processing of computations in a cycle between integers and floating point. The second region, from 45 to 60 s, simulates a benchmark generating level 1 cache hits. The third region represents a benchmark specifically designed to generate Taken Branches and finally, the fourth region, is a rapid variation in power between 35 and 55 W simulating the actual use of the program *Gnumeric*. The system idle power (power dissipation at rest) is 10 W. The tests performed consist on sudden routine trigger, once the entire system is at ambient temperature, inferring on the time resolved junction temperature of the simulated CPU heat source.

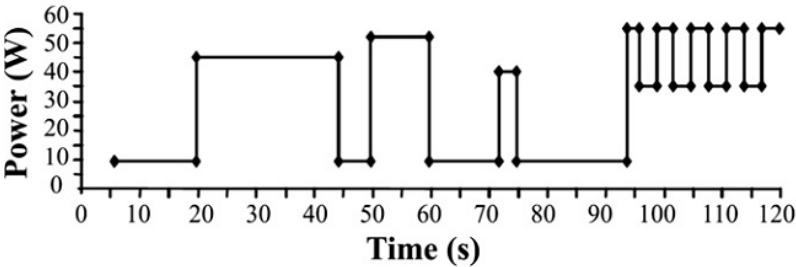


Figure 5.12 – Typical power profile of an Intel Pentium 4 used in the transient tests [95].

Following the micro-structured surfaces analysis, a different transient test condition was considered. Power steps of 40, 60, 80, 100 125 and 150 W were suddenly applied and the resulting time resolved junction temperature was acquired. Each experimental condition was repeated three times.

Concerning the multi-parameter exploratory investigation that follows, which was performed to devise the final cooling system, the methodology adopted might be better understood by analysis to the chart depicted in Figure 5.13.

Where S_n states for the several surfaces investigated in terms of overall thermal performance as already introduced in this section. Mainly, the surface providing the best system performance is selected. For this surface, two condenser arrangements C are tested, namely the regular and reflux configuration, as introduced in Section 3.3. Both configurations are subjected to a study on the inclination effects ϕ_n and various liquid fill charges L_n addressing the performance in terms of overall thermal resistance. Then, the effect of evaporator orientation is addressed, which mainly consists on changing it from the horizontal to the vertical position, O_2 . Finally, to different sizes of the evaporator (mainly resulting from varying the bottom diameter, D) are tested. Using the final resulting 2 configurations, the Liquid fill charge that maximizes performance is found, based on a comparative analysis between these 2 final configurations. Finally, the last geometry parameter changed is the evaporator height H , in which a liquid fill charge study is also conducted.

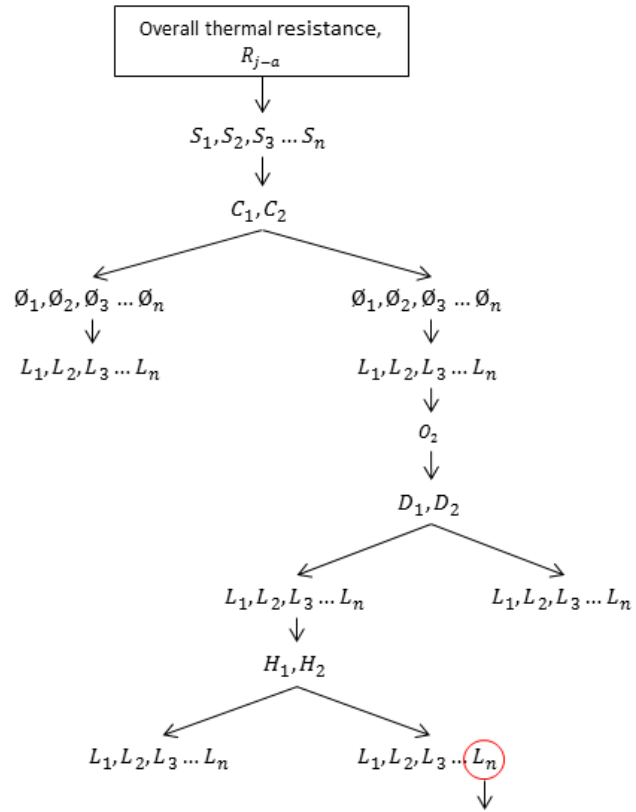


Figure 5.13 – Methodology algorithm employed within the multi-parameter exploratory investigation. Red circle denotes an illustrative final geometry achieved.

6. Results and discussion

6.1. Loop characterization and working conditions

This first sub-section intends to characterize the working conditions, namely steady-state temperature distribution along the loop, governing pressure and also start-up behavior of the two-phase closed loop thermosiphon, which was designed and assembled as described in the previous chapter. For this purpose, the results presented and discussed in the next paragraphs were obtained using the following configuration: a smooth non-structured aluminum surface; a 40 mm inner diameter and 40 mm height evaporator, filled with the same working fluid fill charge of 30 ml, as used in the proof-of-concept prototype; the condenser positioned with a -30° tilt angle in order to enhance hydraulic drainage of the liquid film condensed, as suggested by [81]; the ULTRAKAZE DFS123812H-3000 fan, as tested in the proof-of-concept prototype. The fan was set to run always at maximum speed (2700rpm).

The initial loop pressure is set as the saturation pressure at ambient temperature, which was kept constant at $23\pm 1^\circ\text{C}$. The measured pressure could never match exactly the vapor pressure value predicted by equation 5.1, even after the degassing process. However measured value was at most 20 mbar higher than the predicted one, resulting in a maximum increase of liquid saturation temperature of 0.8°C , which is considered acceptable.

On the other hand, the working pressure within the loop increases with increasing heat load, as the mass flow rate (mostly vapor mass) increases, being unbalanced by the mass flow rate that is condensed. However, the heat transfer coefficient in the condenser increases with increasing pressure, at higher heat loads and consequent higher mass flow rates. So, the new equilibrium state is attained at a higher pressure. This means that, for the same ambient temperature and condenser fan velocity, the liquid saturation temperature inside the evaporator increases with increasing heat load, as well as all the temperatures measured along the loop. This trend is depicted in Figure 6.1.

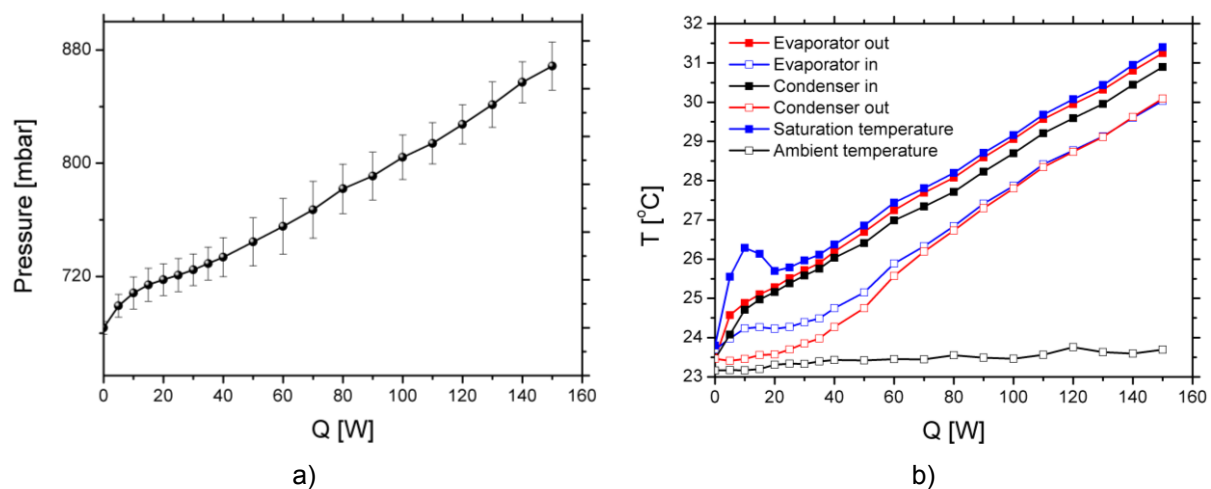


Figure 6.1 – Steady-state pressure and temperature measurements along the loop as function of dissipated power. a) Absolute evaporator pressure; b) Temperature distribution.

As an illustrative example, Figure 6.2 represents the thermodynamic cycle in terms of p-h diagram under steady-state conditions, at 150 W of thermal load. At the outlet of the evaporator, the measured fluid temperature is close to the saturation temperature at the measured vapor pressure in the evaporator. At this extreme heat load, vapor quality is assumed to be lower than 1 due to the visible presence of vapour-liquid mixture arising from the evaporator pool. Furthermore, temperature and pressure decrease is attributed to friction losses in the vapor line and sudden contraction and enlargement caused by the vapor line connecting the evaporator reservoir to the plenum chamber, at the inlet of the condenser and descending pressure head. Vapour condenses in the downward facing condenser with notorious sub-cooled liquid at the outlet. This is caused by the geometry of the gravity assisted condenser, in which stratified flow with thin liquid film falling attached to the bottom wall of the tubes is drained due to the hydraulic gradient imposed. In the stratified regime, pressure losses are negligible owing to the quiescent vapour condition assumed inside the condenser and confirmed, based on the available measurement instrumentation. The rise in pressure is caused by the ascending fluid head along the tilted condenser. Downstream the condenser the gravitational-type pressure head, which impels the liquid into the evaporator, develops and reaches a maximum at the inlet of the evaporator. Moreover, it is qualitatively considered to be in reasonable agreement with the results reported by [96, 97], despite these studies mainly concern a single pipe closed loop thermosyphon. Also, this scenario remains valid through the wide range of heat loads tested, as one can conclude by inspection of Figure 6.1b.

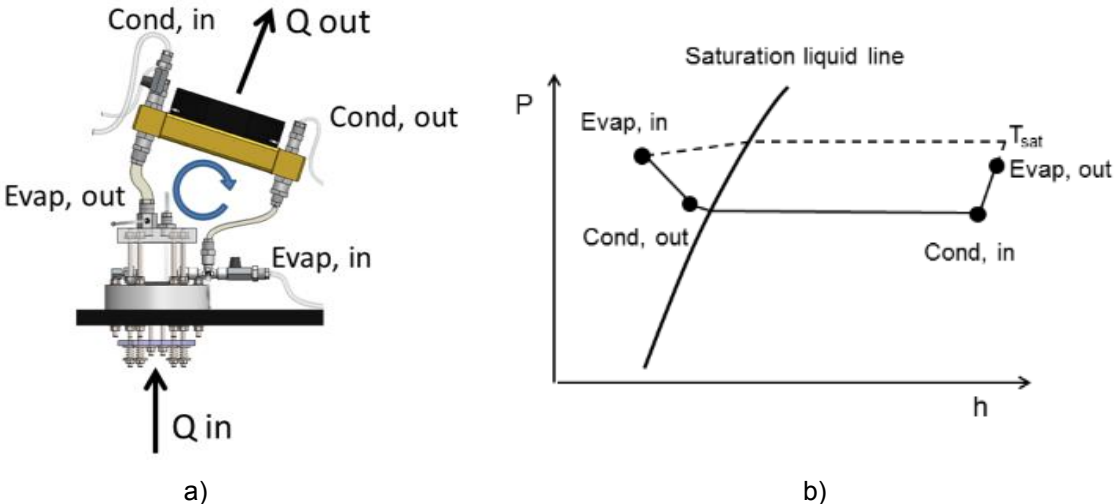


Figure 6.2 – Thermodynamic cycles of the developed loop thermosyphon. a) Combined temperature and pressure measurement locations; b) p-h diagram under steady-state conditions at 150W.

To complete the general overview of the thermodynamic properties characterization along the loop and as function of heat load, the liquid level inside the evaporator is also worth to mention. The ratio between the initial liquid free surface height and measured height as function of heat load is depicted in Figure 6.3 by means of still photographs combined with the abovementioned results.

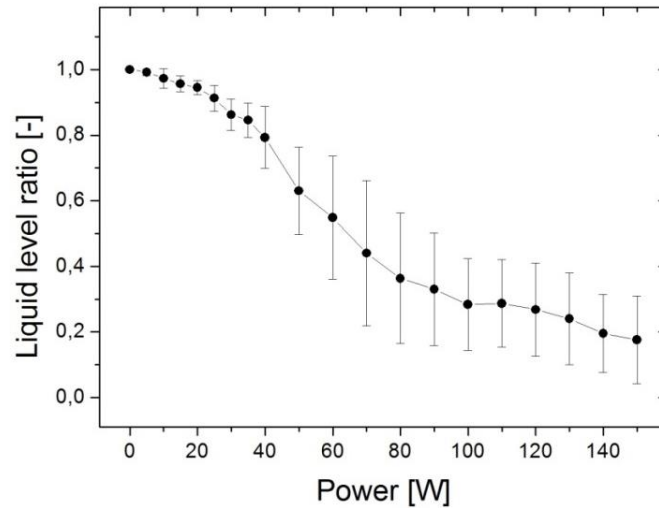


Figure 6.3 – Liquid free surface height ratio as function of heat load. Error bars indicate the standard deviation of consecutive measurements.

It is commonly argued that the driving force of the condensation liquid return is the liquid position difference between that in the liquid return line and that of the evaporator. This is qualitatively confirmed by the measured pressure difference between the evaporator and the liquid inlet. Furthermore as the mass flow rate increases with increasing power, friction losses also increase, which results in a corresponding liquid height decrease in the evaporator. Hence the liquid level ratio decreases, as function of heat load as expected. However, Figure 6.3 also shows a higher decrease rate for increasing heat loads, which cannot be explained just by friction losses. This can be attributed to the contribution of the following effects: temperature measurements in the evaporator inlet line at system transient phase start-up suggest that the first condensed liquid returns to the evaporator after just 4 seconds, for $Q=150\text{ W}$. Assuming that a steady-state mass flow rate balance in the evaporator control volume is attained at this point, an upper bound of just 3.3 ml of vaporized fluid difference is expected, which is responsible for a decrease in the liquid level ratio of 11%. However, it is worth mentioning that the large uncertainty in the liquid level measurement, due to the co-existence of liquid and vapour bubbles, with large bubbles which do not burst at the free surface, may strongly contribute to an underestimation of the liquid level, thus leading to an overestimation of the liquid level ratio. Qu [98] proposes that the increase in liquid surface due to the decrease in mixture density is 30% in average. Nevertheless, the trend in the liquid level ratio with the heat load is obvious and must be taken into account for an adequate design process, to avoid surface dry-out at high power loads.

At last, given that the nominal pressure inside the loop is not a controlled parameter, but a consequence of the loop working conditions, an objective evaluation of the system performance can be inferred based on the overall thermal resistance of the entire system (junction-to-ambient), defined as:

$$R_{ja} = \frac{T_j - T_{amb}}{Q} \quad (6.1)$$

The thermal resistance of the abovementioned baseline configuration is presented in Figure 6.4.

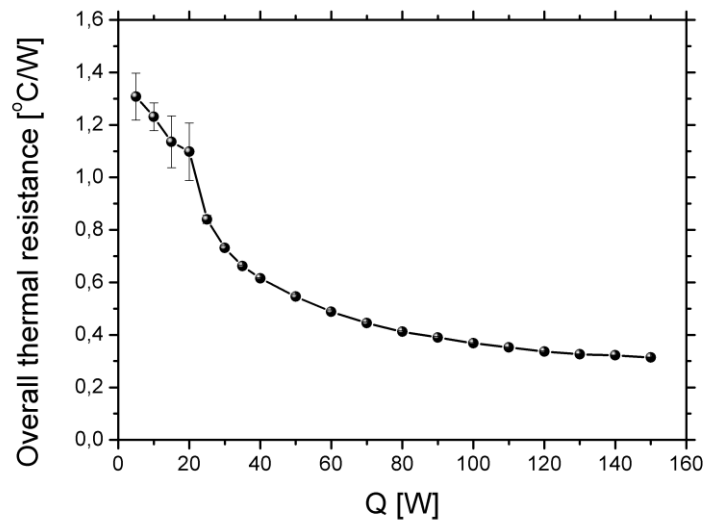


Figure 6.4 – Overall thermal resistance (junction-to-ambient) as function of heat load.

The overall thermal resistance decreases significantly with increasing heating power and maximum system performance occurs at 150 W. The accordingly total thermal resistance is 0.314 °C/W, which will be later used as a baseline for comparison on the resulting optimization with other results published in the literature.

6.2. Effect of surface micro-structuring

Following the arguments briefly presented in Section 3.2 the use of surfaces micro-structured with cavities in the evaporator is expected to improve the boiling heat transfer coefficient, and therefore to reduce the thermal resistance between the chip and the fluid, and ultimately the overall thermal resistance. The parametric study developed in this work focused on the distance between cavities, which consequently changes the number of cavities in the surfaces. The distance between cavities was varied as 800 μm , 600 μm , 400 μm and 300 μm . These values were selected based on previous studies reported in the literature [34]. The surfaces are tested under the so-called real working conditions, under controlled conditions and finally under transient conditions, as presented in the following sub-sections.

6.2.1. Steady-state analysis under real working conditions

As introduced in Section 5.3, real working conditions correspond to the situation in which the pressure and saturation temperature are not controlled parameters, but a consequence of the loop thermodynamic cycle. This condition is important to study, as it is the one occurring in practice.

Figure 6.5 depicts, for each one of the surfaces tested, an example of the resulting steady state heat flux and temperatures relation, in a representation similar to the Nukiyama boiling curves. The curves depicted here are obtained by both increasing and decreasing the heat load.

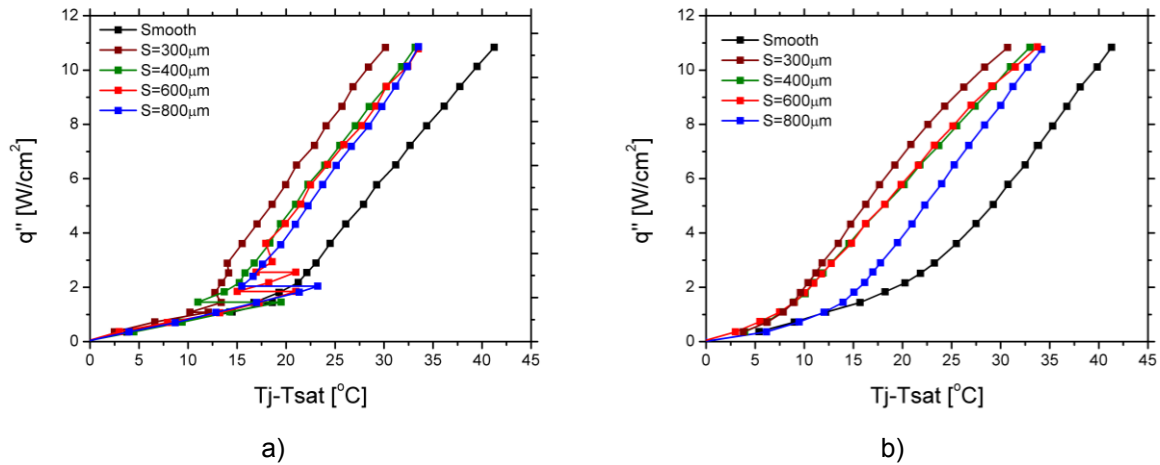


Figure 6.5 – Steady-state boiling curves under real working conditions. a) Increasing heat flux; b) Decreasing heat flux.

It is worth to mention that these are not boiling curves. First of all, mainly due to the practical and objective-oriented nature of this work, surface temperature was not acquired at any instance as the main variable of concern is the junction temperature of the simulated CPU. Also, recalling section 6.1, the working conditions inside the evaporator are dependent on the heat load applied. Hence, due to the raise in nominal pressure and consequent change in the liquid pool saturation temperature, the wall superheat, as considered in the Nukiyama's curves is evaluated at increasingly higher saturation temperatures with increasing heat load. Nevertheless, using the heat flux and temperature difference between junction and liquid, the resulting plot provides a familiar and easy way to understand the effect of surface micro-structuring in the performance of the cooling system, under actual working conditions, which are relevant for the application studied here. In this context, several characteristics are worth to be noticed and discussed. First of all, there is a notorious difference on the shape and slope of the curve, for the same surface, depending on whether the heat flux was increasing or decreasing (a detailed representation of this phenomenon can be better seen in Figure 6.6 for the surface with $S = 600\mu m$). This hysteresis phenomenon, which is associated to the activation of the nucleation sites, is well-known in the literature, but is particularly evident for the present working conditions. By combining temperature and heat flux measurements with still photographs of the boiling phenomena inside the evaporator, one can easily address the reason behind this distinct behaviour and possible implications to the performance of the device. Figure 6.7 shows images taken for four different heat loads (10W, 20W, 40W and 60W). In the left column, the heat flux is subsequently increased while in right column, the heat flux is subsequently decreased.

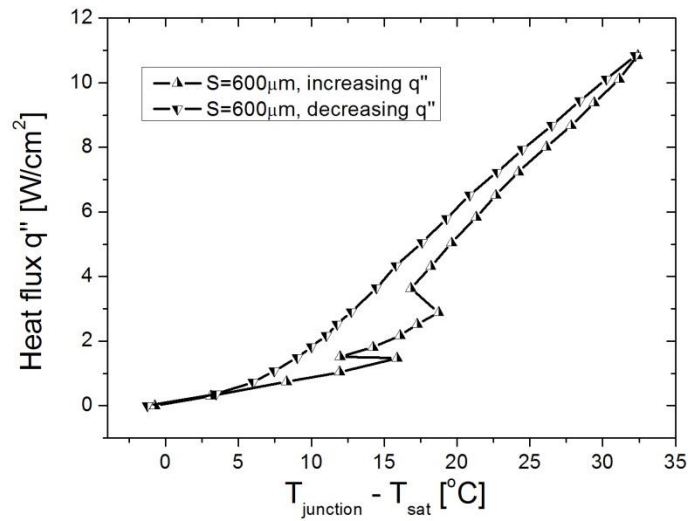
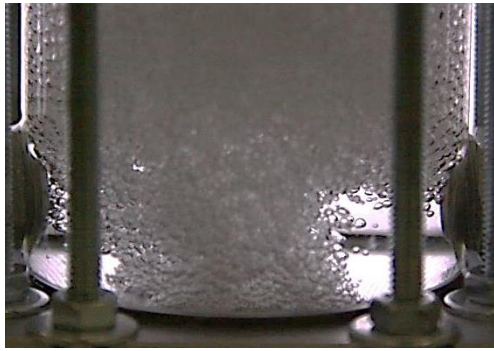
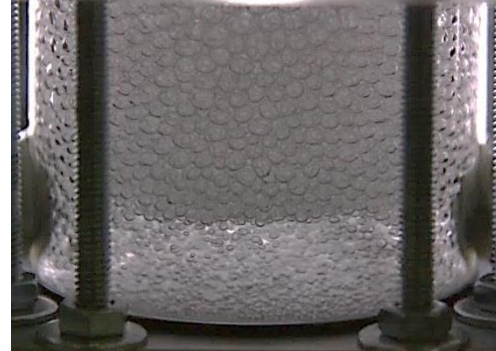


Figure 6.6 – Steady-state real working conditions boiling curve example for increasing and decreasing heat flux.

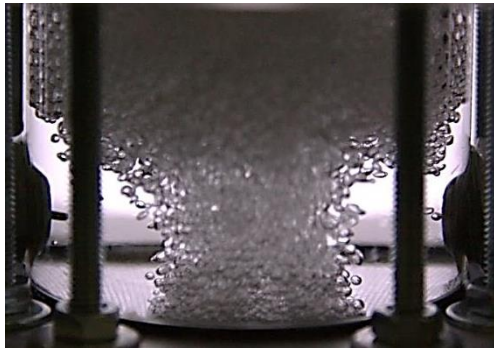
In Figure 6.6, two consecutive possible incipient boiling points stand out, at 20 W, and as the result of the onset of boiling, the junction temperature of the simulated die decreases. However it is also noticeable that only a small number of cavities became active, close to the centre of the surface. The active nucleation sites density naturally increases with increasing heat load (Figures 6.7a, c, e and g), although this increase is very subtle, for heat loads lower than 40 W. This may be due to the fact that a cavity which has just become active significantly reduces the local temperature of the surface and the surrounding cavities, thus requiring higher wall superheat to propagate the activation to new nucleation sites. At higher loads, a stochastic event takes place and a significant additional number of cavities become active. The increase of number of nucleation sites, although after the onset of nucleate boiling, obviously promotes the performance of heat transfer by enhancing all the boiling heat transfer mechanisms (as revised in section 3.2) simultaneously. From this point beyond, each increase of the applied power promotes the activation of an increased number of nucleation sites until eventually the entire surface becomes active. A completely different scenario happens when decreasing the heat flux, showing a great dependence on previous conditions. Once a nucleation site becomes active, due to the previous existence of a high enough wall superheat, the cavity remains active afterwards with smaller excess temperature. This behaviour is clearly noticed following the photographs taken at decreasing heat flux, and the ultimate influence may be clearly seen at only 10W of power, in Figure 6.7g and h, where with increasing heat flux the wall superheat was not enough to promote the onset of nucleate boiling, and in contrast, when decreasing heat flux, die temperature is significantly lower due to the existence of sparse active nucleation sites spread across the surface. The observation of this phenomenon raises awareness to the fact that as much as 10°C of difference on the effective die temperature may be observed for the same dissipated power, as well as the fact of the existence of a great dependence on the previous conditions. To cope with this, the present work also addresses transient conditions that will be exposed further in this chapter.



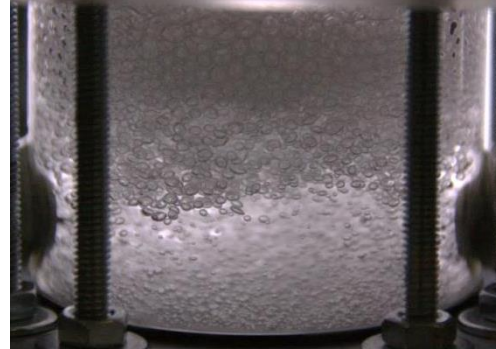
a)



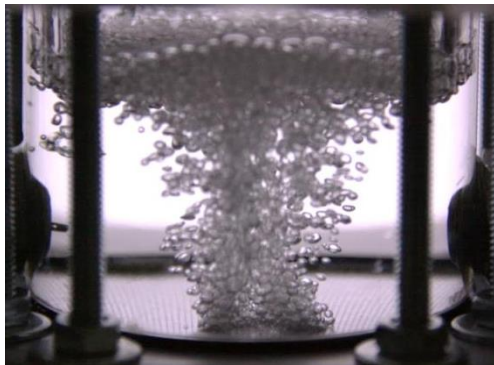
b)



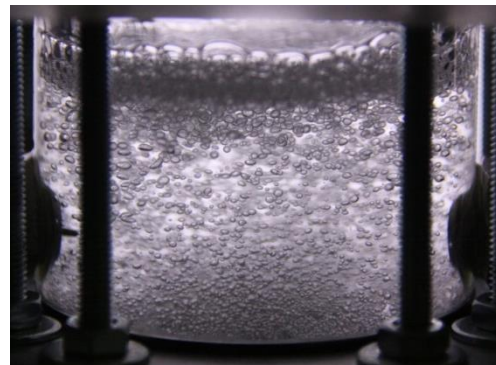
c)



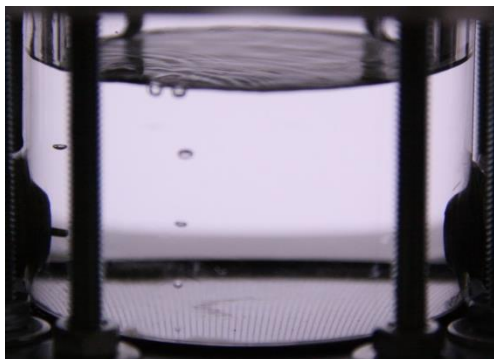
d)



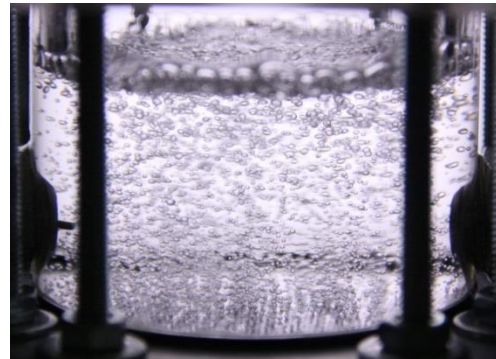
e)



f)



g)



h)

Figure 6.7 – Visualization of the boiling phenomena for increasing and decreasing heat flux with $S = 600\mu\text{m}$. a) 60W increasing; b) 60W decreasing; c) 40W increasing; d) 40W decreasing; e) 20W increasing; f) 20W decreasing; g) 10W increasing; h) 10W decreasing.

Anyway, the previous paragraphs simply evidence experimentally, the well-known phenomenon of hysteresis, which is particularly evident in the present work, possibly due to the spreading caused by the aluminum surface (and the CPU heat spreader).

Following this analysis, the effects of micro-structuring the surfaces are only investigated for the curves obtained by decreasing the heat flux. The thermal resistance is calculated for all the test surfaces, under real working conditions, and results are depicted in Figure 6.8 for the entire power range, and in Table 6.1 for 150 W.

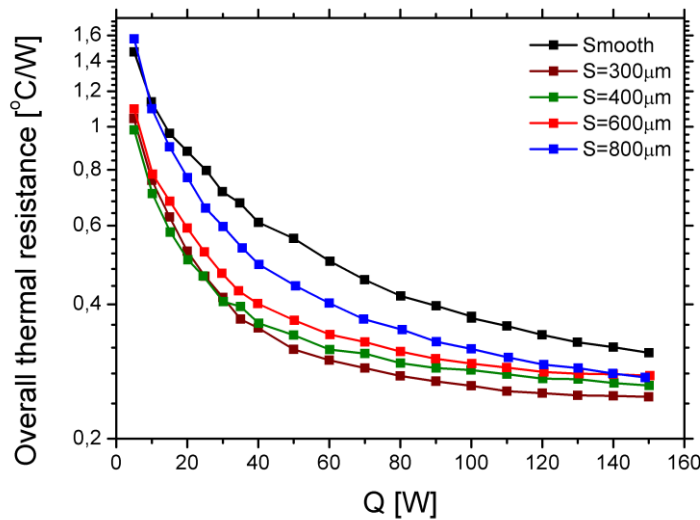


Figure 6.8 – Overall steady-state thermal resistance under real working conditions as function of cavity distance.

Table 6.1 – Overall thermal resistance as function of cavity distance at 150W under real working conditions.

S_c [μm]	T_{amb} [$^{\circ}C$]	T_j [$^{\circ}C$]	R_{ja} [$^{\circ}C W^{-1}$]	Improvement
Smooth	23.80	70.94	0.3143	-
800	23.56	64.42	0.2743	12.73%
600	22.90	64.50	0.2767	11.96%
400	24.73	64.23	0.2623	16.54%
300	24.10	61.33	0.2482	21.03%

The results depicted in Figure 6.9 and in Table 6.1 support that using the surface with 300 μm distance between cavities leads to the minimum junction temperature and, thus minimum thermal resistance, with an increase of performance of 21% at 150 W with respect to the smooth surface.

6.2.2. Steady-state analysis under controlled working conditions

The results discussed in this sub-section were obtained under controlled pressure (and consequent saturation temperature inside the loop) conditions. Under these conditions, the results are independent from ambient temperature fluctuations.

In order to maximize the heat load range, several set-point pressures were tested. For the set-point of 900 *mbar*, the system reaches stable conditions within the wider power range possible – 50 *W* to 150 *W*. Post-processing shows that among all the data points acquired in the abovementioned power range, inner pressure was maintained always within a maximum deviation of 3.12 *mbar* from set-point and corresponding liquid temperature at 31.3°C in average, among all collected data points, with standard deviation from the average measurements for each point of 0.2°C. The adopted methodology consists on starting every experiment at maximum power, thus maximizing nucleation sites activation and decrease step by step the heat load until 50 *W*. The boiling curves obtained with this procedure are presented in Figure 6.9. Each curve is averaged from 4 data sets, for each surface, two built for increasing power steps and two for decreasing power steps.

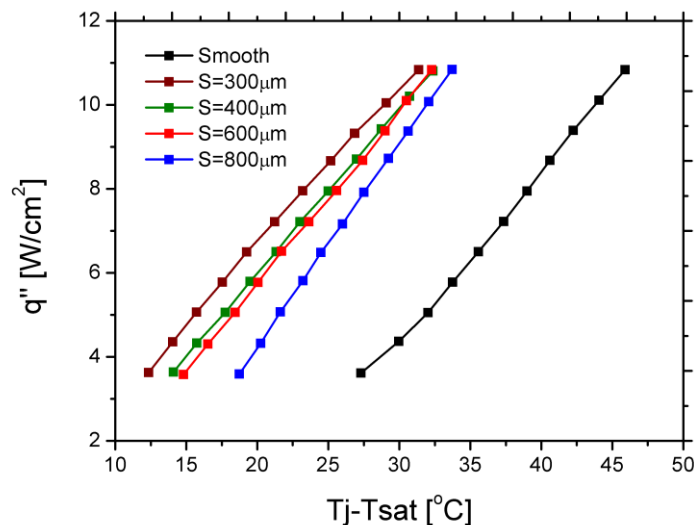


Figure 6.9 – Boiling curves under controlled pressure via PID.

A qualitative analysis of Figure 6.9 suggests that under these conditions the previous conclusion made on the performance of each surface remains valid. However, a more formal and quantitative study is required. Thus, taking advantage of the controlled conditions at which boiling curves are acquired, the abovementioned experimental results of the different surfaces are compared to the empirical results calculated from Rohsenow's boiling correlation [47], with a similar methodology used by [34, 50, 99, 100]. The pool boiling Rohsenow correlation can be simplified and rearranged in the form:

$$\left[\frac{c_{pf} \Delta T_{sat}}{h_{fg}} \right] = C_{sf} \left[\frac{q''}{\mu_f h_{fg}} \left(\frac{\sigma}{g(\rho_f - \rho_g)} \right)^{\frac{1}{2}} \right]^n \left[\frac{c_p \mu_f}{k} \right]_f^{m+1} \quad (6.2)$$

Where c_{pf} is the liquid specific heat, h_{fg} is the latent heat of vaporization, ΔT_{sat} is the wall superheat, q'' is the heat flux across the heating surface, σ is the surface tension, g the acceleration due to gravity, ρ the density, and μ_f is the viscosity of liquid working fluid. Values of C_{sf} , m and n , which relate to different nucleation properties of any liquid-surface combination, can be determined from the regression results of the experiment. The superheat is measured and heat flux imposed. Figure 6.10 compares the predicted values with the experimental results obtained for the different surfaces.

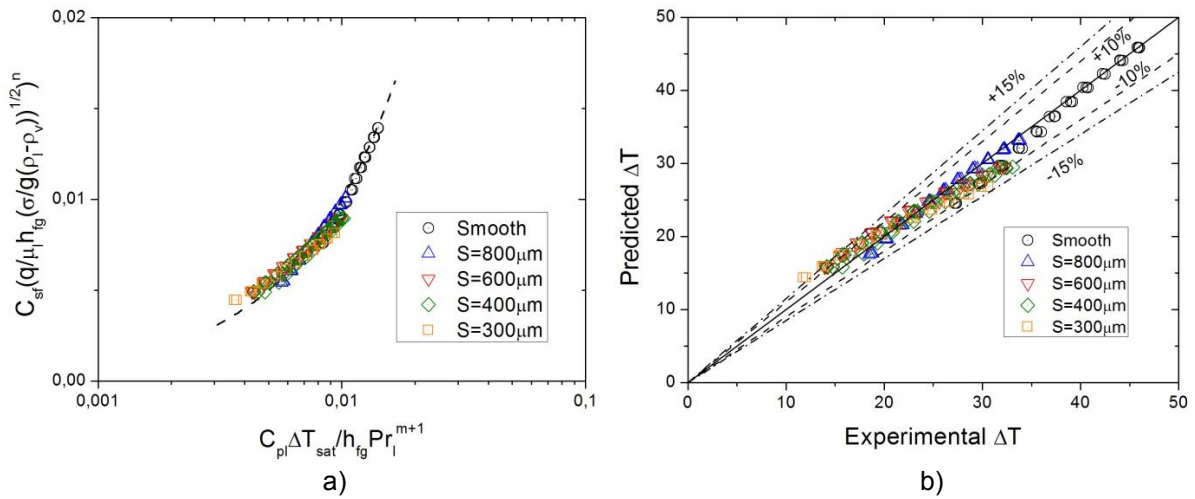


Figure 6.10 – Rohsenow correlation with experimental data. Predicted and experimental temperature superheat

The original Rohsenow's equation was fitted to the experimental data used by the author using values of $n = 0.33$ and $m = 0.7$ for fluids other than water. A detailed study of the values of C_{sf} and n for various liquid-surface combination and various surface preparations techniques has been reported by Vanchon *et al.* [100], however any published results for the combination of liquid-surface used in this present work (HFE-7000 on aluminum), were found. Nevertheless, with the procedure shown above, and keeping the value of $m = 0.7$ as originally recommended by Rohsenow, the average n is evaluated to be 0.569 for all surfaces, and the regressed value of C_{sf} is 0.0101 for the smooth surface, 0.0073 for $S = 800 \mu m$, 0.0064 for $S = 600 \mu m$, 0.0065 for $S = 400 \mu m$ and 0.0059 for $S = 300 \mu m$. This outcome suggests that the surface with $S = 300 \mu m$ works best among the five due to the smaller value of C_{sf} [34, 50]. However, care must be taken given that, as introduced in Chapter 3, the dependence between C_{sf} and the properties of the surface is usually determined from a strictly empirical fitting, being strongly dependent on particular experimental conditions. Consequently the values obtained in this fitting parameter do not necessarily correlate with the particular topographical properties of the surface, unless a particular study is performed in that context (Teodori *et al.* [34]).

Nevertheless, for the conditions tested here, Rohsenow's correlation is in fairly good agreement with the experimental, being the values of C_{sf} and n of the same magnitude and in rational agreement with

those reported in Vanchon *et al.* [100]. Hence, 89.2% of the experimental data points are within 10% deviation from the predicted values and 98.4% are within 15%.

Moita *et al.* in 2012 [71] and 2015 [101] developed a closely related study with the same working fluid and parametric study with distance between cavities. However, several experimental conditions were different, namely surface material and working pressure, and also the depth, shape and size of cavities were different. Nevertheless, a qualitative comparison concerning the effect of cavity distance in the relative enhancement of pool boiling heat transfer coefficient versus cavity distance is depicted in Figure 6.11.

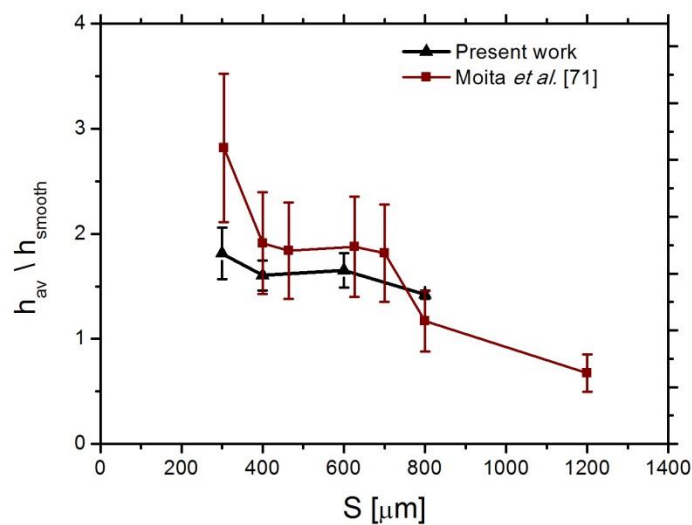


Figure 6.11 – Heat transfer ratio versus cavity distance

With the experimental data acquired under controlled pressure, and assuring that the nucleate boiling regime prevails, the average heat transfer coefficient was plotted, as function of heat flux, for all the micro-structured surfaces h_{av} and the relative increment in the heat transfer coefficient compared to that obtained with the smooth surface, h_{smooth} . The resulting data set (represented by the triangles) is then compared to that reported by Moita *et al.* [71]. Both data sets follow a similar trend, thus qualitatively confirming the role of the distance between cavities in the enhancement of the heat transfer coefficient. Discrepancies between the actual obtained values should be attributed to the diverse experimental conditions. It would be extremely simplistic to consider that the enhancement of the heat transfer coefficient is only linearly affected by the increase in the fluid/surface contact area and the increase of cavity density (obtained for smaller distances S) which are more likely to act as nucleation sites and promote the heterogeneous nucleation process. Several authors (e.g. Valente *et al.* [102]) also refer that the distance between nucleation sites influences the interaction mechanisms between departing bubbles, which in turn affects boiling performance. Hence, the distance between cavities must balance the positive effect of promoting the activation of nucleation sites with the negative effect of excessive interaction between them. In line with this, despite the different conditions, both parametric studies report a negligible change in the relative improvement of the heat transfer coefficient with the cavity distance of $S = 600 \mu\text{m}$ and $S = 400 \mu\text{m}$.

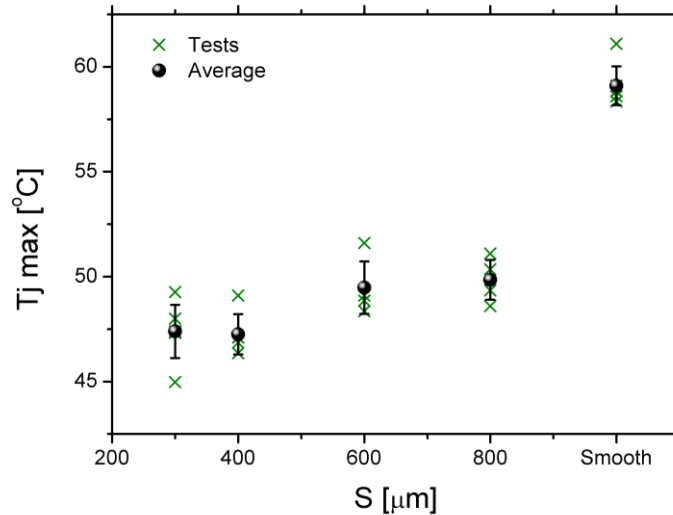


Figure 6.13 – Maximum junction temperature reached versus cavity distance.

The analysis performed up to now mainly stresses that lower junction temperatures and enhanced heat transfer coefficients are obtained when using structured surfaces, compared to the smooth surface taken here as reference. However, little difference is noticed when trying to compare different structured surfaces. One could conclude that in average a smaller distance between cavities is associated to lower maximum junction temperatures. However, non-negligible discrepancies are observed in the absolute values of the maximum junction temperature taken from each experiment. Hence, an alternative representation is depicted in Figure 6.13, which plots the actual data points, together with the averaged values and standard deviation.

At this point, it is clear that the onset of nucleate boiling is the governing phenomena and the main dependent variable acting on the junction temperature, for the heat load cycle tested here. Hence, instead of the whole heat load cycle, it is worth focusing on the response of the system to a sudden power step. According to the methodology presented in Section 5.3, power steps of 40 W, 60 W, 80 W, 100 W, 125 W and 150 W were suddenly applied as heat load and the resulting time resolved junction temperature acquired, for the five surfaces under examination. Figure 6.14 depicts an illustrative example of a typical step response.

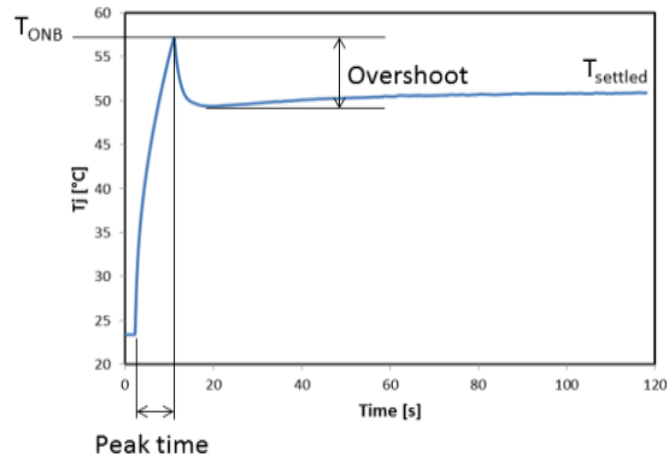


Figure 6.14 – Illustrative example of a typical junction temperature step response

Valuable results to withdraw from this set of experiments are the peak time, i.e., the time interval during which natural convection governed heat transfer is responsible for the rise in junction temperature prior to the onset of nucleate boiling; T_{ONB} which is the junction temperature at which nucleate boiling regime begins. The sudden increase in heat transfer coefficient associated to the onset of boiling leads to the step decrease in junction temperature is noticed afterwards. This temperature difference is called as overshoot temperature. This is an important factor to be addressed when using the devised system in pool boiling in IC cooling, due to the thermal stresses acting upon the component. Steady-state settled temperate is also worth to be addressed due to the fact that steady-state settled equilibrium pressure is much higher than the vapor pressure at rest.

Figure 6.15a depicts the average peak time as function of applied power step for all the surfaces under examination.

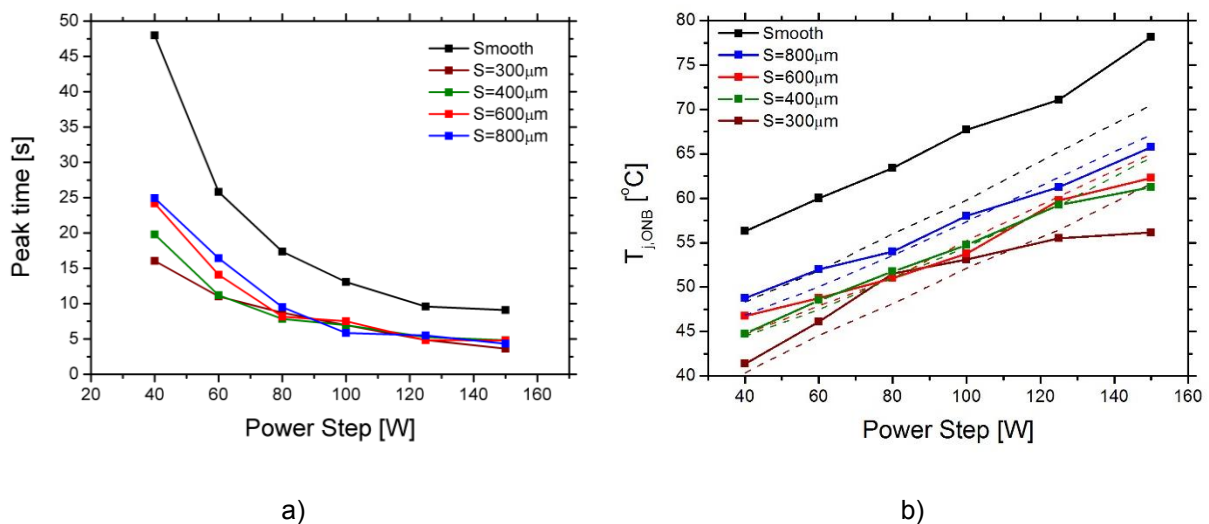


Figure 6.15 – Average results as function of applied power step. a) Peak time at the onset of nucleate boiling for the five surfaces under examination; b) Maximum junction temperature at the overshoot, $T_{j,ONB}$. Dashed lines indicate steady-state settled temperature for the same heat load.

Concerning Figure 6.15a the first evident conclusion is that the onset of nucleate boiling occurs earlier for the structured surfaces, when compared to the smooth one. Also, the higher is the power step

intensity the lower is the peak time, obviously due to the natural convection regime prior to nucleate boiling, that begins at this point.

The results depicted in Figure 6.15a further suggest that smaller values of S lead to shorter peak times, for power steps lower than 70 W, although the curves seem to collapse at higher power steps (>100 W). Looking at Figure 6.15b, this plot suggests that the maximum temperature occurring at the overshoot caused by the onset of boiling appears for lower temperatures with decreasing cavity distance. Since the raise in temperature prior to this event is caused by natural convection, lower temperatures are attained in shorter periods of time. Comparing the peak temperature to the settled temperature, for the same power load, one can safely conclude that at higher heat fluxes the temperature overshoot is never higher than what would be expected under settled steady-state conditions, for all the structured surfaces. Moreover, one can further infer that this difference is increasingly notorious with lower cavity distances.

Finally, it is worth to further examine the sudden decrease in junction temperature, which is quantified as the difference between the maximum peak temperature and minimum temperature after the overshoot. These results are summarized in Table 6.2.

Table 6.2 – Average temperature overshoot at the onset of nucleate boiling under sudden power step.

	40 W	60 W	80 W	100 W	125 W	150 W
Smooth	0.7	1.9	2.4	5.4	4.6	7.9
S = 800μm	5.0	5.5	4.3	4.5	4.0	4.8
S = 600μm	4.4	4.0	4.1	3.1	4.1	2.1
S = 400μm	1.7	2.2	3.8	2.2	1.0	1.0
S = 300μm	1.5	2.5	3.4	3.8	1.7	0.3

Due to the stochastic nature of the phenomenon and taking into account the small number of tests performed in the present study, one cannot extract relevant qualitative trends addressing the influence of applied power or cavity density on the results. In fact, the temperature decrease caused by the incipient boiling is affected by the number of cavities that become active, which is not a reproducible condition. Nevertheless, a global evaluation of the results allows concluding that the overshoot caused by sudden power steps is not relevant for the system design, as the attained temperature is never higher than that obtained at steady-state conditions at maximum power, and the sudden decrease in temperature recorded at the onset was always lower than 4°C for the surface with 400 and 300 μ m between cavities.

In an attempt to explain why different distance between cavities influence the intensity of overshoot and the temperature at which it occurs, small power steps were applied in order to find the wall superheat at which onset of nucleate boiling occurs.

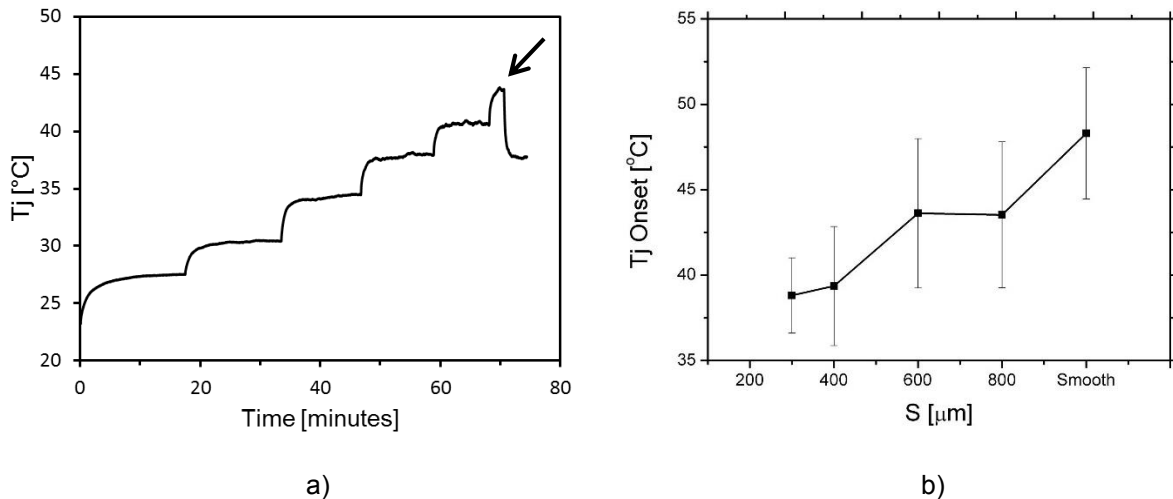


Figure 6.16 – Temperature of onset of nucleate boiling versus cavity distance. Arrow indicates the onset of boiling a) Experimental methodology; b) Results comprising average and standard deviation of the measurements.

By inspecting Figure 6.16 b) a trend is evident, suggesting that the onset of nucleate boiling occurs at lower temperatures. This result is mostly qualitative, as the precise determination of the onset of boiling requires very demanding experimental conditions and accurate measurements, as recently described in Bourdon *et al.* [103]. It is known in the literature that the wettability affects the onset of nucleate boiling [101, 104]. However, the wettability is not expected to vary much in the present working conditions. Also, the present results are not comparable to those reported by Bourdon *et al.* [103], given the significantly different experimental conditions. Also the surface topography is not comparable to that considered in the present study. Hence, one may only argue that due to the higher density of cavities per surface area, for the surfaces with smaller S , and due to the stochastic nature of the phenomena, boiling is probabilistically more likely to occur at lower wall superheat with increasing number of probable nucleation sites.

6.3. Condenser optimization

The overall thermal resistance of the loop thermosyphon is the sum of individual thermal resistance encountered in solid heat conduction, contact resistance and especially in the boiling and condensation equivalent thermal resistances. At this point of the discussion, the important role of the condenser in terms of the overall performance of the loop becomes evident. Enhancing the condenser inner side heat transfer coefficient leads to a resulting lower equilibrium pressure required to condensate the proper mass flow rate of vapour, thus decreasing the saturation temperature of the liquid in the pool boiling, with obvious beneficial implications in the junction temperature.

6.3.1. Effect of tilt angle

Lips & Meyer [81, 82] report under several different conditions, the effect of the inclination angle in the enhancement of the condensation heat transfer coefficient, inside tubes, as already introduced in Chapter 3. In their latest work [80], the authors conclude that despite the different tested conditions, the tilt angle which maximizes the heat transfer was always between 15° and 30° facing downward,

when using R125a as the working fluid. However, this optimum range of the tilt angle may vary, depending on the configuration. In fact, in the present configuration, the tilt angle affects many variables, such as the inlet and outlet vapour and liquid line angle or the positioning distance of the condenser relative to the evaporator. The pressure drop and liquid residence time are also affected by the condenser tilt angle, especially in gravity assisted condensers. These parameters were never reported in the literature, as argued by Lips & Meyer [81] on their review paper on this topic, although they must be considered, namely in the present work, as they can limit the applicable tilting angle to be selected. For instance, even if a high downward facing tilt angle could maximize heat transfer coefficient, it would not be feasible to implement due to the fact that the liquid outlet of the condenser has to be placed with a minimum distance to the evaporator in order to avoid flooding. This means that, for a high tilt angle, the vapour line had to be longer which would increase friction losses and also result in a possible overall geometry difficult to implement in the limited free space available inside a desktop. To avoid differences in the liquid and vapour line length as well as in the relative distance of the condenser when changing the tilt angle, the pipe lines were increased, the geometrical centre of the condenser was fixed and a paper duct was installed in order to avoid influence of the air direction leaving the condenser. Figure 6.17 shows an illustrative example of the experimental facility comprising three representative tilt angles. However, and despite all the efforts conducted to address the tilt angle influence in absolute, due to the lack of instrumentation to accurately address, solely, the potential improvement of the inner heat transfer coefficient, equilibrium pressure at steady-state heat loads was acquired, under the aforementioned assumption that the lower the equilibrium pressure for constant mass flow rate of vapor, the higher the condensation heat transfer coefficient, for the same air-side inlet temperature and flow rate. Figure 6.18 depicts the results in terms of overall equivalent thermal resistance, in steady-state, for the entire range of tested heat loads.

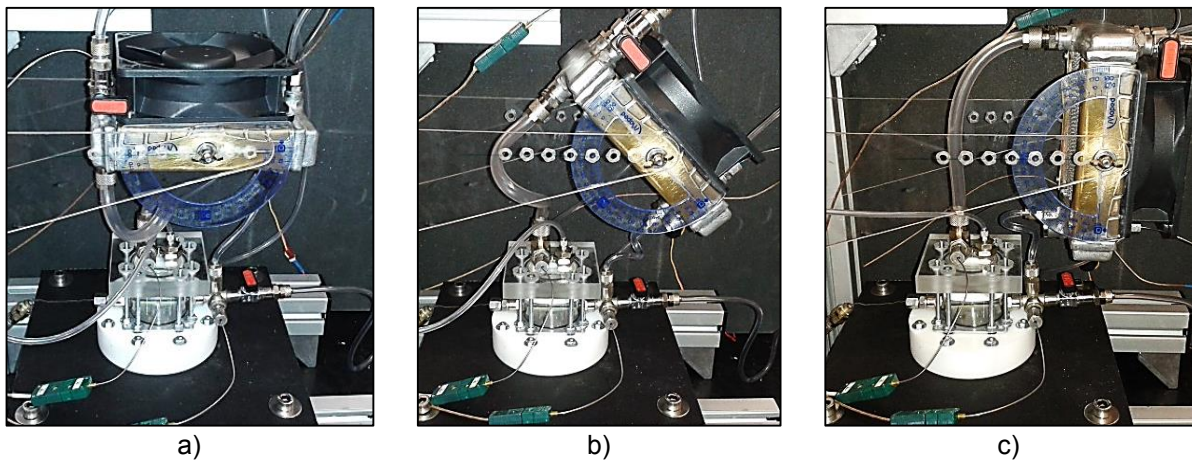


Figure 6.17 – Study on the effect of tilt angle. a) 0°; b) 45°; c) 90°

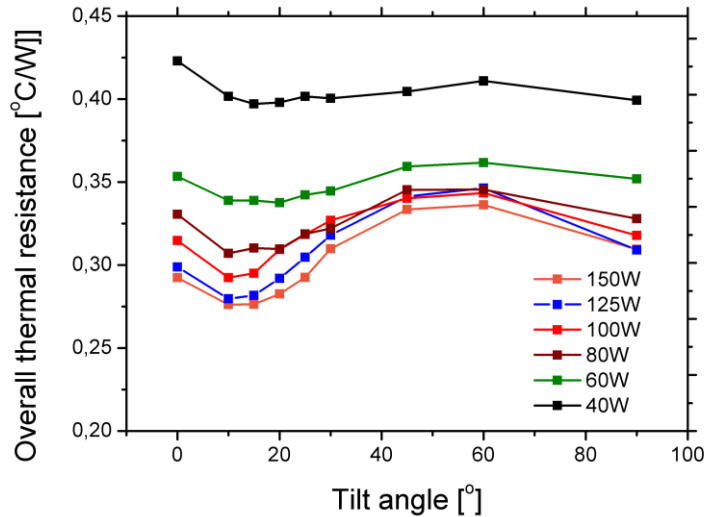


Figure 6.18 – Overall thermal resistance as function of tilt angle and heat load.

The results clearly show the existence of an optimum angle, which is particularly evident with increasing heat loads. Performing a polynomial fit to the experimental data, one can roughly estimate the optimum angle, as function of the dissipated power. In the design process of a thermosyphon for CPU cooling, the optimum tilt angle could be chosen according to the abovementioned results. Particularly, considering an Intel i7 with TDP=95W it is recommended to use a tilt angle between 9° and 13° degrees facing downward. Fortunately, the resulting optimum angle also benefits the implementation inside the highly restricted space available inside a modern desktop.

6.3.2. Reflux condenser

Reflux condensers have been increasingly applied to compact heat exchangers which are controlled by gravity [83], such as in the case of the present work. For this kind of system, vapour enters the inclined or vertical condenser and flows upwards driven by buoyancy forces, while the condensate flows downwards counter-current, under the influence of gravity. Several benefits are expected when using this configuration. First of all, in the context of the present case application, this configuration would result in a more compact geometry, because the liquid line could be suppressed. Also, even with stratified regime inside the condenser, the turbulent shear stress caused by the counter-flow could enhance heat transfer. Liquid residence time is also expected to decrease, as the first droplets of condensed liquid could leave the condenser in a shorter period of time and with less sub-cooling. Although larger sub-cooling is not considered an adverse effect, it should be avoided, since the sensitive heat transfer term is much lower, when compared to the vaporization heat transfer. In this context, the system devised in the present work, accounted for the possibility of using a reflux condenser configuration.

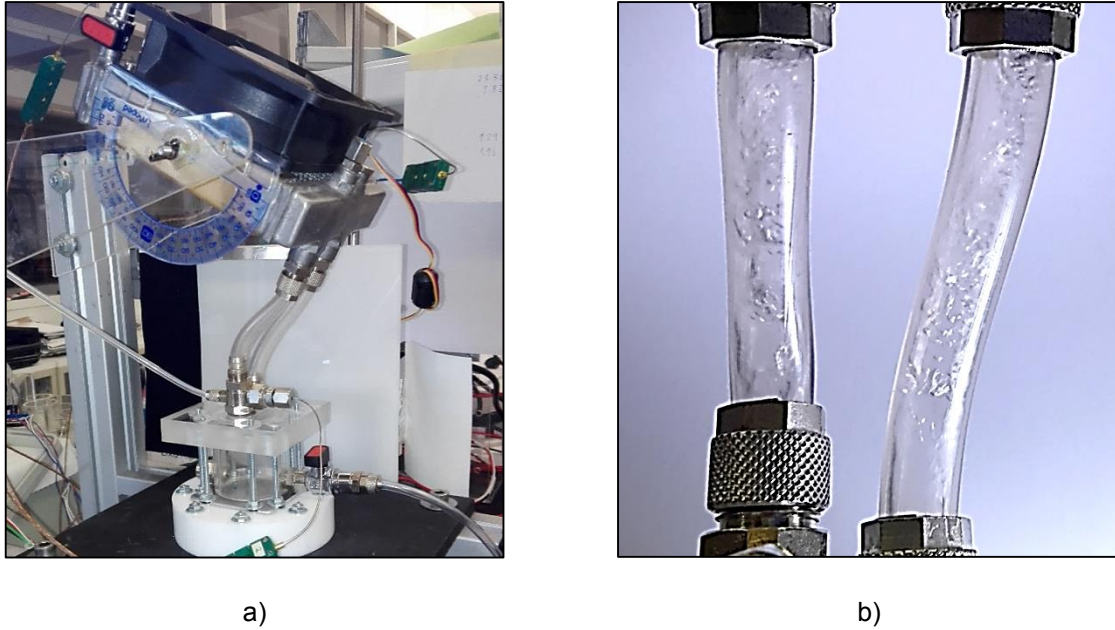


Figure 6.19 – Reflux condenser. a) Experimental test section overview; b) Counter-flow pattern in the connecting lines.

Figure 6.19 shows an overview of the experimental test section comprising the condenser in reflux configuration, as well as the counter-flow pattern in the connecting lines, which for this application were doubled, foreseeing flow interactions. Reflux condensers are usually applied in compact thermosyphons when the geometry is similar to a heat-pipe like configuration without capillary wick. With this configuration, several studies stress out the operating limit of the device controlled by the onset of temperature fluctuations [105, 106, 107, 108]. Operating limit of the thermosyphon is dictated by the onset of temperature fluctuation at a heat flux at which unstable vapour-liquid counter current flow is generated in the connecting pipe. Fukano *et al.* [108] visually observed the vapour-liquid flow in the adiabatic section of a pipe and clarified the relation between the flow pattern and the operating limit in a closed two-phase thermosyphon with a uniform heated pipe. Based on this visualization, the authors explain that the operating limit appears due to a constrain of falling liquid to the evaporating section, by the upward flow of vapour. They conclude that a vapour plug holds up the liquid slug intermittently and brings about a periodic liquid circulation in the adiabatic section. In the present work, such temperature fluctuations were observed at values as low as 100 *W* of heat load, being magnified at higher heat fluxes. This behaviour can be indeed attributed to the phenomena reported by Fukano *et al.* [108]. Steady-state junction temperature was acquired within the usual heat load range, considered through this work. Figure 6.20a depicts these measurements as function of heat load for both condenser configurations. At higher dissipated power the devised system comprising the reflux condenser shows surprisingly high temperatures. However, standard deviation of three minutes of continuous acquisition is also depicted in every data point, as exemplified in Figure 6.20b, highlights the magnitude of fluctuation of these measures, which can explain the high temperatures obtained with the reflux condenser configuration. These fluctuations are caused by partial dry-out of the aluminium bottom surface.

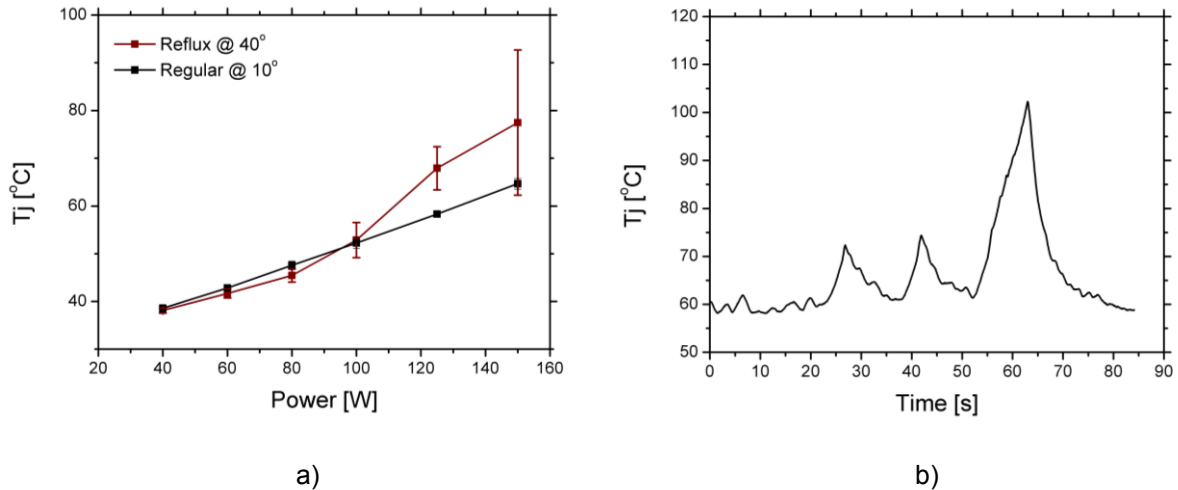


Figure 6.20 – a) Steady-state junction temperature measurements for both condenser arrangements; b) Temperature fluctuations due to partial dry-out with the reflux condenser at 150W.

A careful analysis of Figure 6.20a, namely focusing on the slope of the first three data points with the reflux condenser, suggests an improvement in the performance of the system with the reflux condenser. However, this analysis is rather speculative and, despite of all the efforts conducted to inhibit flow interactions in the connecting line, no satisfactory solution was found at higher heat loads. Inoue & Monde [105] conducted an experimental study on the effect of the connecting line diameter in the operating limit heat flux. They showed that increasing the pipe diameter from 2 mm to 6 mm increased the operating limit heat flux in 700%. Using water as working fluid, with a 6 mm diameter pipe the onset of temperature fluctuation increased to a heat flux of $19.9 W/cm^2$. The hydraulic diameter of the combined two connecting pipes used in the present work is 12.72 mm with an operating limit of $7.22 W/cm^2$. This discrepancy in absolute values is not comparable having in mind the different working fluid used, and the flow enhancement created by the above mentioned author with a bell mouth at either the top and bottom of the connecting pipe, which results in different flow patterns. However, during the experiments, a considerably high amount of foam like balance between liquid and vapour above the liquid free surface in the evaporator was noticed. Due to the close proximity to the inlet of the connecting line, this could cause an additional restriction to the liquid flowing down to the evaporator section. Decreasing the initial amount of liquid in the evaporator could reduce this interaction, but a good balance between this reduction and the earlier beginning of surface dry-out due to insufficient liquid in contact with the surface was not successfully accomplished.

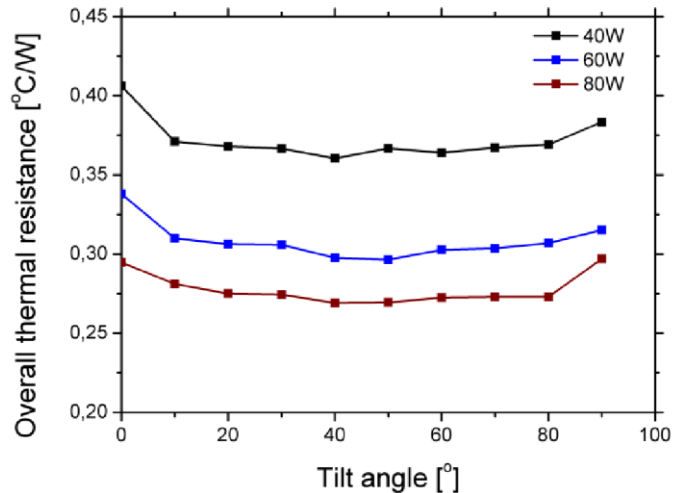


Figure 6.21 – Thermal resistance as function of reflux condenser tilt angle.

A final attempt was considered to study the inclination angle effect on the reflux condenser configuration. Figure 6.21 shows the resulting equivalent thermal resistance of the cooling system, as function of the tilt angle in the reflux condenser. Fielder and Auracher [83], using R134a as working fluid, concluded that the highest heat transfer coefficient during reflux condensation occurs between the upward facing angle of 40° and 60°. Recalling the similar study conducted in this present work in Section 6.3.1, the influence of tilt angle was only notorious at high heat loads. Unfortunately, due to the unstable condition occurring at higher heat fluxes, those results are not suitable to be compared here. Hence, only heat loads below the operating limit were considered, and although with little difference, results suggest that in fact, a tilt angle between 40 and 60 degrees in agreement with Fielder and Auracher [83] could maximize heat transfer performance, although without any significant effect on the aforementioned operating limit.

6.4. Evaporator Optimization

In the design process of a thermosyphon it is a common practice to optimize the amount of liquid used [37, 38, 109]. However, most of the studies reported in the literature, addressing liquid fill charge optimization in thermosyphons, consider much simpler geometries such as a single pipe in a two-phase closed loop where flow boiling occurs, or a reflux like configuration similar to a heat-pipe, but without a capillary wick structure, where boiling occurs usually in the vertical side wall of the evaporator section into which the liquid film condensed falls. In these configurations the effect of the ratio between liquid phase volume and total available volume is much more important than in the present case, where the evaporator and the condenser are two separate elements. Nevertheless, it is worth performing a brief experiment to explore the effect of working fluid fill charge ratio in the overall performance of the system devised in the present work. In fact, this is relevant given the already mentioned negative impact of high levels of liquid concerning friction losses and condenser flooding. On the other hand, an insufficient amount of liquid can result in surface dry-out. Finally, the optimization of the amount of liquid used can be important, given the decrease in the liquid level ratio, with increasing heat load, discussed in Section 6.1.

Resulting steady-state overall thermal resistance of the devised cooling system, as function of initial working fluid fill charge is depicted in Figure 6.22.

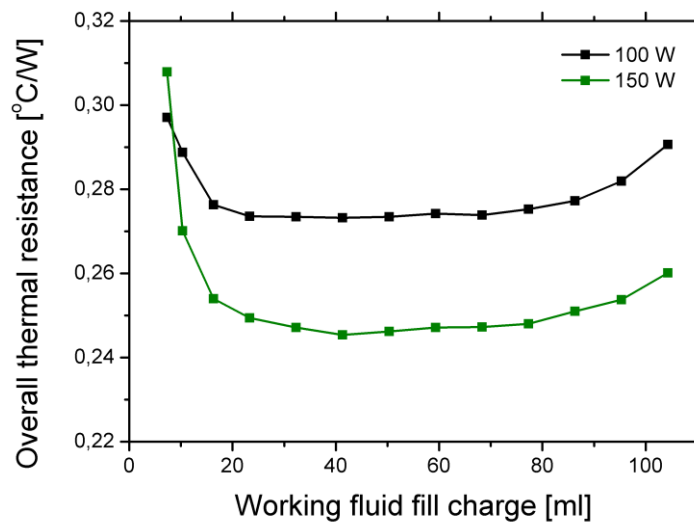


Figure 6.22 – Overall thermal resistance as function as initial working fluid fill charge

The results clearly show that for a fill charge lower than a critical value ($< 20\text{ ml}$) the thermal resistance rises. This trend is observed to be due to partially dry-out, being, naturally more evident at higher heat loads. On the other hand, with increasing fill charge the amount of liquid inside the liquid line increases, leading to higher friction losses and, consequently, higher equilibrium pressure. At even higher fill charges ($> 80\text{ ml}$) the condenser bottom starts to flood, which also deteriorates the overall performance. It may be worth mentioning that according to Nishikawa *et al.* [110], the wall superheat decreases due to the enhancement of evaporation for low liquid levels below 5 mm and a heat flux $\leq 6.5\text{ W/cm}^2$ for water. The exact values depend on the properties of the working fluid, but a similar reasoning can be applied in the present study. In this context, it was expected that before the onset of temperature fluctuations, due to partially surface dry-out, an optimum point could be identified, to optimize the fill charge. However, such point could not be identified. Additionally, for fill charge values between 32 ml and 77 ml , the influence of this parameter on the simulated die junction temperature was lower than 1°C , which is of the same magnitude as the combined uncertainty for temperature difference measurements used to calculate thermal resistance. The optimum fill charge for this configuration is thus considered to be within 32 ml and 77 ml .

6.4.1. Orientation effects

With a fixed minimum liquid fill charge one could reduce the overall size of the evaporator, decreasing the void volume and, consequently, minimizing the friction losses and cycle response time. Although this was of vital importance having in mind the application of the devised system to desktop CPU cooling, at this stage is considered a priority to address the thermal performance under vertical orientation. In fact, in most of the PC desktops the CPU is mounted vertically. However, nucleate

boiling heat transfer from a vertically oriented surface could deteriorate the performance of the cooling system, as discussed in Chapter 3.

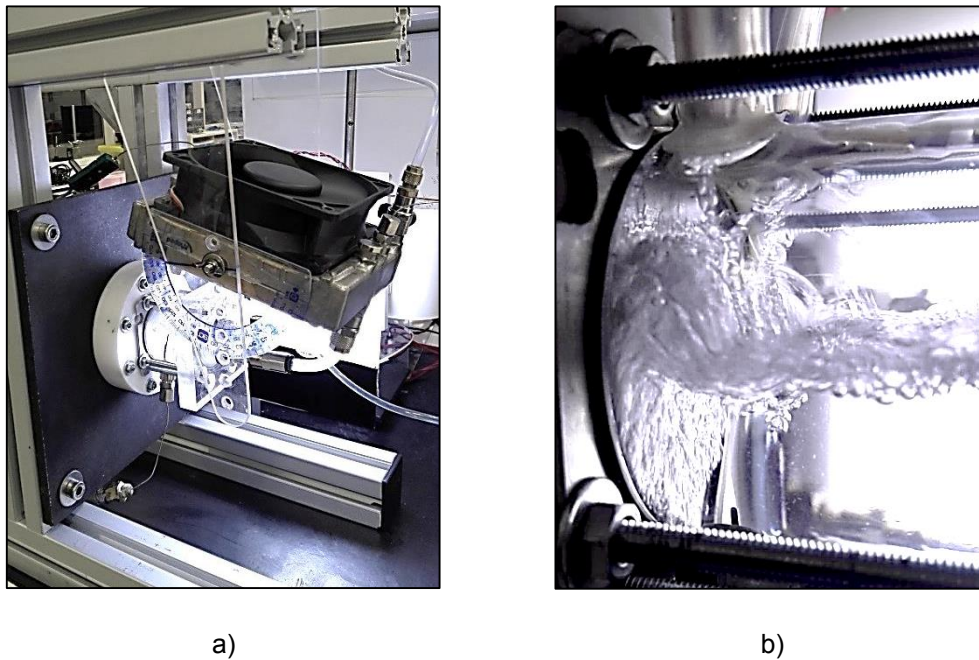


Figure 6.23 – a) Overview of the experimental facility comprising a vertically oriented evaporator; b) Detail of the boiling phenomena occurring inside the evaporator at $Q=150W$.

The decrease in CHF with increasing tilt angle is well reported in the literature, as revised in Section 3.3. To fully understand this effect in the present study, boiling curves under real working conditions and also under controlled environment were performed, using the same fill charge of working fluid. Results are presented in Figure 6.24.

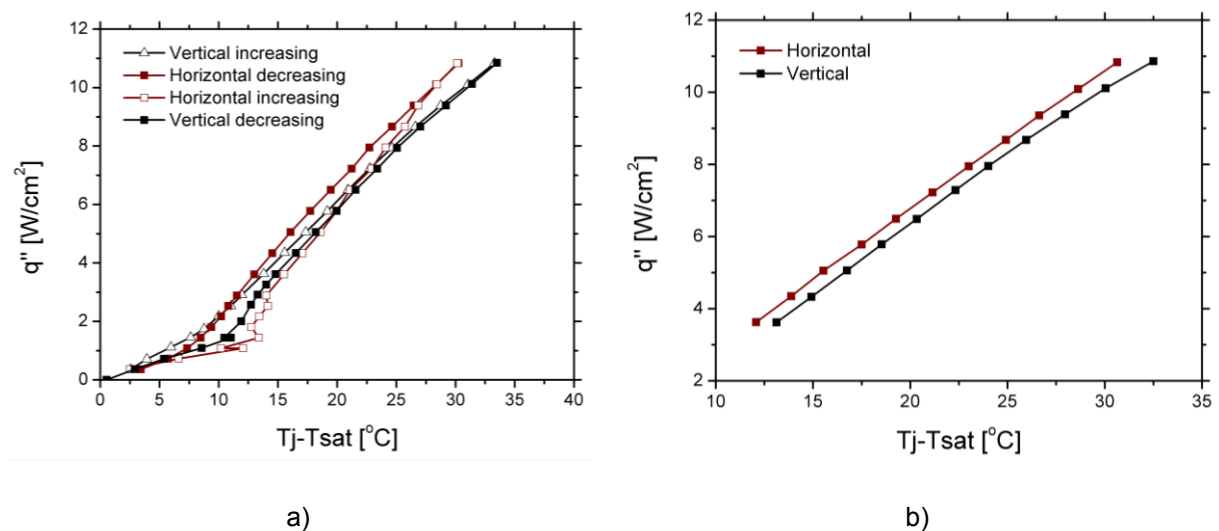


Figure 6.24 – a) Boiling curves under real working conditions for vertical and horizontal orientation. Increasing and decreasing heat flux; b) PID controlled environment comparison between horizontal and vertical orientation

Concerning the real working conditions curve, is evident that the natural convection regime benefits from the change in orientation. Also, even if the incipient boiling occurs at higher imposed heat flux, a

smaller wall superheat seems to be evident. However, due to small significance of the collected data one should not emphasize this conclusion. Concerning the high heat flux region, a similar behaviour is observed, for both real and controlled experimental conditions: a small increase in the wall superheat is notorious, increasing when the maximum heat load applied is approached. This may be so, since it is known that the CHF decreases with inclination angle (e.g. Mohamad & Bostanci [65]). So, although the CHF was never reached when the evaporator was placed in the horizontal position, it may occur at a lower heat flux in the vertical position. In fact due to the absence of buoyancy forces moving the bubbles away from the surface, lateral coalescence is promoted. However, at small heat fluxes, heat transfer may be enhanced owing to sensible heat transport by compulsory removal of the thermal layer by the raising bubble close to the surface and the latent heat transport by evaporation from thin liquid film underneath the rising bubble.

To conclude, in terms of overall thermal resistance, an increase of 5% is acknowledged, with a practical implication to the CPU junction temperature of an increase of 2.1°C in average, at 150 W of heat load. 150 W is still the heat load that maximizes the loop performance. Looking towards the development of a CPU cooling system, this small decrease in performance is clearly outweighed by the benefit of implementing the devised system in a vertically oriented CPU, which is the most usual configuration.

Furthermore, it is relevant to explain that the above experiments were performed with the optimum amount of liquid fill charge, similarly to the procedure followed when the evaporator was placed in the horizontal position. However, due to the fact that the liquid free line is now perpendicular to the surface, results are considerably different, as depicted in Figure 6.25.

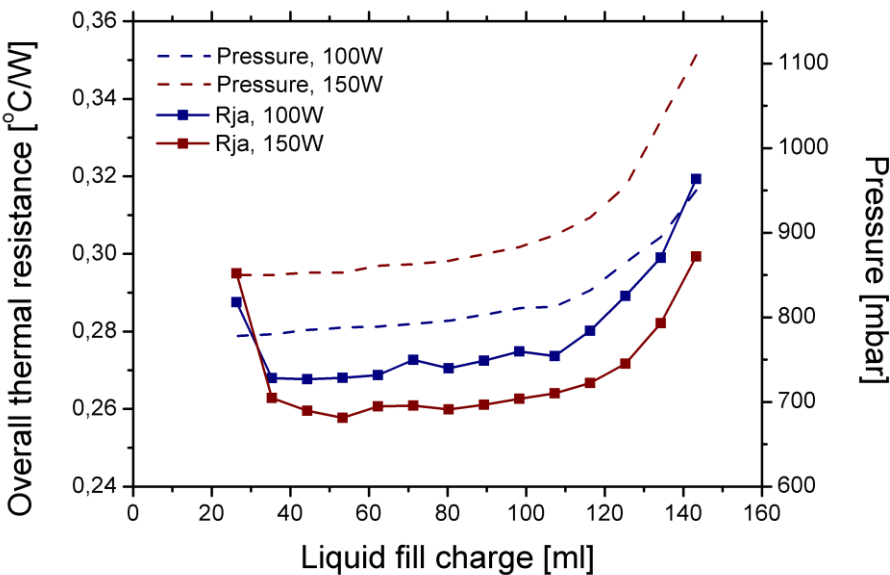


Figure 6.25 – Overall thermal resistance and equilibrium pressure as function of initial working fluid fill charge with vertical orientation

Contrarily to the observations reported when the evaporator was placed in the horizontal position, the existence of an optimum point is now more evident. Figure 6.25 depicts the overall thermal resistance and equilibrium pressure in the same plot, thus one can infer the influence of equilibrium pressure in the overall thermal resistance. With high levels of working fluid ($> 110 \text{ ml}$), the equilibrium pressure is extremely high due to flooding of the condenser. With working fluid charges below $100\text{--}120 \text{ ml}$, the condenser is no longer flooded and the decrease in fluid charge contributes to reduce the friction losses in the liquid return line. The continuous overall performance increase with decreasing fluid charge is now evident. Nevertheless, a critical minimum is attained when surface dry-out occurs. Recalling Figure 6.23b, one can conclude that the optimum fill charge ratio produces a liquid free surface line that does not cover the entire surface. However, due to buoyancy forces, the liquid is impelled and covers most of the surface. In principle, the impelled fluid-vapour mixture is not as effective as pool boiling direct contact, but the results depicted here, clearly show that the attained decrease in pressure with consequent decrease in saturation temperature benefits heat transfer.

6.4.2. Effect of evaporator's dimension in vertical orientation

Following the development of the system towards the development of a CPU cooling system, in a vertically oriented CPU mount, one should further infer on the effect of the size of the evaporator for this new orientation.

Due to feasibility constraints related to the space that is available in the desktop for the assembly of the system for the vertical orientation, the evaporator could not be further increased. Hence, the contact area between the evaporator and the aluminium interface surface was reduced. The diameter of the evaporator was consequently reduced from 42 mm (as used in all the previous experiments) to 32 mm . Also, the height of the evaporator was decreased, from 40 mm (as used in the previous experiments), to 18 mm , which is the minimum feasible height to implement with the devised test section. Both configurations were firstly subjected to a liquid fill charge optimization in order to allow a fair comparison. For the evaporator with 32 mm diameter and 40 mm height, the results are presented in Figure 6.26.

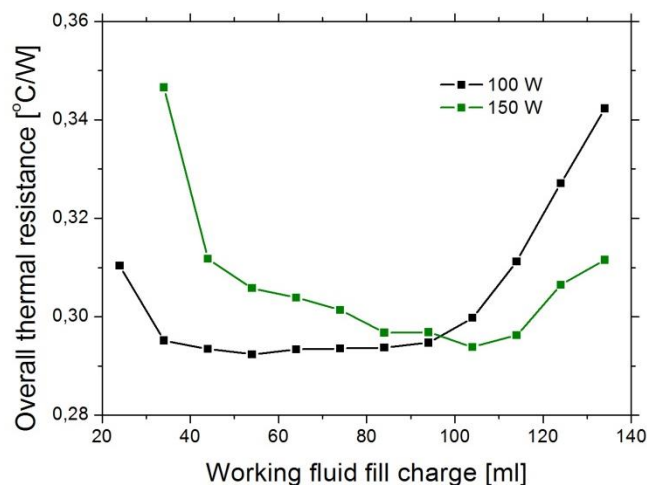


Figure 6.26 – Overall thermal resistance as function of initial fill charge ratio.

With $Q = 100\text{ W}$ the overall thermal resistance versus working fluid fill charge follows the same behaviour as Figure 6.25 with the evaporator with $D = 42\text{ mm}$. However, the results are quite different for the highest heat load of 150 W . In fact, due to the reduction in area for the same dissipated power, the heat flux is now closer to the critical value. With this heat flux, and as consequence of the vertical orientation, heat transfer coefficient starts to decrease, which in turn increases the overall thermal resistance. With a lower amount of fluid, the working pressure and saturation temperature also decrease, which should contribute to enhance heat transfer. However, since the critical heat flux also decreases, the heat transfer coefficient will be lower due to the boiling regime that occurs near this critical heat flux. This means that for this configuration, the amount of liquid is dependent on the target TPD. For reference and based on the results depicted in Figure 6.26, the initial fill charge was chosen to be 80 ml , as it establishes a good compromise between avoiding proximity to the high pressure region, where flooding of condenser occurs, and the low pressure region where close proximity to critical heat flux may endanger the integrity of the CPU.

Following the same reasoning, for the evaporator with smallest height, the fill charge was chosen to be 60 ml .

Due to the fact that for the smaller evaporator, the contact area between liquid and the interface is reduced in 45%, the boiling curves are not comparable to those discussed in the previous sections. Hence, Figure 6.27 depicts the global thermal resistance, as a function of the heat load for all the vertical configurations tested.

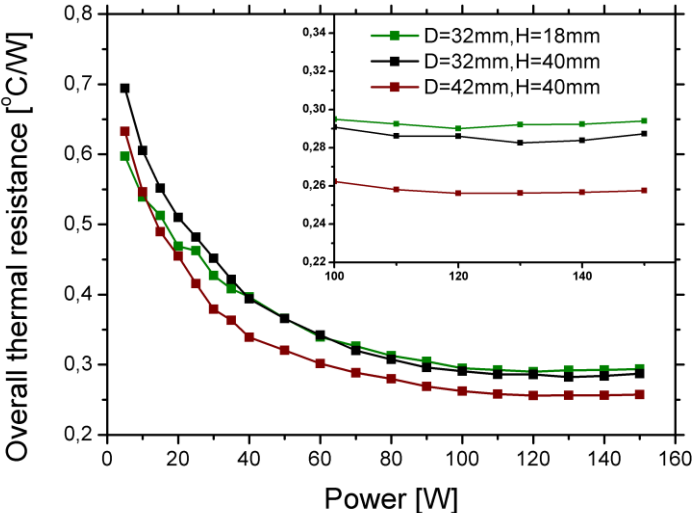


Figure 6.27 – Overall thermal resistance as function of heat load for the three vertical configurations tested.

One can conclude that the reduction in contact area notoriously decreases the performance of the system. Given that even for the evaporator with the smallest diameter, this dimension is larger than the length of the IHS, the higher global thermal resistance, which is associated to a lower performance of the system is attributed to the absence of heat spreading on the aluminum interface, which has now

been uncovered as beneficial. Concerning the reduction in the evaporator height, differences are within the uncertainty of measurement, so, any conclusions can be withdrawn.

The final thermosyphon geometry, that resulted from the above study, has a maximum performance at 130 W with $R_{ja} = 0.29\text{ }^\circ\text{C/W}$.

7. Conclusions and Future Work

7.1. Conclusions

In the present work the investigation, design and development of a benchmark experimental facility based on a two-phase closed loop thermosyphon was addressed. The performed study aims at demonstrating the feasibility to apply pool boiling of a dielectric fluid as a CPU cooling technique.

To assure well defined experimental conditions, an accurate and reliable simulation of a CPU thermal behavior was developed. The system consists in an electronically controlled transistor coupled to an integrated heat spreader, which is able to reproduce typical power load profiles of a micro-processor. The materials, geometry and dimensions of the simulated CPU were also accurately replicated. The thermal behavior of the simulated CPU was confirmed provide a representative reproduction of thermal behavior of the real micro-processor, both in steady-state and in transient conditions.

The devised pool boiling system is based on a thermosyphon like configuration, combining boiling and condensation in a close loop. The devised system acts as a modular benchmark facility, to allow a detailed study on the various parameters that influence its performance. The main outcomes of this study can be summarized as follows:

- Arrays of laser etched cavities characterized the surface structures used in this work. The cavities have fixed shape and dimensions, so that the sole varying parameter is the distance between cavities, S . Structuring the surface resulted in an enhancement of the cooling performance of the system. In steady-state conditions an improvement of 21% in terms of the overall thermal resistance using the surface with cavities distance of $300 \mu m$ was achieved, when compared to the performance evaluated for a smooth surface. In transient power steps, the onset of nucleate boiling was identified as the critical parameter influencing the system performance, due to the overshoot in the temperature above steady-state values. The maximum overshoot recorded across the entire power range tested, with the surfaces of $300 \mu m$ and $400 \mu m$ was lower than $4^\circ C$ and peak temperature at overshoot always lower than steady-state settled temperature.
- The inclination angle of the condenser was found to affect the overall performance of the system. An inclination angle of 10° compared to the horizontal position led to a decrease in 5% of the overall thermal resistance. A reflux configuration was also investigated, but unstable conditions dictate the operating limit heat load to $80 W$, due to a severe counter-flow contain in the connecting lines.
- The previous conclusions were inferred based on a horizontally oriented evaporator. Considering that the processors are usually assembled inside the desktop tower to work in the vertical orientation, the effect of the evaporator orientation was investigated. The tests

showed, as expected, a small decrease in the performance when comparing to the horizontal orientation. However this outcome is balanced by the benefits arising from more application oriented implementation

- In the vertically oriented position, the effect of the evaporator size was also quantified. Decreasing the diameter of the evaporator was necessary due to geometrical constraints related with the final application. The resulting reduced contact area will negatively influence the heat spreading, thus leading to a consequent increase in the thermal resistance. This trend was observed especially in proximity to the critical heat flux. Reduction of the evaporator volume with the same contact area (i.e. by reducing the height of the evaporator) has a negligible effect in the performance of the devised system. However, the range of initial optimum liquid fill charge under these conditions is narrower.

Based on this analysis, the geometry of the final system was optimized. The final thermal resistance achieved was $R_{ja} = 0.29 \text{ }^\circ\text{C}/\text{W}$ for a heat load $Q = 130 \text{ W}$.

7.2. Future work

This work, provided insightful knowledge on the practical application of a closed loop thermosyphon for CPU cooling, designed for an actual desktop PC. The next incoming step to be followed comprises the assembly of the dimensioned two-phase loop thermosyphon in a real desktop PC. This will allow a more reliable demonstration of the feasibility of such cooling system. Properly design structured surfaces were prepared for the purpose.

In this context a reflux condenser could be used in order to obtain a more compact design. To tackle the various problems that were found when testing this configuration in the present work, a more detailed study of this configuration must be performed.

Removing the interface surface placed between the liquid and the heat spreader (IHS) will further reduce the thermal resistance. Structured heat spreaders were already prepared and are ready to be tested in order to evaluate the effectiveness of this solution.

CPU with cavities laser etched directly in the micro-processor were also prepared. Testing the so structured components in direct immersion in a boiling dielectric fluid is of extreme interest for a more extreme cooling solution.

References

- [1] G. E. Moore, "Cramming more components onto integrated circuits," *Electronics*, vol. 38, no. 8, pp. 114-117, 1965.
- [2] J. Hennesy and D. A. Patterson, *Computer Architecture: A Quantitative Approach*, Morgan Kaufmann, 2003.
- [3] A. Kumar, L. Shang, L.-S. Peh and N. K. Jha, "A coordinated hardware-software approach for dynamic thermal management," in *43rd Design Automation Conference ACM/IEEE*, San Francisco, CA, 2006.
- [4] D. Brooks and M. Martonosi, "Dynamic thermal management for high-performance microprocessors," in *Seventh International Symposium on High-Performance Computer Architecture*, Washington, DC, 2001.
- [5] A. Bar-Cohen, "State-of-the-art and trends in the thermal packaging of electronic equipment," *ASME J. Electron*, vol. 114, pp. 254-270, 1992.
- [6] S. S. Tonapsi, R. A. Fillion, F. J. Schattenmann, H. S. Cole, J. D. Evans and B. G. Sammakia, "An Overview of Thermal Management for Next Generation Microelectronic Devices," in *IEEE/SEMI Advanced Manufacturing Conference*, 2003.
- [7] P. Y. Paik, K. Chakrabarty and V. K. Pamula, "Adaptive Cooling of Integrated Circuits using Digital Microfluidics," Artech House, 2007.
- [8] T. Cader, L. J. Westra and R. C. Eden, "Spray Cooling Thermal Management for increased Device Reliability," *IEEE Transactions on Device and Materials Reliability*, 2004.
- [9] I. Mudawar, "Assessment of High-Heat-Flux Management Schemes," *IEEE Transactions on Component And Packaging Technologies*, vol. 24, pp. 122-141, 2001.
- [10] C. Lasance and R. Simons, "Advances in High Performance Cooling for Electronics," *Electronics Cooling*, 2005.
- [11] S. Naphon and S. Wiriyasart, "Liquid cooling in the mini-rectangular fin heat sink with and without thermoelectric for CPU," *International Communications in Heat and Mass Transfer*, vol. 36, pp. 166-171, 2009.

- [12] S. Kang, D. Miller and J. Cennamo, "Sukhvinder Kang, David Miller, John Cennamo "Closed loop liquid cooling for high performance computer systems" Proceedings of IPACK2007 ASME InterPACK '07" Vancouver, 2007.
- [13] M. Nazari, M. Karami and M. Ashouri, "Comparing the thermal performance of water, Ethylene Glycol, Alumina and CNT nanofluids in CPU cooling: Experimental study," *Experimental Thermal and Fluid Science*, vol. 57, pp. 371-377, 2014.
- [14] R. Mohammed, Y. Xia, R. Sahan and Y. Pang, "Performance improvements of air-cooled thermal tool with advanced technologies," in *Semiconductor Thermal Measurement and Management Symposium (SEMI-THERM)* , 2012.
- [15] H. G. Yun, G. Hwang and T. G. Choy, "Experimental Study on the Performance of miniature heat pipes with woven-wire wick," *IEEE Transactions on components and packaging technologies*, vol. 24, pp. 591-595, 2001.
- [16] K. S. Kim and B. Back, "Heat pipe cooling technology for desktop PC CPU," *Applied Thermal Engineering*, vol. 23, pp. 1137-1144, 2003.
- [17] Y. Koito, Y. Imura, M., Y. Mochizuki and S. S. Torii., "Numerical analysis and experimental verification on thermal fluid phenomena in a vapor chamber," *Applied Thermal Engineering*, vol. 26, pp. 1669-1676, 2006.
- [18] M. Lu, L. Mok and R. J. Bezama., "A Graphite Foams Based Vapor Chamber for Chip Heat Spreading," *ASME Journal of Electronic Packaging*, vol. 128, pp. 427-431, 2006.
- [19] R. Rulliere, F. Lefevre and M. Lallemand., "Prediction of the maximum heat transfer capability of two-phase heat spreaders- Experimental validation," *International Journal of Heat and Mass transfer*, vol. 50, pp. 1255-1262, 2007.
- [20] V. G. Pastukov, Y. F. Maidanik, C. V. Vershinin and M. A. Korukov, "Miniature loop heat pipes for electronics cooling," *Applied Thermal Engineering*, vol. 23, pp. 1125-1135, 2003.
- [21] R. A. Singh, C. Akbarzadeh, M. Dixon, Mochizuki and R. Riehl., "Miniature Loop Heat Pipe With Flat Evaporator for Cooling Computer CPU," *IEEE Transactions on Components and Packaging Technologies*, vol. 30, pp. 42-49, 2007.
- [22] A. Faghri, "Review and Advances in Heat Pipe Science and Technology," *Journal of Heat Transfer*, vol. 132, no. 12, 2012.

- [23] J. Y. Chang, H. S. Park and S. Julia., "A System Design of Liquid Cooling Computer Based on the Micro Cooling Technology", Tenth Intersociety Conference on Thermal and Thermomechanical Phenomena and Emerging Technologies in Electronic Systems," *iTHERM 2006*, pp. 157-160, 2006.
- [24] V. Silverio, "Methanol and etanol evaporating flow mechanisms in square and circular microchannels," *Proceedings of 8th World conference on experimental Heat Transfer, Fluid Mechanics and Thermodynamics*, 2003.
- [25] C. Perret, J. Boussey, M. Schaeffer and Coyauld, "Analytic Modeling Optimization, and Realization of Cooling Devices in Silicon Technology," *IEEE Transactions on Components and Packaging Technologies*, vol. 23, pp. 665-672, 2000.
- [26] A. Bar-Cohan, M. Arik and M. Ohadi, "Direct Liquid cooling of high flux micro and nano electronic components," *Proceedings of the IEEE*, vol. 94, pp. 1549-1570, 2006.
- [27] C. V. and F. F. Chiriac, "The Optimization of a Refrigeration Vapor Compression System for Power Microelectronics," *10th IEEE intersociety conference on Thermal and Thermomechanical Phenomena in Electronic Systems*, pp. 764-770, 2006.
- [28] S. Trutassanawin, E. Groll, V. Garimella and L. Cremaschi, "Experimental Investigation of a Miniature-Scale Refrigeration System for Electronic Cooling," *IEEE Transactions on Components and Packaging Technology*, vol. 29, pp. 678-687, 2006.
- [29] H. Bostanci, R. Daniel, K. John and C. Louis, "Spray Cooling with Ammonia on microstructured Surfaces: Performance Enhancement and Hysteresis Effect," *Journal of Heat Transfer*, vol. 131, 2009.
- [30] J. Guerreiro, "Desenvolvimento de um sistema avançado para o arrefecimento de processadores," Master thesis - Instituto Superior Técnico, Universidade de Lisboa, 2011.
- [31] W. T. Kim, K. S. Song and Y. Lee, "Design of a Two-Phase Loop Thermosyphon for Telecommunications System - Experiments and Visualization," *KSME International Journal*, vol. 12, no. 5, pp. 926-941, 1998.
- [32] H. Toyoda and Y. Kondo, "Effect of Non-Condensable Gas Leakage on Long Term Cooling Performance of Loop Thermosyphon," *Journal of Electronics Cooling and Thermal Control*, vol. 3, pp. 131-135, 2013.

- [33] R. Khodabandeh and B. Palm, "Influence of system pressure on the boiling heat transfer coefficient in a closed two-phase thermosyphon loop," *International Journal of Thermal Science*, vol. 41, pp. 619-624, 2002.
- [34] E. Teodori, A. S. Moita and A. L. N. Moreira, "Empirical and Modeling-based correlations for pool boiling on microstructured surfaces," *Interfacial Phenomena and Heat Transfer*, vol. 2, no. 3, pp. 273-292, 2014.
- [35] C. Ramaswamy, Y. Joshi, W. Nakayama and W. Johnson "Performance of a compact two-phase thermosyphon: Effect of evaporator inclination, liquid fill volume and contact resistance," *Proceedings of the 11th International Heat Transfer Conference*, vol. 2, pp. 127-132, 1998.
- [36] C.-C. Chang, "Two-phase closed-loop thermosyphon for electronic cooling" *Experimental Heat Transfer*, vol. 156, no. 23, p. 144, 2010.
- [37] A. Samba, H. Louahlia-Gualous, S. Le Masson and D. Nörterhäuser, "Two-phase thermosyphon loop for cooling outdoor telecommunications equipments," *Applied Thermal Engineering*, vol. 50, pp. 1351-1360, 2013.
- [38] A. Chehade, H. Louahlia-Gualous, S. Le Masson, V. I. and N. Abouzahab-Damaj, "Experimental investigation of thermosyphon loop thermal performance," *Energy Conversion and Management*, vol. 84, pp. 671-680, 2014.
- [39] R. L. Webb, S. Yamauchi, S. Denko and K. Tochigi "Remote Heat Sink Concept for High Power Heat Rejection," *IEEE Transactions on Components and Packaging Technologies*, vol. 25, pp. 608-614, 2002.
- [40] A. Pal, Y. Joshi, M. Beitelmal and : Patel "Design and performance evaluation of a compact thermosyphon," *IEEE Transactions on Components and Packaging Technologies*, vol. 24, no. 5, pp. 601-607, 2002.
- [41] S. Gima, T. Nagata, X. Zhang and M. Fujii " Experimental Study on CPU Cooling System of Closed-Loop Two-Phase Thermosyphon," *Heat Transfer - Asian Research*, vol. 34, pp. 147-159, 2005.
- [42] P. E. Tuma, "Evaporator/Boiler Design for Thermosyphons Utilizing Segregated Hydrofluoroether Working Fluids," *Proceedings 22nd IEEE SEMI-THERM Symposium* , 2006.

- [43] S. Nukiyama, "The maximum and minimum values of the heat Q transmited from metal to boiling water under atmospheric pressure," *Journal of the Japan Society of Mechanical Engineers*, vol. 37, pp. 367-374, 1934.
- [44] M. Jakob and W. Linke, "Der Wärmeüberganag beim Verdampfen von Flüssigkeiten au senkrechten und waagerechen Flächen," *Phys. Z.*, vol. 36, pp. 267-280, 1935.
- [45] T. B. Drew and C. Mueller, "Boiling," *Transactions AIChE*, vol. 33, p. 449, 1937.
- [46] A. Bar-Cohen and T. W. Simon, "Wall Superheat Excursion in The Boiling Incipience of Dielectric Fluids," *Heat Transfer in Electronic Equipment, ASME*, vol. 57, pp. 83-94, 1986.
- [47] W. M. Rohsenow and P. Griffith, "Correlation of maximum heat transfer data for boiling saturated liquids," *Chemical Engineering Progress Symposium*, vol. 52, p. 18, 1956.
- [48] H. K. Forster and N. Zuber, "Dynamics of vapor bubbles and boiling heat transfer," *American Institute of Chemical Engineers Journal*, vol. 1, p. 531, 1955.
- [49] K. Stephan and M. Abdelsalam, "Heat-transfer correlation for natural convection boiling," *International Journal of Heat and Mass Transfer*, vol. 23, pp. 73-87, 1980.
- [50] J. M. S. Jabardo, E. F. Silva and S. F. Barros, "Evaluation of the Rohsenow correlation through experimental pool boiling of halocarbon refrigerantts on cylindrical surfaces," *Journal of the Brazilian Society of Mechanical Scences and Engineering*, vol. 26, no. 2, pp. 218-230, 2004.
- [51] S. S. Kutateladze, "A hydrodynamic Theory of Changes in Boiling Process under Free Convection," *Proceedings of the Russian Academy of Sciences*, vol. 4, p. 524, 1951.
- [52] N. Zuber, M. Tribus and J. Westwater, "The Hydrodynamic Crisis in Pool Boiling of Saturated and Subcooled Liquids," in *Proceedings of 1961-62 International Heat Transfer Conference*, Boulder, CO, 1961.
- [53] J. H. Lienhard, *A Heat Transfer Textbook*, Englewood Cliffs, NJ: Prentice-Hall, 1987.
- [54] S. L. Kim, I. C. Bang, J. Buogiorno and L. W. Hu, "Surface wettability change during pool boiling of nanofluid and its effect on critical heat flux," *International Journal of Heat and Mass Transfer*, vol. 50, pp. 4105-4116, 2007.

- [55] S. G. Kandlikar, "A theoretical model to predict pool boiling FC incorporating effects of contact angle and orientation," *Journal of Heat Transfer*, vol. 123, pp. 1071-1079, 2001.
- [56] C. Gerardi, J. Buongiorno and L. W. Hu, "Study of bubble growth in water pool boiling through synchronized, infrared, thermometry and high-speed video," *International Journal of Heat and Mass Transfer*, vol. 53, pp. 4185-4192, 2010.
- [57] Y. Y. Hsu and R. W. Graham, *Transport processes in boiling and two-phase systems, including near-critical fluids*, Washington, D.C., Hemisphere, 1976.
- [58] N. Kurul and M. Podowski, "Multidimensional effects in forced convection subcooled boiling," *Proceedings of the 9th International Heat Transfer Conference*, pp. 21-25, 1990.
- [59] C. Y. Han and P. Griffith, "The mechanism of heat transfer in nucleate boiling," *Technical Report No. 7673-19, Department of Mechanical Engineering, Massachusetts Institute of Technology*, 1962.
- [60] C. Gerardi, J. Buongiorno, L. W. Hu and T. McKrell, "Measurement of nucleation site density, bubble departure diameter and frequency in pool boiling of water using high-speed infrared and optical cameras," in *7th ECI International Conference on Boiling Heat Transfer*, Florianopolis, 2009.
- [61] D. C. Das, K. Ghosh and D. Sanyal, "A scale analysis model for film boiling heat transfer on a vertical flat plate with wide applicability," *International Journal of Heat and Mass Transfer*, vol. 90, pp. 40-48, 2015.
- [62] S. Ishigai, K. Inoue, Z. Kiwakit and T. Inai, "Boiling heat transfer from a flat surface facing downward," in *International Heat Transfer Conference*, Boulder, CO, 1961.
- [63] A. H. Howard and I. Mudawar, "Orientation effects on pool boiling critical heat flux (CHF) and modeling for near-vertical surfaces," *International Journal of Heat and Mass Transfer*, vol. 42, pp. 1665-1688, 1999.
- [64] K. Nishikawa, Y. Fujita, S. Uchida and H. Ohta, "Effect of surface configuration on nucleate boiling heat transfer," *International Journal of Heat and Mass Transfer*, vol. 27, no. 9, pp. 1559-1571, 1983.

- [65] M. S. Genk and H. Bostanci, "Satuaration boiling of HFE-7100 from a copper surface, simulating a microelectronic chip," *International Journal of Heat and Mass Transfer*, vol. 46, pp. 1841-1854, 2003.
- [66] M. Jakob, "Heat Transfer in evaporation and condensation," *Journal of the American Society of Mechanical Engineers*, vol. 58, pp. 73-87, 1980.
- [67] D. Kim, D. Yu, D. Jerng, M. Kim and H. Ahn, "Review of boiling heat transfer enhancement on micro/nanostructured surfaces," *Experimental Thermal and Fluid Science*, vol. 66, pp. 173-196, 2015.
- [68] M. E. Poniewski and J. R. Thome, *Nucleate Boiling on Micro-Structured Surfaces*, Texas, USA: Heat Transfer Reserach, Inc. (HRTI), 2008.
- [69] C. K. Yu, D. C. Lu and C. C. Tsung, "Pool boiling heat transfer on arteficial micro-cavity surfaces in dielectric fluid FC-72," *Journal of Micromechanics and Microengineering*, vol. 16, pp. 2092-2099, 2006.
- [70] D. Nitesh, S. Nimkar, H. Bhavnani and R. C. Jaeger, "Effect of nucleation site spacing on the pool boiling characteristics of a structured surface," *International Journal of Heat and Mass Transfer*, vol. 49, pp. 2829-2839, 2006.
- [71] A. S. Moita, E. Teodori and A. L. N. Moreira, "Enhancement of pool boiling heat transfer by surface micro-structuring," *Journal of Physics: Conference Series*, vol. 395, 2012.
- [72] E. Teodori, A. S. Moita and A. L. N. Moreira, "Characterization of pool boiling mechanisms over micro-patterned surfaces using PIV," *International Journal of Heat and Mass Transfer*, vol. 66, pp. 261-270, 2013.
- [73] V. V. Chekanov, "Interaction of centers in nucleate boiling," *Teplofizika Vysokikh Temperatur*, vol. 15, pp. 121-128, 1977.
- [74] K. J. Bell, J. Taborek and F. Fernoglio, "Interpretation of Horizontal Intube Condensation Heat Transfer Coirrelation with Two-Phase Flow Regime Map," *Chemical Engineering Progress Symposium Series*, vol. 66, no. 102, pp. 159-165, 1970.
- [75] D. Baker, "Simultaneous Flow of Oil and Gas," *Oil and Gas Journal*, vol. 53, pp. 183-195, 1954.

- [76] J. C. Chato, "Laminar Condensation inside horizontal tubes," Ph.D. Thesis - Massachusetts Institute of Technology, 1960.
- [77] J. G. Collier and J. T. Thome, *Convective Boiling and Condensation*, New York: Oxford University Press, 1996.
- [78] V. Carey, *Liquid-Vapor Phase-Change Phenomena*, New York: Hemisphere, 1992.
- [79] M. B. Ould Didi, N. Kattan and J. R. Thome, "Prediction of two-phase pressure gradients of refrigerants in horizontal tubes," *International Journal of Refrigeration*, vol. 25, pp. 935-947, 2002.
- [80] S. Lips and J. P. Meyer, "Condensation heat transfer in smooth inlined tubes for R134a at different saturation temperatures," *International Journal of Heat and Mass Transfer*, vol. 70, pp. 515-525, 2014.
- [81] S. Lips and J. P. Meyer, "Experimental study of convective condensation in an inlined smooth tube. Part I: Inclination effect on flow pattern and heat transfer coefficient," *International Journal of Heat and Mass Transfer*, vol. 55, pp. 395-404, 2012.
- [82] S. Lips and J. P. Meyer, "Two-phase flow in inclined tubes with specific reference to condensation: A review," *International Journal of Multiphase Flow*, vol. 37, pp. 848-859, 2011.
- [83] S. Fiedler and H. Auracher, "Experimental and theoretical investigation of reflux condensation in an inclined small diameter tube," *International Journal of Heat and Mass Transfer*, vol. 47, pp. 4031-4043, 2004.
- [84] H. T. Klahm and F. Z. Auracher, "Heat transfer during reflux condensation of an R134a/R123 mixture in vertical and inclined narrow tubular and rectangular channels," *International Journal of Refrigeration*, vol. 33, no. 7, pp. 1319-1326, 2010.
- [85] T. Moita, "Evaluation and development of advanced cooling systems," Master thesis, Instituto Superior Técnico - Universidade de Lisboa, 2008.
- [86] A. Maciel, "Development and Control of a condensating system using Peltier Cells.," Master thesis - Instituto Superior Técnico, Universidade de Lisboa, 2014.
- [87] K. Ogata, *Modern Control Engineering*, New Jersey: Pearson Education, Inc., 2010.

- [88] L. A. Oliveira and A. Lopes, *Mecânica dos Fluidos*, Lisboa: Lidel, 2010.
- [89] R. K. Shah and D. P. Sekulic, *Fundamentals of Heat Exchanger Design*, New Jersey: John Wiley & Sons, Inc., 2003.
- [90] T. E. Schmidt, "Heat Transfer Calculations for Extended Surfaces," *Refrigerating Engineering*, pp. 351-357, April 1949.
- [91] C.-C. Wang, Y.-M. Hwang and Y.-T. Lin, "Empirical correlations for heat transfer and flow friction characteristics of herringbone wavy fin-and-tube heat exchangers," *International Journal of Refrigeration*, vol. 25, pp. 673-680, 2002.
- [92] Y.-G. Park and A. M. Jacobi, "The Air-Side Thermal-Hydraulic," *Journal of Heat Transfer*, vol. 131, no. 6, pp. 061801-061801-13, 2009.
- [93] C. C. Wang, W. L. Fu and C. T. Chang, "Heat Transfer and Friction characteristics of Typical Wavy Fin-and-tube Heat Exchangers," *Experimental Thermal and Fluid Science*, vol. 14, pp. 174-186, 1997.
- [94] L. C. Yang, Y. Asako, Y. Yamaguchi and M. Faghri, "Numerical prediction of transitional characteristics of flow and heat transfer in a corrugated duct," *Journal of Heat Transfer*, vol. 119, pp. 62-69, 1997.
- [95] C. Isci and M. Martonosi, "Runtime power monitoring in high-end processors: Methodology and empirical data," *Proceedings of the 36th annual IEEE/ACM International Symposium on Microarchitecture*, pp. 93-104, 2003.
- [96] P. Zhang, B. Wang, W. Shi, L. Han and X. Li, "Simulation on energy performance of air-conditioning system assisted with thermosyphon used in telecommunication base station," in *Proceedings of 13th Conference of International Building Performance Simulation Association*, Chambéry, 2013.
- [97] S. W. Chang, K. F. Chiang and C. Y. Lin, "Loop thermosyphon electronic cooling device operated at sub-atmospheric pressure," in *Proceedings of 10th International Heat Pipe Symposium*, Taipei, 2011.
- [98] W. Qu, "Hydrodynamics of two-phase loop thermosyphon," *Frontiers in Heat Pipes*, vol. 1, pp. 104-111, 2010.

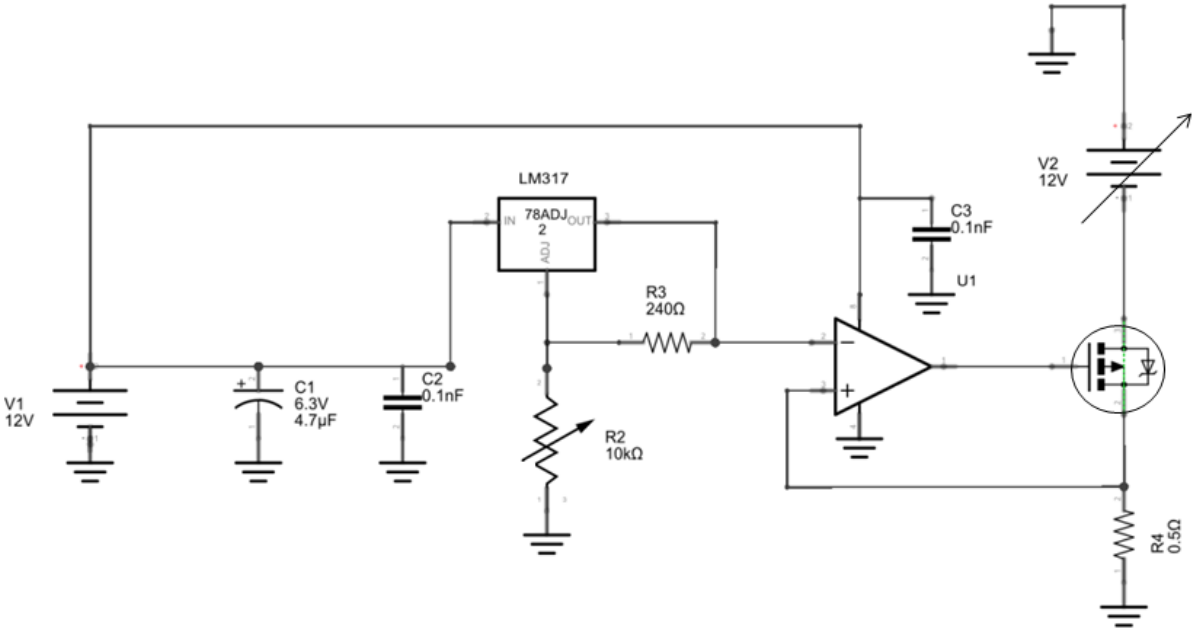
- [99] T.-E. Tsai, H.-H. Wu, C.-C. Chang and S.-L. Chen, "Two-phase closed thermosyphon vapor-chamber system for electronic cooling," *International Communications in Heat and Mass Transfer*, vol. 37, pp. 484-489, 2010.
- [100] R. I. Vachon, "Evaluation of constants for the Rohsenow pool boiling correlation," in *U.S. National Heat Transfer Conference*, Seattle, 1967.
- [101] A. S. Moita, E. Teodori and A. L. N. Moreira, "Influence of surface topography in the boiling mechanisms," *International Journal of Heat and Fluid Flow*, vol. 52, pp. 50-63, 2015.
- [102] T. Valente, E. Teodori, A. S. Moita and A. L. N. Moreira, "Effect of wettability on nucleate boiling," in *11th International Conference on Heat Transfer, Fluid Mechanics and Thermodynamics - HEFAT*, Kruger, 2015.
- [103] B. Bourdon, E. Bertrand, P. D. Marco, M. Marengo, R. Rioboo and J. De Coninck, "Wettability influence on the onset temperature of pool boiling: Experimental evidence onto ultra-smooth surfaces," *Advances in Colloid and Interface Science*, vol. 221, pp. 34-40, 2015.
- [104] B. Bourdon, R. Rioboo, M. Marengo, E. Gosselin and J. De Coninck, "Influence of the wettability on the boiling onset," *Langmuir*, vol. 28, pp. 1618-1624, 2012.
- [105] T. Inoue and M. Monde, "Operating limit of heat transport in two-phase thermosyphon with connecting pipe (heated surface temperature fluctuation and flow pattern)," *International Journal of Heat and Mass Transfer*, vol. 52, pp. 4519-4524, 2009.
- [106] M. Monde, S. Mihara and T. Inoue, "An analytical study of critical heat flux on a two-phase thermosyphon," *Transactions of the Japan Society of Mechanical Engineers*, vol. 59, no. 560, pp. 1258-1264, 1993.
- [107] M. Monde and Y. Mitsutake, "Enhancement of CHF in open thermosyphon with heated bottom chamber," *Transactions of the Japan Society of Mechanical Engineers*, vol. 39, no. 4, pp. 768-779, 1996.
- [108] T. Fukano, K. Kadoguchi and H. Imuta, "Experimental study on the heat flux at the operating limit on a closed two-phase thermosyphon," *Transactions of the Japan Society of Mechanical Engineers*, vol. 53, no. 487, pp. 1065-1071, 1987.

- [109] B. Jiao, L. Qiu, X. Zhang and Y. Zhang, "Investigation on the effect of filling ratio on the steady-state heat transfer performance of a vertical two-phase closed thermosyphon," *Applied Thermal Engineering*, vol. 28, pp. 1417-1426, 2008.
- [110] K. Nishikawa, H. Kusuda, K. Yamasaki and K. Tanaka, "Nucleate boiling at low liquid levels," *Bulletin of JSME*, vol. 10, pp. 328-338, 1967.
- [111] B. D. Marcus and D. Drpkin, "The effect of surface configuration on nucleate boiling heat transfer," *International Journal of Heat and Mass Transfer*, vol. 6, pp. 863-866, 1963.
- [112] P. Naphon and S. Wiriyaart, "Liquid cooling in the mini-rectangular fin heat sink with and without thermoelectric for CPU," *International Communications in Heat and Mass Transfer*, no. 36, p. 166-171, 2009.
- [113] S. H. Moon, H. G. Yun, G. Hwang and T. G. Choy, "Experimental Study on the Performance of miniature heat pipes with woven-wire wick," *IEEE Transactions on components and packaging technologies*, vol. 24, pp. 591-595, 2001.
- [114] L. Jiang, J. M. Koo, J. C. Zeng, L. Mikkelsen, L. Zhang and Z. Zhou, "Two-Phase Microchannel Heat Sinks for an Electrokinetic VLSI Chip Cooling System," *Proc. of the 17th IEEE SEMI-THERM Symposium*, pp. 153-157, 2001.

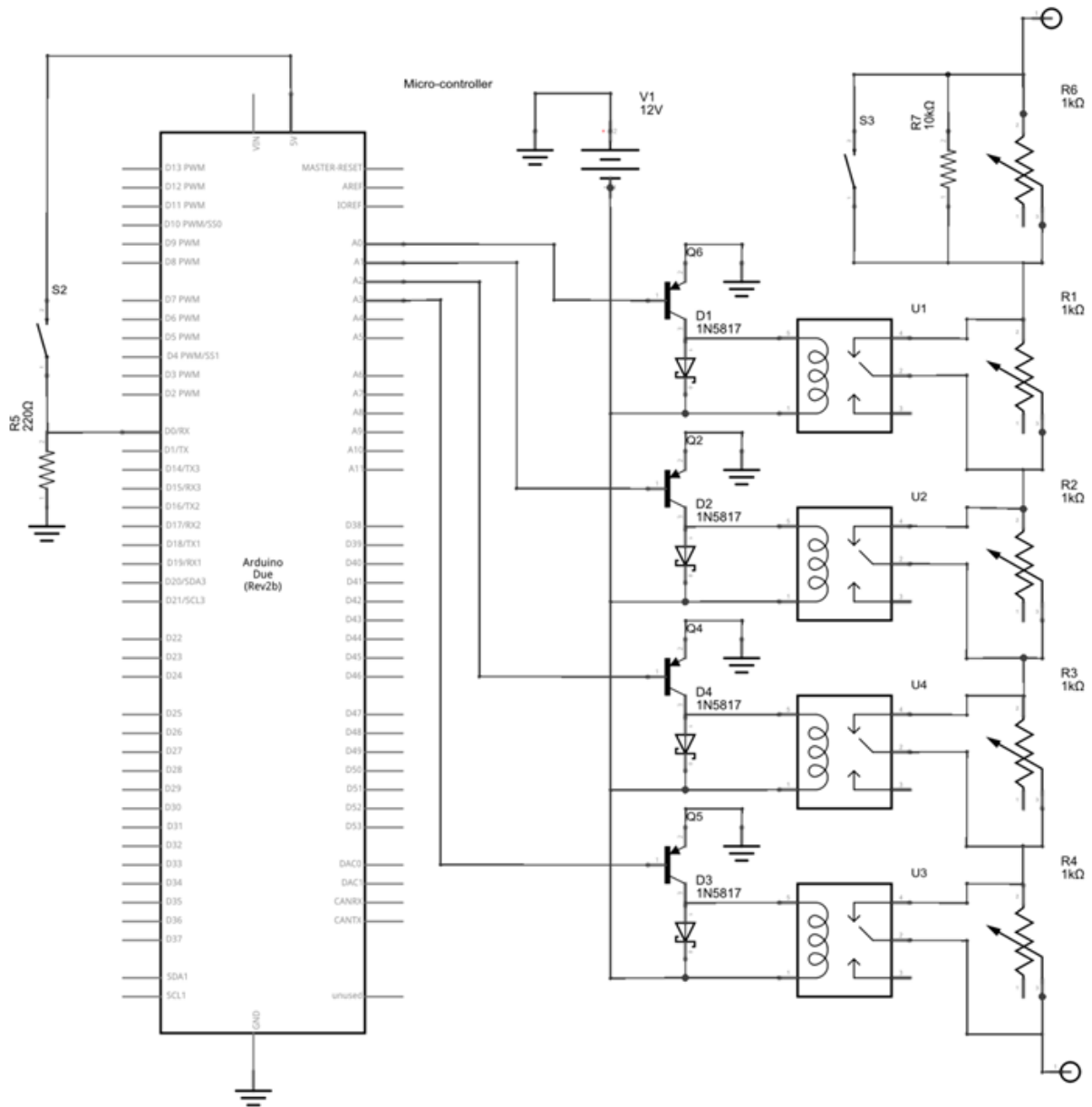
Annexes

Annex A – Electronic circuits:

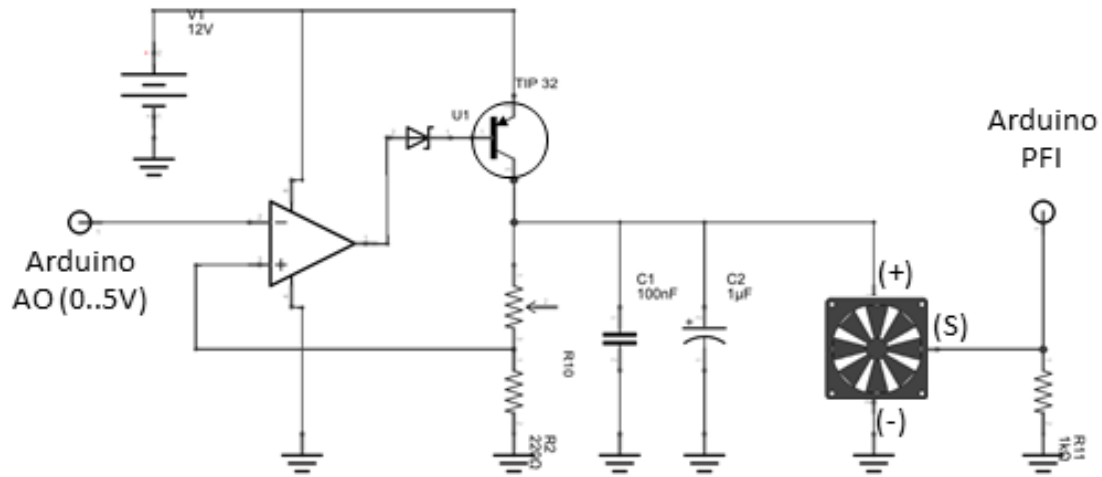
A.1. Transistor power control unit:



A.2. Power supply remote control unit:



A.3. Fan control and acquisition unit



A.4. Differential pressure transducers amplification circuit

